Pitching airfoil study and freestream effects for wind turbine applications

by

Kobra Gharali

A thesis
presented to the University of Waterloo
in fulfillment of the
thesis requirement for the degree of
Doctor of Philosophy
in
Mechanical Engineering

Waterloo, Ontario, Canada, 2013

I hereby declare that I am the sole author of this thesis. This is a true copy of the thesis, including any required final revisions, as accepted by my examiners.

I understand that my thesis may be made electronically available to the public.

Abstract

A Horizontal Axis Wind Turbine (HAWT) experiences imbalanced loads when it operates under yaw loads. For each blade element of the aerodynamically imbalanced rotor, not only is the angle of attack unsteady, but also the corresponding incident velocity, a fact usually unfairly ignored. For the unsteady angle of attack, a pitch oscillating airfoil has been studied experimentally and numerically when $3.5 \times 10^4 \leq Re \leq 10^5$. For small wind tunnel airfoils, Particle Image Velocimetry (PIV) was utilized to determine the aerodynamic loads and the pressure field where other measurement techniques are either intrusive or very challenging. For dynamic airfoils in highly separated flow fields, i.e., deep dynamic stall phenomena, loads were calculated successfully based on the control-volume approach by exploring ways to reduce the level of uncertainties in particular for drag estimation. Consecutive high resolution PIV velocity fields revealed that increasing the reduced frequency was followed by an enriched vortex growth time and phase delay as well as a reduced number of vortices during upstroke motion. Moreover, the locations of the vortices after separation were influenced by each other. Laminar separation bubble height also showed a reducing trend as the reduced frequency increased. The nature of the vortex sheet vortices before stall were explored in two Reynolds numbers, with and without laminar separation bubbles, at low angles of attack. For all cases, a vortex sheet was the result of random vortex sheding while a longer vortex sheet was more favorable for lift augmentation. A wake study and averaged drag calculation at low angles of attack were also performed with Laser Doppler Anemometry (LDA) for $Re = 10^5$. For the unsteady incident velocity, longitudinal freestream oscillations have been studied numerically, since experimental study of an unsteady freestream is challenging. In this regard, the streamwise freestream velocity and pitch angle of incidence oscillated with the same frequency in a wide range of phase differences. Changing the phase difference caused variation of the results, including significantly augmented and dramatically damped dynamic stall loads, both increasing and decreasing trends for vortex growth time during phase increase and shifted location of the maximum loads. The results showed strong dependency on the velocity and acceleration of the freestream during dynamic stall and the dynamic stall characteristics differed significantly from those of the steady freestream states. The results also demonstrated consistent trends regardless of the airfoil shape and the Reynolds number while $Re = 10^5$ and 10^6. The vortex study presented here not only provides information about the unsteady aerodynamic forces, but also knowledge regarding airfoil noise generation and distributed flow for downstream objects beyond wind turbine applications.

Acknowledgements

It is my pleasure to acknowledge some people whom I have interacted with during my PhD program. Without their help this would not have been possible.

First of all, I would like to thank my supervisor, Professor David A. Johnson, for directing me through this "interesting project", sending me to many conferences, telling me "focus just on one topic each time!", and finally, teaching me that "indeed, my family should be my first priority". I would also like to say special thanks to my PhD committee, Professors Cecile Devaud, Ali Elkamel, Ting Tsui, Kenneth Dale Visser and Serhiy Yarusevych for their support and constructive comments.

Thanks are also due to the Natural Sciences and Engineering Research Council of Canada (NSERC), Ontario Centres of Excellence (OCE), the facilities of the Shared Hierarchical Academic Research Computing Network (SHARCNET) and Compute/Calcul Canada, for their support.

I am grateful to Professor Joseph Katz from Johns Hopkins University for accepting me as a visiting student and to the researchers who shared their deep knowledge with me, in particular Professors Daniel Favier from Aix-Marseille University, David E. Rival from University of Calgary and Fulvio Scarano from Delft University and Dr. Shengyi Wang from Beihang University and Dr. Scott Schreck from NRELs National Wind Technology Center.

Best regards to the University of Waterloo faculty members, staff and technicians, in particular Professor John Medley, Professor Fathy Ismail, Martha Morales, Lisa Baxter, Jason Benninger, Gord Hitchman and Andy Barber. The assistance of Vivian Lam for the motion control setup, Mingyao Gu for taking PIV images and Pauline Lambert for LDA measurements is deeply appreciated. Also, thanks to my colleagues: Brian Gaunt, Michael McWilliam, Stephen Orlando, Adam McPhee, Erik Skensved, Drew Gertz, Adam Bale, Ahmed Abdelrahman, Nigel Swytink-Binnema, Rizwana Amin, Curtis Knischewsky, Nicholas Tam and all our co-up students.

A huge thank you to all my friends throughout my good times and bad times, and to the Waterloo birds who wake me up early in the morning.

My greatest gratitude goes to my parents, Tayebeh and Ali, my siblings and in-laws. No matter the distance, they are always with me and words cannot thank them enough.

Finally, to my loved ones. To my Madjid, always showing me my dream is his dream. I am here because of him. To my little son, Soroush, who has brought joy and happiness to my life. Indeed, he is the little magician who makes me full of energy when I am exhausted.

Dedication

This is dedicated to all women who demonstrate the possibility of having both a professional life and a happy family. Despite all their tiredness, they are strong and never stop smiling and sending out positive energy.

Table of Contents

List of Tables

List of Figures

Nomenclature

Roman Symbols

a	Freestream acceleration $[m/s^2]$
a_{DS}	Freestream acceleration during dynamic stall $[m/s^2]$
A	Vortex integration window $[m^2]$
c	Airfoil chord length $[m]$
C_d	Drag coefficient
C_l	Lift coefficient
C_P	Pressure coefficient
d	Drag force $[N]$
f	Frequency of oscillation $[1/s]$
h	LDA measurement domain in the y coordinate $[m]$
h_b	Height of the LSB $[m]$
k	Reduced frequency
k	Turbulent kinetic energy $[m^2/s^2]$
l	Lift force $[N]$
N	Number of samples
P	Pressure $[N/m^2]$

P_∞	Freestream pressure $[N/m^2]$
Re	Reynolds number
u	Stream-wise velocity $[m/s]$
$\overline{u_i' u_j'}$	Reynolds stress term $[m^2/s^2]$
U	Unsteady freestream velocity $[m/s]$
U_{DS}	Freestream velocity during dynamic stall $[m/s]$
U_{mean}	Mean freestream velocity $[m/s]$
U_∞	Freestream velocity $[m/s]$
v	Normal velocity $[m/s]$
V	Wind turbine inflow velocity $[m/s]$
W	Incident velocity $[m/s]$
W_{amp}	Incident velocity amplitude $[m/s]$
W_{mean}	Mean incident velocity $[m/s]$
x	Stream-wise direction
X_S	LSB separation location $[m]$
X_T	Laminar turbulent transition location inside LSB $[m]$
y	Normal direction
z	Span-wise direction

Abbreviations

CFD	Computational Fluid Dynamics
COS	Coupled Oscillating State (angle oscillation under unsteady freestream)
DS	Dynamic stall
$HAWT$	Horizontal Axis Wind Turbine

IA	Interrogation area
LEV	Leading Edge Vortex
LDA	Laser Doppler Anemometry
LSB	Laminar Separation Bubble
PIV	Particle Image Velocimetry
RMS	Root Mean Square
RPA	Axis A reference position (Galil software)
SOS	Single Oscillating State (angle oscillation under steady freestream)
TEA	Axis A position error (Galil software)
TEV	Trailing Edge Vortex
TPA	Axis A encoder position (Galil software)
TVR	Turbulent Viscosity Ratio
$URANS$	Unsteady Reynolds-Averaged Navier Stokes

Greek Symbols

α	Angle of attack $[^o]$
α_{amp}	Pitch amplitude $[^o]$
α_{mean}	Mean angle of attack $[^o]$
ε	Uncertainty
Γ	Circulation $[m^2/s]$
Δt	Time interval between PIV image pairs
$\Delta\alpha$	Phase delay $[^o]$
λ	Reduced amplitude
μ	Dynamic viscosity $[Pa.s]$

ρ	Fluid density $[kg/m^3]$
Φ	Phase difference between the oscillations $[^o]$
Ψ	Azimuth angle $[^o]$
ω_z	Spanwise vorticity component $[1/s]$

Chapter 1

Introduction

A Horizontal Axis Wind Turbine (HAWT) rotor usually operates with yaw errors or is subjected to wind disturbances as a result of complex environmental effects. These resultant yaw loads impact the performance of the wind turbine. HAWTs under yaw loads experience aerodynamically imbalanced rotors with regular performance affected significantly by over-predicted or under-predicted loads. During one wind turbine rotor revolution, the angle of attack as well as the incident velocity of each blade section varies. Since an idealized yaw load can be categorized as a periodic load, the wind turbine blade section under yaw loads can be modeled as an oscillating airfoil, and the blade element experiences an unsteady incident velocity as well. Studying unsteady airloads on wind turbine airfoils is important due to significant load variations and then the assumption of a steady angle of attack cannot be applied in particular when the angle of attack of the dynamic blade element passes through the dynamic stall angle. The dynamic stall phenomena, including energetic vortices, result in intensified aerodynamic loads. Many details regarding the dynamic stall vortex process as well as the corresponding aerodynamic loads remain unknown, and are the main subject of this study. This subject is also relevant to helicopter blade rotors, Vertical Axis Wind Turbines, maneuverable wings and Micro Air Vehicles.

This thesis is arranged in the following manner:

Chapters 2, 3 and 4: These three chapters provide a state-of-the-art overview, experimental description and the numerical simulation details, respectively.

Chapter 5: The dynamic stall phenomena were investigated with the PIV technique at the Reynolds number of 4×10^4 using the SD7037 airfoil. The PIV velocity fields

were post-processed to determine the loads and the pressure field by finding the sources of uncertainty and decreasing them for the challenging case of a dynamic airfoil. The effects of the reduced frequency on the laminar separation bubble (which is small for the dynamic cases), leading edge and rolling-up trailing edge vortices and aerodynamic loads will be discussed in detail. Because there is no literature regarding the dynamic SD7037 airfoil, a numerical simulation is considered as an alternative method of comparison.

Parts of this chapter have been published in the "ASME Fluids Engineering Conference" [32], "Applications of Laser Techniques to Fluid Mechanics" [31] and "International Symposium on Particle Image Velocimetry" [36] conference proceedings.

Chapter 6: Numerous investigations have been conducted to investigate large scale dynamic stall vortices but there is a significant lack of studies related to the flow structure for low angles of attack before dynamic stall phenomena. This chapter focuses on the real structures of these vortices, which usually appear as vortex sheets. A pitch oscillating S822 airfoil within the static stall angle has been considered for this chapter. The PIV method has been performed for visualization purposes as well as a numerical study as another alternative. LDA was used to measure the averaged drag values. Moreover, with the aid of LDA and the numerical simulation, the details of the wake structure have been investigated. There are no other publications studying the flow field of the pitching S822 airfoil.

This chapter was presented in the EUROMECH Colloquium 528 (February 22-24, 2012; Oldenburg, Germany). A related paper is also under second review to be published in the Springer book - proceedings series.

Chapter 7: Whether an unsteady freestream can affect dynamic stall behavior in terms of vortex processes and aerodynamic loads has been investigated in this chapter using the NACA0012 airfoil and numerical simulation at $Re \approx 10^5$. Because of the difficulties of creating a time-varying freestream experimentally, the usefulness of Computational Fluid Dynamic (CFD) approaches is apparent. No CFD simulation study has been completed thus far to investigate the interaction of a pitch oscillating airfoil with an unsteady freestream velocity with the application in HAWTs (the same oscillation frequencies with high amplitude). The NACA0012 airfoil has been chosen since there are enough experimental studies related to pure pitch oscillating cases in the literature.

An article including these results is under publication in the "*Journal of Fluids and Structures*" [35].

Chapter 8: This chapter is a continuation of Chapter 7 investigating the effects of airfoil shape and Reynolds number on the behavior of the dynamic stall phenomena under an unsteady freestream. For this purpose, the unsteady flow field around a pitching S809

airfoil at Re=10^6 was simulated numerically. Moreover, the effects of a full range of phase differences between oscillating systems (oscillating airfoil and oscillating freestream) are considered in detail.

Some results regarding the S809 airfoil have been presented at the "Green Energy Conference IGEC V" [33] and published in the "*Journal of Applied Energy*" [34]. Another manuscript has also been submitted to a scientific journal and is under second review.

Chapter 9: The main points of this dissertation are highlighted.

1.1 Objective

The first step of this study was started with questions regarding the dynamic stall phenomena that a HAWT blade element faces and the ability of state-of-the-art techniques to capture the details of this phenomena. Although a few manuscripts have been published very recently regarding some of these questions, the lack of research in this area needs to be addressed. The questions that have motivated this study are as follows:

1. Can the control-volume approach based on the PIV velocity field (which has been used for static objects) determine reliable aerodynamic loads for a dynamic airfoil?

2. How can the accuracy of the calculated PIV loads be improved?

3. How do dynamic stall vortices impact each other?

4. How does the calculated pressure field from the PIV velocity field coincide with the vortical structure of the dynamic stall phenomena?

5. What is the influence of the reduced frequency on the laminar separation bubbles and dynamic stall vortices?

6. What is the nature of a vortex sheet?

7. Do the results of an oscillating angle of attack within static stall angle differ from those of the static angle?

8. Is the incident velocity variation periodic for a rotor of a HAWT under yaw loads?

9. How does the combination of an unsteady incident velocity and unsteady angle of attack (Coupled Oscillating State) affect the dynamic stall loads?

10. Is the overall performance of the vortices from the Coupled Oscillating State the same as that of just angle of attack oscillation?

11. What is the contribution of a vortex sheet?

12. Are the results from the Coupled Oscillating State affected by the Reynolds number and the airfoil type?

This dissertation has been organized to answer these questions.

Chapter 2

Background

2.1 Horizontal Axis Wind Turbine (HAWT)

With today's high demand for renewable energy, wind turbines have been the subject of much ongoing numerical and experimental research. In terms of efficiency and robustness, the Horizontal-Axis Wind Turbine (HAWT), a lift-based propeller type turbine, is the current choice especially for commercial firms [15] for $Re > 6 \times 10^5$ [120], where

$$Re = \rho c U_\infty / \mu \tag{2.1}$$

and ρ and μ are the air density and viscosity respectively, c is the airfoil chord length and U_∞ is the mean freestream velocity. Recently, small HAWTs have become very practical, with extensive applications such as in sailing, remote communities, micro grids and farms [81]. Considering the airfoil elements from root to tip of a small HAWT blade under normal operation, the Reynolds number that an airfoil element can experience starts at approximately 3.8×10^4 [111].

Frequently, natural wind has a strong wind shear with altered direction and velocity magnitude which results in yaw loads [15, 42]. In some cases, the rotor of the wind turbine also operates under yaw errors regardless of the wind conditions [42]. The amount of power produced by a HAWT under yaw loads is very uncertain, has a significant impact on the performance of the turbine and causes fatigue damage. Ambiguities in force determination in different flow conditions are the main reasons for these uncertainties. Studying yaw loads is important even for pitch controlled [58] and small HAWTs [41, 61, 74, 138]. Therefore, in wind turbine technology, there is a great demand for further research on unsteady aerodynamic forces.

2.1.1 Yaw loads

Figure 2.1 shows two different potential wind disturbances that cause yaw loads for a HAWT [42]. In this figure, the six o'clock position is the zero azimuth angle, $\Psi = 0$. The positive horizontal crossflow (Figure 2.1-a) is the resultant of the yaw angle, which indicates the mean inflow vector makes an angle with the rotor axis. With a positive horizontal crossflow V_y, the advancing blade is on the rotor side ($\pi/2 < \Psi < 3\pi/2$) where the direction of the air velocity vector from the blade rotation ($r\Omega$) and the direction of the crossflow V_y are the same. On the contrary, the retreating blade is on the rotor side ($3\pi/2 < \Psi < \pi/2$) where the direction of the air velocity vector from the blade rotation and V_y are opposite. Figure 2.1-a (last row) shows that at π azimuth, the blade element has the minimum angle of attack and the incident velocity reaches its maximum value; at $\Psi = 0$, the representative blade element has a maximum angle of incidence and is subjected to the minimum incident velocity. The periodic oscillations of the angle of attack and incident velocity occur with the same frequency but with π phase difference.

Positive horizontal shear (Figure 2.1-b) is one of the consequences of spatial variation of horizontal inflow velocity along the rotor for many reasons including upwind obstructions. In this situation, each blade element is facing a maximum angle of incidence and a maximum incident velocity when the magnitude of the horizontal inflow is the highest ($\Psi = \pi/2$). The reverse condition (a minimum angle of incidence and a minimum incident velocity) occurs at the lowest magnitude of the horizontal inflow ($\Psi = 3\pi/2$). In this condition, both the angle of attack and the incident velocity are oscillating in one cycle with the same frequency while they are in phase.

Oscillating airfoils with application to HAWTs have been studied numerically and experimentally. The incident velocity also shows an oscillating behavior which was unfairly ignored in previous wind turbine studies [58] but has now become a topic of very recent research [99].

These two examples show that when the rotor is under yaw loading, the angle of attack and the incident velocity can oscillate with a wide range of phase difference, Φ, from in-phase to out-of-phase. This study discusses the effects of the phase difference, as it changes in a wide range as a result of different yaw loads or combinations of them. Since this study focuses on a 2D airfoil, the freestream velocity oscillation is the same as the incident velocity oscillation.

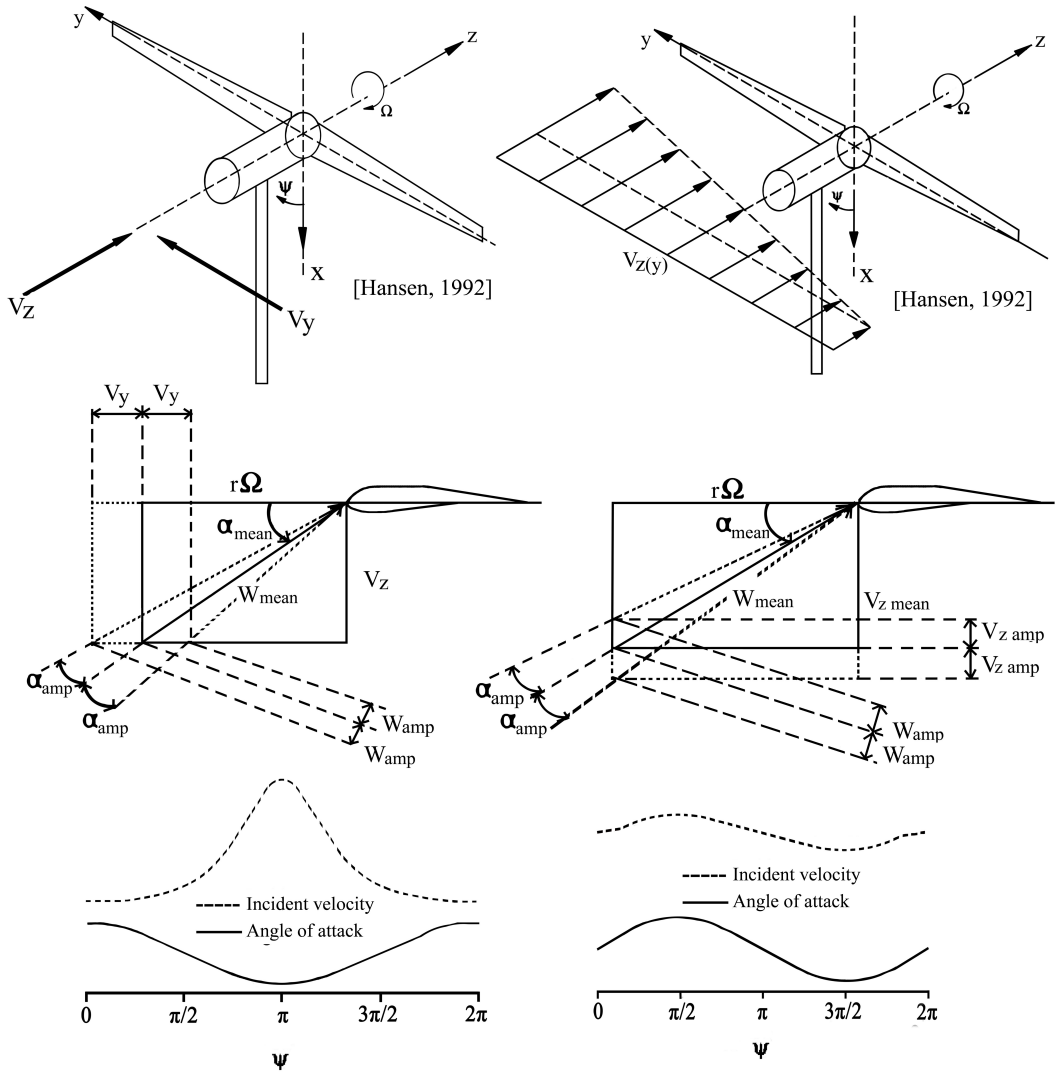

(a) Positive horizontal crossflow

(b) Positive horizontal shear

Figure 2.1: Two types of wind disturbances causing yaw loads; a) positive horizontal crossflow/yaw error, V_y; b) positive horizontal shear, $V_z(y)$; top figures from [42] with permission.

2.2 Sinusoidally oscillating airfoils and dynamic stall

An airfoil oscillates about the 1/4 chord location according to the sinusoidal mode:

$$\alpha = \alpha_{mean} + \alpha_{amp} \ \sin(2\pi f t) \tag{2.2}$$

where α_{mean}, α_{amp} and f represent mean angle of attack, pitch oscillation amplitude and oscillation frequency, respectively. The harmonic oscillation provides a positive pitch rate for half the cycle, the upstroke ($\uparrow$), and a negative pitch rate for the second half, the downstroke ($\downarrow$) with the reduced frequency k,

$$k = \frac{\pi f c}{U_\infty}. \tag{2.3}$$

Since pitch oscillating airfoils provide load variation in one cycle, understanding the details is critical for designing and controlling systems operating under these conditions. Load variation will be more significant if an unsteady angle of attack passes the static stall angle. If the effective angle of attack of a lifting surface subject to unsteady motion exceeds its static stall angle, dynamic stall occurs [59, 68]. The combination of stall phenomena, inherently unsteady, and unsteady angle of attack motion results in delay of stall, the development of a dynamic stall vortex and the loads exceeding the static one. Dynamic stall lift augmentation was first reported by Kramer [98]. Lift augmentation is considerable since dynamic stall lift values can be more than twice the static stall ones [19]. Dynamic stall phenomena associated with pitch oscillating airfoils have been considered for many years, with a wide range of applications such as helicopter blade rotors, wind turbine blades and maneuverable wings. For more than two decades, McCroskey and his colleagues made tremendous efforts to investigate the details of the dynamic stall phenomena [53, 62]. McCroskey also published two excellent reviews related to this study [65, 66]. However, although extensive recent experimental studies [56, 57, 89, 93, 100, 132] as well as numerical studies [8, 24, 70, 107, 108, 118, 129, 132, 143] have been reported, dynamic stall issues have not been addressed completely.

The stages of dynamic stall events are presented in Figure 2.2 for the NACA0012 airfoil. As the airfoil passes the static stall angle the boundary layer behaves differently from the static airfoil, with no separation. The majority of the flow is attached to the airfoil [17, 59, 68], with global behavior similar to that of the steady airfoil before stall. Gradually, flow reversal appears at the rear of the airfoil, resulting in a thicker boundary layer at the rear portion. For $0.005<x/c<0.3$ of the leading edge, the boundary layer breaks down or separates upstream of the flow reversal and a Leading Edge Vortex (LEV)

forms and then the lift-curve slope increases. The maximum lift value occurs when the vortex meets the trailing edge [59] and then an abrupt lift drop is experienced with vortex shedding [17, 56, 57, 62, 64, 68]. McCroskey classified dynamic stall as either light or deep [66]. For a low maximum effective angle of attack, slightly higher than the static stall angle of attack, a light dynamic stall occurs. The thickness of the separated flow at the trailing edge, the viscous layer, is on the order of the thickness of the airfoil. A deep-stall regime is the result of a high maximum angle of attack. The vortex dominates, the thickness of the viscous layer increases to the order of the airfoil chord, and most notably for aerodynamic loads, significant load augmentation is observed [17]. A second LEV forms in the fully separated flow. This vortex carries a relatively low pressure wave and causes a second lift peak [62, 68, 82]. Flow reattachment from the trailing edge to the leading edge gradually occurs after the static stall angle during downstroke, with the speed of $25 - 35\%$ of the freestream velocity [17, 68]. To satisfy conservation of circulation (Kelvin's circulation theorem),

$$\frac{D\Gamma}{Dt} = 0, \tag{2.4}$$

a counter-clockwise rotating vortex called the Trailing Edge Vortex (TEV), which is another source of circulation, appears [85]. A TEV diminishes the lift value [98] and appears in the form of either a vortex sheet or a roll-up vortex. During post stall, the shed LEV and TEV in the form of a vortex pair looking like a mushroom, called a mushroom-wake structure, convect downstream to reach the freestream velocity asymptotically [82]. The shape of the TEV, the time its shape is changed, and its contributions to lift reduction are important subjects of this study.

One of the dominant motion parameters in dynamic stall phenomena is the frequency of oscillation. Decreasing the reduced frequency advances LEV formation and dynamic stall with the lower LEV strength [52, 64, 68, 82]. This current study looks at the effects of reduced frequency on dynamic stall phase delay as well as the locations of the vortices before and after stall in detail.

Although airfoil geometry can affect static stall characteristics, it is not a dominant parameter compared to the motion parameters that influence deep dynamic stall characteristics [69]. The Reynolds number also has only small effects on dynamic stall characteristics [17]. In this study, the effects of an airfoil's shape and the Reynolds number on dynamic stall will be discussed, but unlike in previous studies, here the freestream velocity is unsteady.

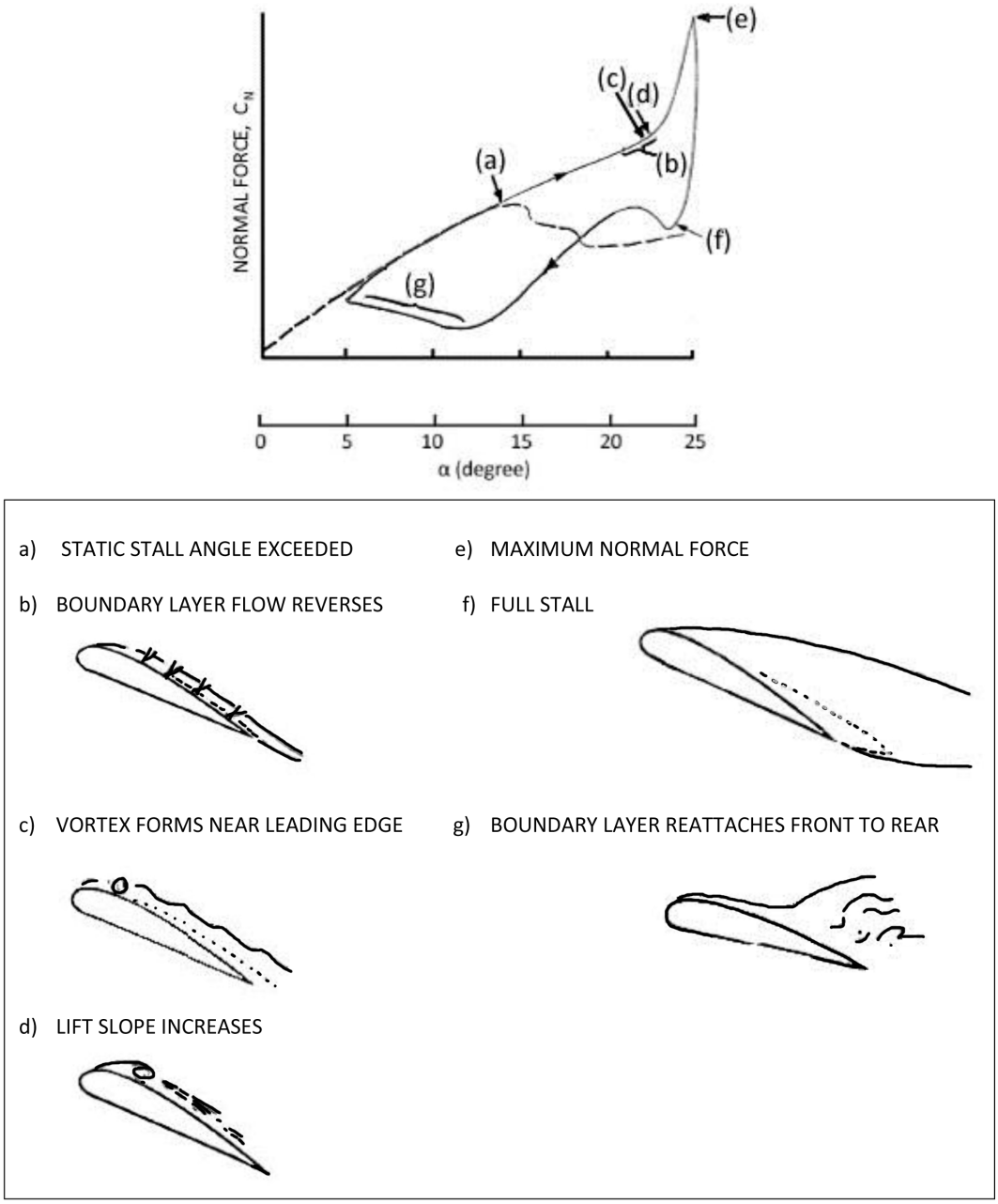

Figure 2.2: Schematic of the dynamic-stall events for NACA0012 airfoil, $k = 0.15$ and $Re = 2.5 \times 10^6$; adapted from [17].

2.3 Oscillating freestream velocity

A time-varying freestream velocity is one of the important parameters for unsteady aerodynamic loads. Theoretical and experimental studies have shown that the effects of the time-varying freestream velocity are more significant in the presence of separated and dynamic stalled flows. Pierce et al. [54, 84] conducted experiments to demonstrate the effects of the accelerating and decelerating unsteady freestream during pitch oscillation of the airfoil when the frequency of the airfoil pitching was different from that of the freestream. Favier et al. [27, 28, 29] used fore-and-aft translational motion of the airfoil in a steady freestream velocity to simulate relative instantaneous velocity variation. Based on their results, the phase difference between the unsteady velocity and the periodic angle of attack changed the magnitude and behaviour of the aerodynamic loads significantly. Favier continued this work using laser based techniques [12] and CFD modeling [26, 63]. Most of the above studies are based on the aerodynamics of helicopter rotors. In very recent studies, experiments were reported by Shi and Ming [109, 110] with pitching delta wings under an unsteady freestream velocity with application to a maneuverable delta wing. The results showed that a decelerating freestream velocity during pitch up can delay the dynamic stall angle. In some studies, regardless of their applications, a gusty environment was presented as a longitudinal oscillating freestream [60, 86, 87]; because of the nature of the gust, the amplitudes of the oscillations are usually low with great variation in the frequency of the oscillations.

As mentioned, in some of the previous studies, instead of an oscillating freestream, the equivalent movement of the body in a steady flow was studied. Recently, Wong et al. [137, 136] compared these two cases for a flat plate and showed that oscillation of the body instead of the oscillation of the freestream are not equivalent even at low frequencies; thus, in the rest of this study, an unsteady freestream means an oscillating freestream.

For a sinusoidally varying freestream, the horizontal velocity was oscillating governed by:

$$\frac{U(t)}{U_\infty} = 1 + \lambda \ \sin\left(2\pi f t + \Phi\right) \tag{2.5}$$

where λ is the reduced amplitude, defined as

$$\lambda = \frac{U_{amp}}{U_\infty} \tag{2.6}$$

and U_∞ of the steady freestream is considered as U_{mean}, with Φ representing the phase difference between the oscillation of the airfoil and the oscillation of the freestream velocity.

Because of the difficulties of creating a time-varying freestream experimentally, the problem of a time-varying freestream velocity is usually ignored. Thus, the usefulness of a Computational Fluid Dynamics (CFD) approach for evaluating this problem is apparent [59] and is the main focus of Chapters 7 and 8. As with the amplitude of pitch oscillation, increasing the incident velocity amplitude amplifies oscillation effects [58]. Since the amplitude of the incident velocity can be large for wind turbines [58], the value of $\lambda = 0.6$ has been considered for this study.

2.4 Laminar Separation Bubble (LSB)

For a low Reynolds number, when a laminar boundary layer transits to a turbulent one, it may form a Laminar Separation Bubble (LSB) at certain angles of attack. Since the airfoil/object geometry is an important parameter determining the existence of an LSB and its size, there are many variations in the literature. Carmichael for $3 \times 10^4 \leq Re \leq 7 \times 10^4$ [16] and Pelletier and Mueller for $6 \times 10^4 < Re < 2 \times 10^5$ [83] reported that no LSB was observed while according to Ol et al. [78], an LSB was observed at $Re = 6 \times 10^4$ while different types of the airfoil were tested by those researchers. That means, besides the Reynolds number values, the type of the airfoil is also important for LSB formation. Aerodynamic efficiency, the ratio of the lift/drag, is reduced in the presence of an LSB [6, 101]. Figure 2.3 shows a schematic of an LSB by Horton [44]. When laminar flow near the leading edge cannot resist the adverse pressure gradient, the attached flow starts to separate. Since the flow at the separated boundary layer is very sensitive to disturbances, laminar to turbulent transition occurs after separation close to the airfoil surface [6, 7]. The turbulent flow improves momentum transfer causing reattachment and forming a recirculation region called the LSB [6, 7, 88]. The turbulent boundary layer keeps the flow attached after the LSB [88].

Angle of attack also influences LSB characteristics. As the angle of attack increases, the laminar separation moves forward [45, 79]. As the Reynolds number is increased, the height of the bubble is decreased while the reduction rate of the height is higher than that of the length [22, 79].

For the dynamic case, as the incidence increases, the airfoil shows the same characteristics as in the static case [47, 57, 64]. The LSB length of a dynamic airfoil decreases significantly compared to that of the static case, while the LSB length is not sensitive to the frequency of the oscillations [57]. Although LSB characteristics are not yet fully understood, for an unsteady airfoil, the temporal aspect makes the study of the LSB even more complicated. This study investigates the effects of the reduced frequency on LSB height at

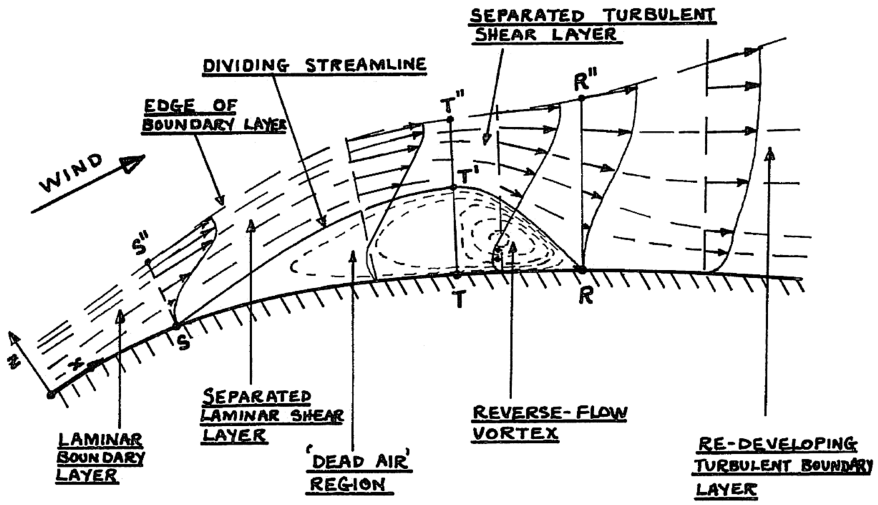

Figure 2.3: LSB sketch by Horton [44].

different oscillation frequencies. The LSB height can be used as an indicator instead of the LSB length since the length of the LSB does not change versus the frequency noticeably with a smaller size than that of the static case [57].

2.5 Force measurement from the velocity field

For measuring unsteady aerodynamic loads of small wind tunnel models, applying fast-response miniaturized pressure sensors [95] and a direct force measurement technique [97] are not practical. Challenges regarding these methods indicate the importance of calculating aerodynamic loads based on velocity fields from new techniques such as the PIV method.

The control-volume approach has been applied recently in PIV velocity fields to determine the aerodynamic forces on an object. In 1997, Noca et al. [76] calculated forces around a stationary circular cylinder by applying the control-volume approach while the pressure term was eliminated analytically. Unal et al. [122] applied the control-volume approach by considering the pressure term for the oscillation cycle of a circular cylinder. Because of the low accuracy of the processing algorithms at that time and the limitations of the experimental equipment, this method was not much used by other researchers. In 2006, Scarano and Van Oudheusden with their colleagues at Delft University started using this technique to evaluate loads for a stationary airfoil [18, 116, 123, 124, 125] and for a

square cylinder [127]. They also applied this approach for the time-resolved PIV technique to evaluate unsteady aerodynamic forces on a static square cylinder[55]. Since 2011, they extended this technique to examine dynamic airfoils [43, 91, 92]. Very recently, David et al. [21] and Rival et al. [95] also calculated aerodynamic loads of dynamic airfoils based on this approach. Load calculation based on the control-volume approach of PIV velocity fields has been extensively validated for static objects. The dependency of the unsteady forces of dynamic airfoils on many parameters makes applying this technique for dynamic airfoils more complicated. This study seeks ways to increase the accuracy of this method for dynamic airfoils and to make it more reliable for further studies.

It should be mentioned that the aerodynamic loads based on unit span can be normalized with the mean freestream velocity

$$[c_l, c_d] = \frac{[l, d]}{\frac{1}{2}\rho {U_\infty}^2 c} \tag{2.7}$$

where l and d are the lift and drag forces.

2.6 Airfoil selection

SD7037 airfoil: This airfoil shown in Figure 2.4a was designed in 1987 by Selig and Donovan with application in sailplanes at low Reynolds numbers. Experimental studies investigated the use of SD7037 for small wind turbines [37]. Based on the lift and drag data from its smooth and rough surfaces, the maximum lift coefficient of the SD7037 is insensitive to leading-edge roughness; therefore, it is a good candidate for wind turbines. Moreover, the SD7037 has a large drag bucket (a high lift range for low drag) [37]. The static SD7037 airfoil was also smoothed, named SD7037(c), and tested for $Re \geq 0.6 \times 10^5$ [104]. The smoothed coordinates have been used in this study.

NREL airfoils: The S822 shown in Figure 2.4b and S809 shown in Figure 2.4c airfoils from the S series family were designed by the National Renewable Energy Laboratory(NREL) specifically for Horizontal Axis Wind Turbine blades [120]. The S822 is a thick airfoil designed for the tip of the blade. Many experimental studies have reported on the static S822 airfoil for $Re \geq 10^5$ [37, 105, 106, 114, 115]. For the static S809 airfoil Somers [113] reported aerodynamic coefficients, while the measurements were taken at Delft's low-speed low-turbulence wind tunnel. Pitch oscillating studies of the thick S809 airfoil have been considered for almost two decades. Ramsay et al. [93] tested a two dimensional S809

airfoil under stationary and dynamic conditions. In the dynamic case, the airfoil underwent pitch oscillations at different mean angles of attack and oscillating amplitude for $Re > 0.75 \times 10^6$. The effects of airfoil roughness were also considered in their study. The dynamic S809 airfoil has been studied recently by semi-empirical strategies as well as CFD methods [34, 40, 108, 143].

NACA0012 airfoil: This airfoil shown in Figure 2.4d has been evaluated in many theoretical and experimental studies and extensive information about its characteristics during dynamic stall have been reported [17, 30, 57].

In this study, the unsteady freestream velocity are examined with the NACA0012 and S809 airfoils since the dynamic stall characteristics of these airfoils under a steady freestream exist. For the rest of the investigation, the SD7037 and S822 airfoils are used.

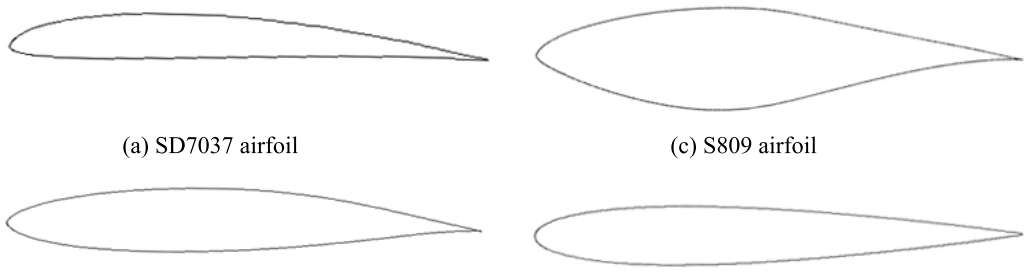

(a) SD7037 airfoil

(c) S809 airfoil

(b) S822 airfoil

(d) NACA0012 airfoil

Figure 2.4: Selected airfoils; a)SD7037 airfoil [104], b)S822 airfoil [120], c)S809 airfoil [120] and d)NACA0012 airfoil.

Chapter 3

Experimental Setup

3.1 Wind tunnel

Experiments have been performed in a low speed closed circuit wind tunnel shown in Figure 3.1, built by Sperandei [119], located in the Turbulent Flow Lab of the University of Waterloo. A frequency controlled axial fan accelerates the air flow through the test section. The test section is made of $3mm$ thick float glass which is suitable for laser based tests. Orlando [80] modified the wind tunnel by adding two turbulence reduction screens, made of fine metal mesh installed before the contraction. With this modification, the upstream turbulent intensity is 0.85% for 10m/s air velocity and it decreases to 0.75% with 35m/s air velocity.

Wind tunnel calibration was completed with a manometer and a pitot tube in the empty test section after cleaning the turbulence reduction screens as shown in Figure 3.2. The behavior of the air velocity versus the fan setting is almost linear (Inlet wind velocity = 0.6× Fan setting - 1.1). The error of inlet velocity is around 0.14 m/s by considering two sets of velocity calibrations taken with a one week interval.

3.1.1 Two dimensional wind tunnel

The two dimensionality assumption of the wind tunnel was examined by the oil film visualization technique [80]. Figure 3.3 shows the boundary layer development at $Re \approx 10^5$ for the S822 airfoil at $\alpha = 3^o$. The laminar boundary layer covers the leading edge until the boundary layer is separated at the separation oil line. The turbulent boundary layer is

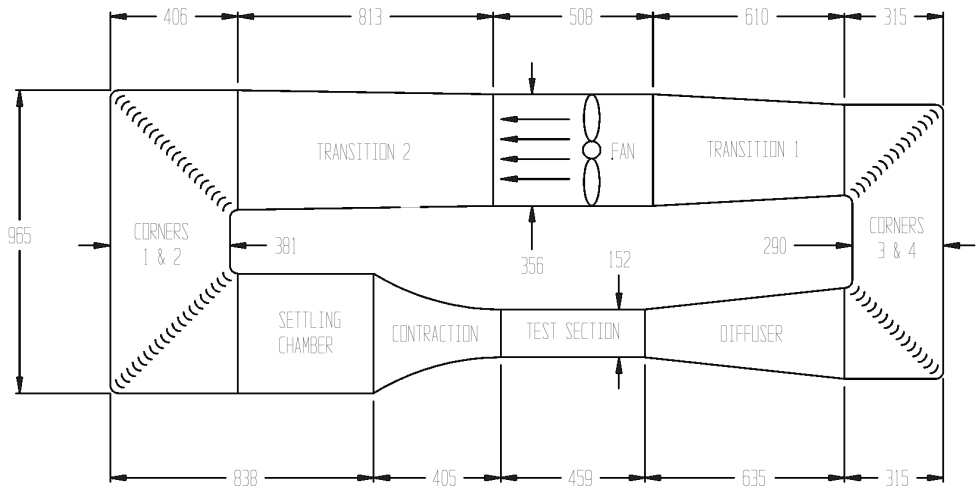

Figure 3.1: Wind tunnel schematic [119]; Dimensions in mm.

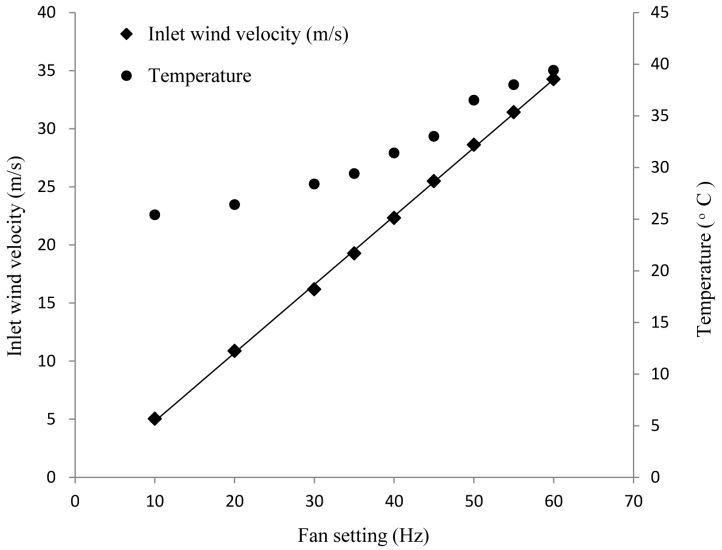

Figure 3.2: Wind tunnel calibration of temperature [80] and inlet wind velocity.

reattached to the suction surface at the reattachment oil line to form a laminar separation bubble. More than 80% of these two oil lines are parallel to the spanwise length of the blade indicating the two-dimensional flow field. Three-dimensionality found in less than 20% of the blade close to the wind tunnel walls and they do not affect the mid-span of the blade where the data were taken. Wind tunnel wall effects are also decreased with a dynamic airfoil [17, 97].

The blockage ratio of the wind tunnel,

$$Blockage\ ratio = \frac{Model\ frontal\ area}{tunnel\ cross\ section\ area}, \tag{3.1}$$

limits either the size of the airfoil or the maximum angle of attack since the maximum recommended blockage ratio is 7.5% [9]. The speed range of the wind tunnel also dictates a low Reynolds number study.

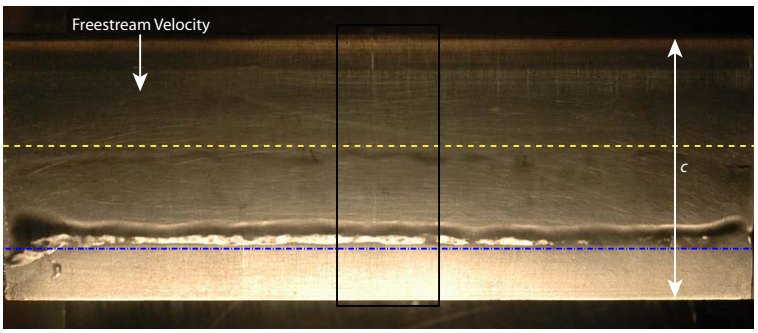

Figure 3.3: Oil film visualization for the S822 airfoil at $\alpha = 3^o$, $Re \approx 10^5$ [80]; ___ separation oil line; _._ reattachment oil line; | | midspan of the blade where the measurements were taken.

3.2 Airfoil information

For the deep dynamic stall study, the chord length of 26 mm with the maximum angle of attack of 22° was considered. Based on a Reynolds number of 4×10^4, the SD7037 airfoil was chosen. The 3D blade was designed to attach from one end, Figure 3.2. A three-axis CNC mill with 0.025 mm tolerance machined the airfoil and its attached shaft from one piece of 6061 aluminum. The airfoil was polished and painted in black to minimize the

laser beam reflection. Measured with a caliper, the chord length and thickness of the airfoil are 25.92mm and 2.38mm, respectively. An angular adjustment device was machined to fix the location of the airfoil at zero angle of attack, Figure 3.5.

To maximize the range of the Reynolds number($Re = 10^5$), the S822 airfoil, designed for this range of Reynolds number, was selected. The chord length of 55mm was chosen with the maximum angle of attack of 8°. For the S822 airfoil, at the angle of attack of 8°, maximum lift to drag ratio occurs [103]. The S822 airfoil for the current experiment was built and documented by Orlando [80].

3.3 Dynamic motion control

A layout of the airfoil motion control is shown in Figure 3.6. A rigid shaft coupling (Ruland $CLX\_4\_4\_F$; see Appendix A for details) connected the shaft of the airfoil to the shaft of the motor, Figure 3.2. The coupling tolerates the maximum rotational speed of 4000 rpm/60Hz, which is more than enough for this setup.

To actuate the airfoil, a brushless servo motor (T0603-A0-N-CG-N-F-A-A Cleveland Motion Controls MDM-5000; Appendix A), Figure 3.2, was selected based on the size of the airfoil, the desired RPM, and the anticipated loads. The servo motor features 8000 counts or 22 positions within a single degree of shaft rotation. With this, it is possible to do high precision motion such as quick oscillations or consistent rotations. Due to its relatively low rotor inertia, it is able to quickly shift speeds, either accelerating, decelerating, or even changing direction making it suitable for sinusoidal oscillations. In continuous rotation, its maximum speed is 508RPM/8 Hz for 360 degree when provided with a 24VDC/12A power supply; then, for a sinusoidal mode with 11 degrees amplitude, the rotor can rotate much faster. The recommended PSR power supply from Galil Company (PSR-12-24; Appendix A) was used.

A single axis PID controller and drive (Galil Motion Controls CDS-3310; Appendix A) was used to operate the servo motor. The digital and analog outputs make triggering external systems such as the PIV processor in the actual position of the shaft possible. Its maximum encoder feedback rate was 12 MHz, and its minimum control loop update time was 250 microseconds. It interfaces with the computer via a RS-232 serial port or an Ethernet cable. The Ethernet cable was recommended if the scope of the Galil software is used.

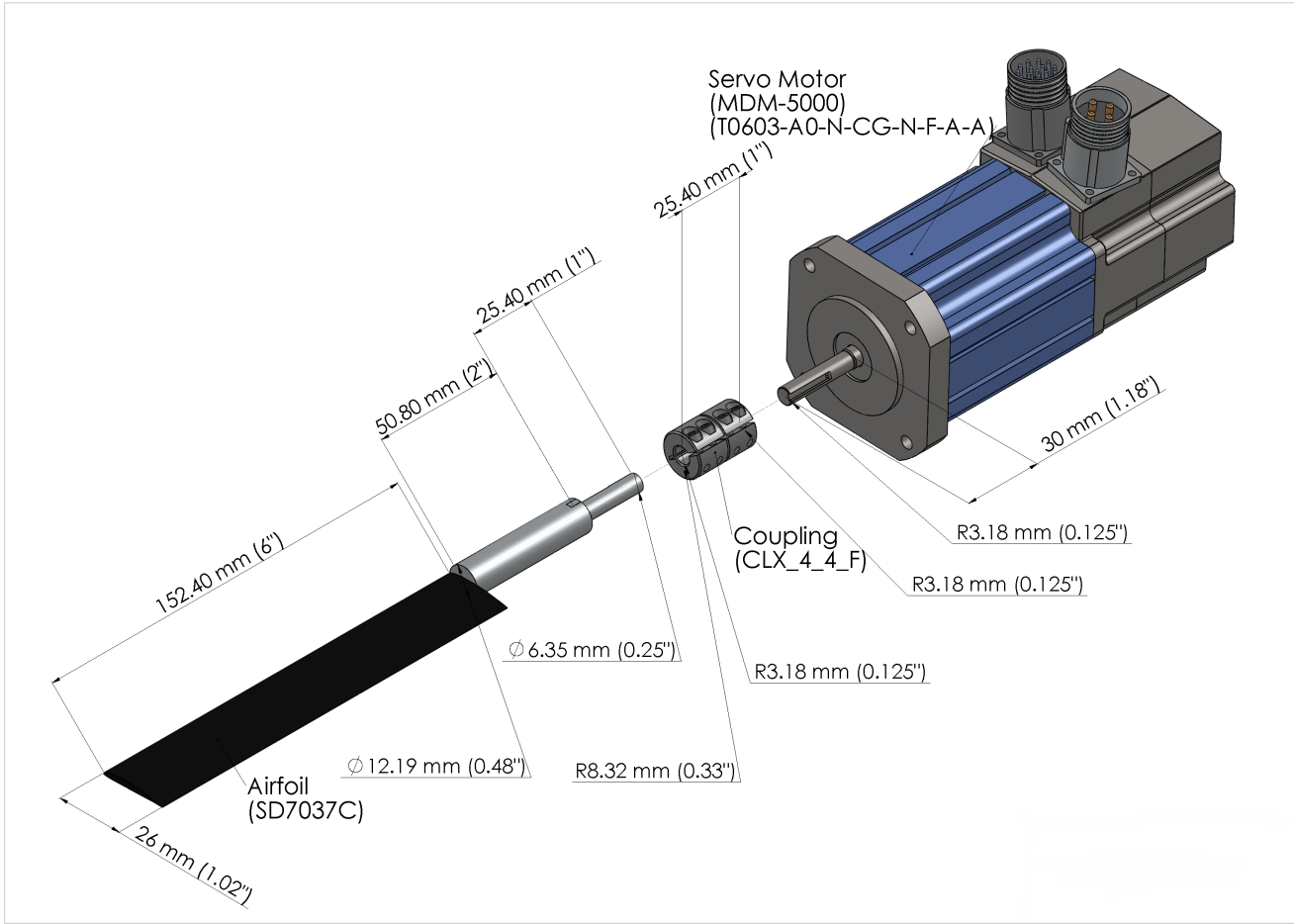

Figure 3.4: 3D view of the SD7037 airfoil, coupling and servo motor.

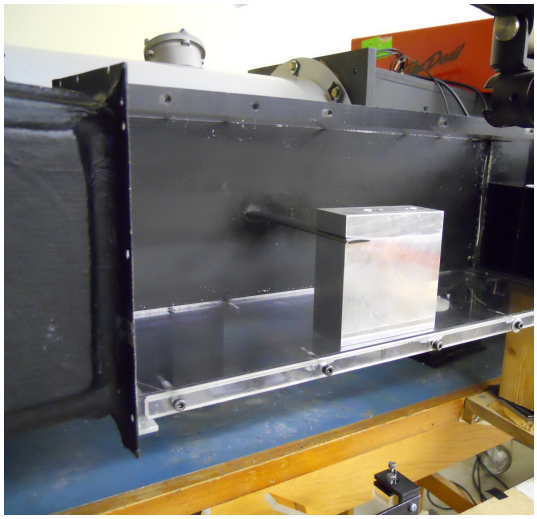

Figure 3.5: Angular adjustment device for zero angle of attack

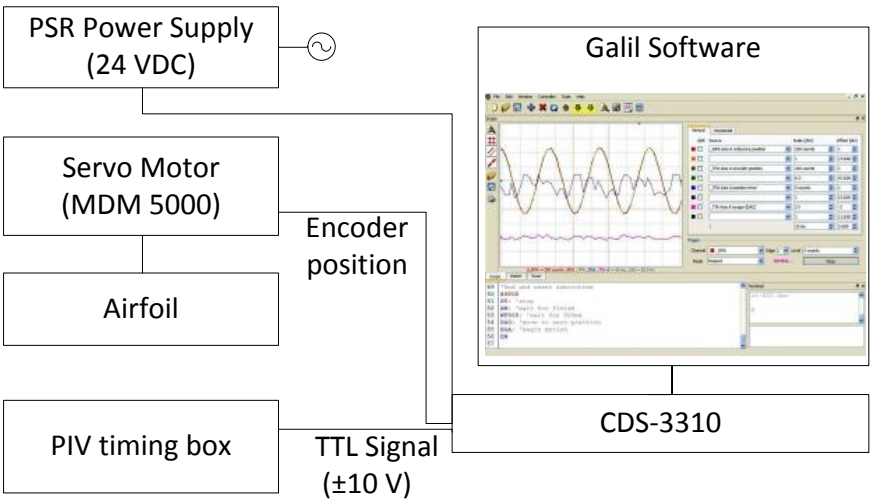

Figure 3.6: Motion control layout

3.3.1 Galil software

To produce sinusoidal motion, the controller's vector mode is used, which is intended to guide a two-axis system along a prescribed profile on a 2D plane of motion. Vector mode can still be used with a single-axis controller to generate sinusoidal motion. A program in vector mode is provided in Appendix B. The optimum performance significantly depends on the process of tuning a PID (Proportional, Integral, and Derivative) filter[1]. If one of the oscillation parameters, such as the weight of the oscillating object, amplitude, or frequency of the oscillations, is changed, the tuning parameters should be modified. The scope of the software can show "RPA Axis A reference position", the calculated position from the program which can be used as a reference to compare with, "TPA Axis A encoder position", the actual position of the axis which should be matched with the RPA, "TEA Axis A position error" which shows the difference between RPA and TPA values. Figure 3.3.1 shows the scope for these parameters for 15Hz frequency and 244 counts (11 degree) of amplitude; the maximum error for pitch up motion is 3 counts and for pitch down motion is 6 counts. These values are almost repeatable for each cycle. For triggering the PIV system, the OC function has been chosen. This function sends the TTL signal to channel 23 based on the main encoder position at each cycle and can trigger the external system for rise down step. For example, OCA=44 means to trigger the system when the actual position of the shaft meets 44 counts (angle of attack of 2 degree). A Labview code was used to invert the polarity of the trigger signal, since the PIV Timer Box (Section 3.5.1) does not accept a negative polarity. For triggering the PIV system, the scope of the Galil should be closed to minimum the signal time lag.

3.4 Laser Doppler Anemometry (LDA)

Laser Doppler Anemometry (LDA) is a non-intrusive optical method for measuring velocity components with a high data rate at a specific position in a flow and has frequently been used for measurement in the wake of airfoils [12, 13]. Principles of the LDA can be found in Albrecht et al. [5]. For the purpose of this study, the LDA is used to measure the velocity flow field in the wake of an S822 airfoil with the Reynolds number of 10^5 for both static and sinusoidally oscillating cases. A Dantec FiberFlow LDA system with a Coherent Innova 70, 5 W Argon Ion laser was used for the measurements. The laser beam passing through a Dantec 60X41 transmitter is divided into green (wavelength of 514.5nm), blue

[1] http://www.galilmc.com/support/appnotes/optima/note3413.pdf;
http://www.galilmc.com/support/appnotes/miscellaneous/note5491.pdf.

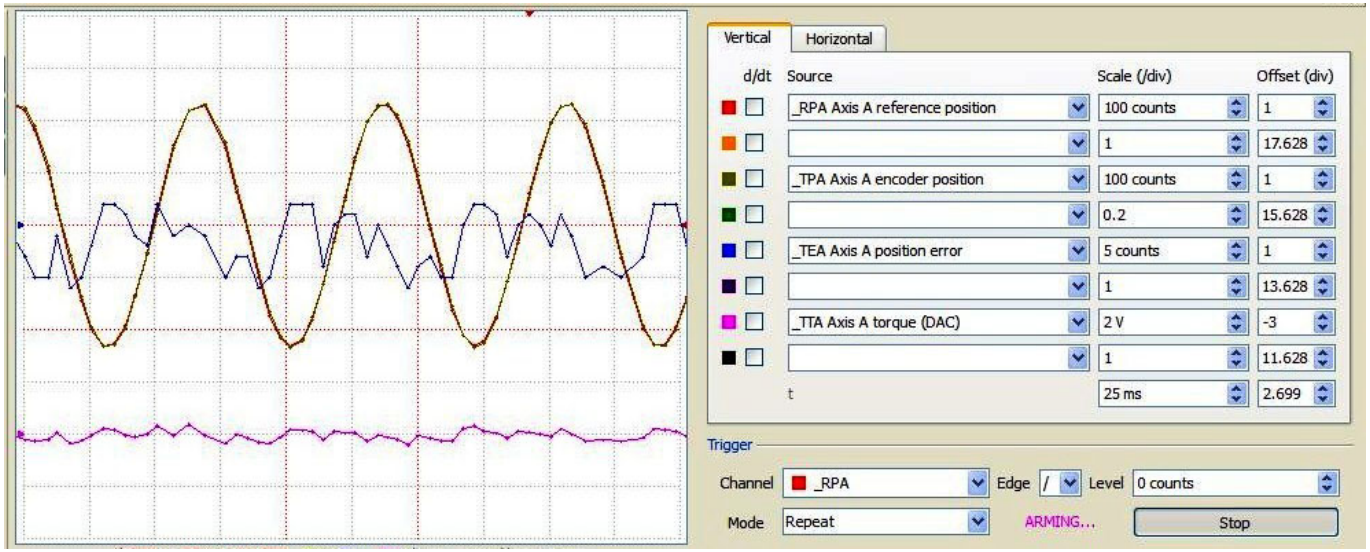

Figure 3.7: Galil scope function showing the reference position (RPA), encoder position (TPA) and position error (TEA) for 15Hz of frequency and 244 counts of amplitude.

(wavelength of 488nm) and violet (wavelength of 476.5nm) light while the violet light has been used just for beam alignment. The two-component Dantec 60X81 probe is in back scatter setup, the receiver and the incident light are located on the same side. The probe includes a 310mm 50X57 focal length lens and a 55X12 beam expander. The LDA bias error is based on the error of beam separation distance which is negligible on the measured velocity [5]. A three-axis traverse was used to mount and move the LDA probe with the accuracy of 0.013mm, 0.013mm and 0.0063mm in x, y and z directions, respectively. Since the vertical direction in the wake of the airfoil is considered, this direction is chosen as the z direction. To acquire a high data rate for velocity components, the probe is rotated 45 degrees, Figure 3.8, with the following magnitudes of the transverse and streamwise velocities [5]:

$$\begin{aligned} U_x &= U_{blue} \cos\frac{\pi}{4} + U_{green} \sin\frac{\pi}{4} \\ U_y &= U_{green} \cos\frac{\pi}{4} - U_{blue} \sin\frac{\pi}{4}. \end{aligned} \tag{3.2}$$

The rotation of the probe has $\pm 0.5^o$ uncertainty, but inserts negligible bias error on the measured velocity [80]. The precision errors are reported in Appendix C.

BSA Flow software controlled the traverse and analyzed the returned raw information [2]. The LDA measurements were taken on the middle of the airfoil span with the specific measurement location at $x/c = 1.25$ from the trailing edge. An order of 10^5 data points were collected for each experiment. Dynamic cases needed more data points compared to the static case and increasing the reduced frequency of the oscillations increases the number of data points. More details of the LDA setup with a static airfoil were explained in Orlando [80] and Skensved [112].

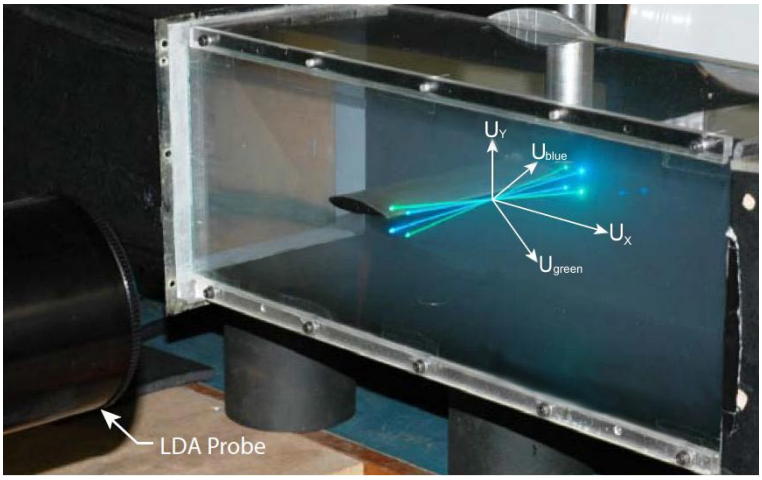

Figure 3.8: Rotated LDA probe[80]

3.4.1 Mean drag coefficient

Bohl and Koochesfahani determined the mean drag load on an airfoil using the integral momentum theorem [14]. Figure 3.9 shows the control volume definition for this analysis. In this figure, a pressure gradient exists in the wake of the airfoil which can be replaced by the Navier-Stokes relation. Fluctuations in the wake which are important in dynamic cases can be measured by the Root Mean Square (RMS) method (δ_u and δ_v). For a dynamic cycle, mean velocity (u_{mean}) in the wake of the airfoil can be averaged (u_{avg}) based on all phases. By considering the pressure term and fluctuations while $U(h) \neq U_\infty$ and $[-h \quad h]$ is the measurement domain in the y coordinate, the mean drag coefficient was calculated using the following equation [14]:

$$C_{d(mean)} = \frac{2}{c}\int_{-h}^{+h}\left[\frac{u_{avg}(y)}{U_\infty}(1-\frac{u_{avg}(y)}{U_\infty})+\frac{1}{2}(1-\frac{U(h)}{U_\infty})(1-\frac{u_{avg}(y)}{U_\infty})\right.$$
$$\left.-(\frac{\delta_u(y)}{U_\infty})^2+(\frac{\delta_v(y)}{U_\infty})^2-\frac{1}{2}(1-\frac{U(h)^2}{{U_\infty}^2})\right]\mathrm{dy}. \tag{3.3}$$

For validation of the results (Table 3.1), the drag values from Equation (3.3) for the static case, Re=10^5, are compared with drag values calculated based on the two-dimensional momentum and continuity equations by Selig and McGranahan [106]. For the LDA measurement the fluctuation effects in the wake have been taken into account. then, the drag values are slightly higher than those measured by Selig and McGranahan while the the

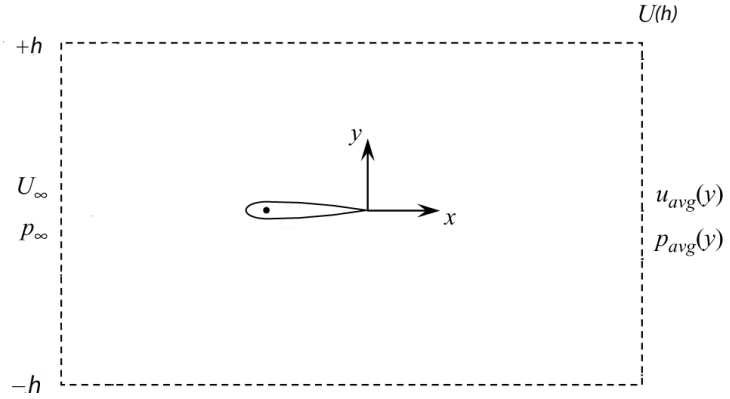

Figure 3.9: Control volume for mean drag coefficient; adapted from Bohl and Koochesfahani [14]

Table 3.1: Static drag coefficients for the S822 airfoil, $Re = 10^5$.

Angle of attack	$-7.19°$	$-2.75°$	$0°$	$3.19°$	$7.89°$
LDA measurement, Equation 3.3	0.032	0.035	0.038	0.045	0.026
Experimental results [106]	0.025	0.028	0.034	0.044	0.022

effects of the fluctuations in the wake were ignored [106]. This is one possible reason for the difference.

3.5 Particle Image Velocimetry (PIV)

As shown in Figure 3.10, the basic principle of standard PIV is based on introducing tracer particles in the fluid flow and then illuminating the particles with a dual-cavity laser. The particle positions are frozen in image pairs captured in a pre-selected time interval, $\triangle t$. Particle displacements between two images in time frame $\triangle t$ provide a velocity field [90].

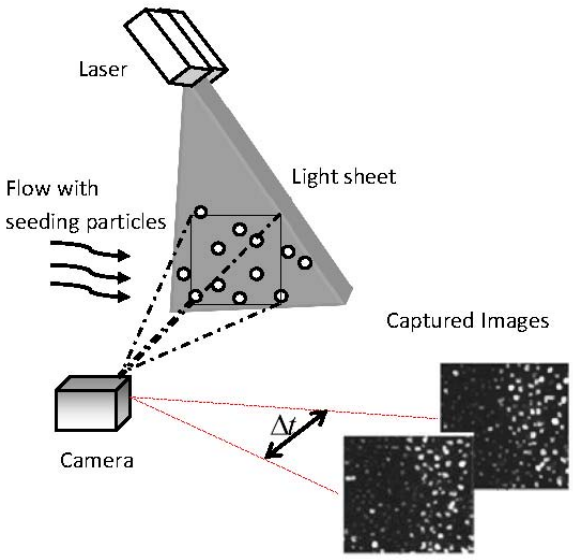

Figure 3.10: Basic principle of PIV

3.5.1 PIV setup

In the current setup, a smoke generator (Le Maitre Special Effects Inc Red Devil) with a remote control seeded a large amount of particles. Smoke fluid (Corona Integrated Technologies Inc 100A) produced large enough particles which lasted long enough for each test, suitable for laser based techniques. It is recommended to fill the wind tunnel with the smoke at the beginning of each test and not add smoke during the test, because adding smoke during the test affects the turbulent intensity of the flow. A Nd:YAG laser (NewWave Research Gemini PIV) illuminated the particles. This dual-cavity laser results in micro second time difference between pulses. Each pulse has a 5 ns duration and a wavelength of 532 nm. Since a full front view of the airfoil is needed, the laser illuminated the test section from the top and bottom walls of the tunnel. Figure 3.11 shows that the green laser beam is divided into two parts with a plate beamsplitter. The vertical beam is rotated 90 degrees with the Edmund optics Laser Line Mirror (Appendix A). It can reflect more than 99 percent of the beam to create even laser beams. Two cylindrical lenses spread the beams into two light sheets, reflected into the test section parallel to the flow field by two laser mirrors. To minimize the errors, the two light sheets from the top and the bottom should cover each other in the mid-span of the test section.

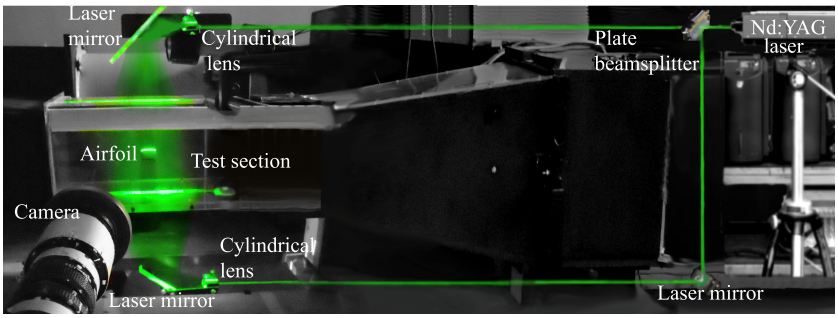

Figure 3.11: PIV light sheet arrangement.

The Dantec dynamics FlowSense EO 4M camera (Appendix A) with a sensor resolution of 2048 $\times$ 2048 pix^2, captured the images. Due to the small field of view, a 60mm f /2.8 Nikkor lens was selected. The fields of view of $\frac{x}{c} = \frac{y}{c} \approx 1.4$ and $\frac{x}{c} = \frac{y}{c} \approx 3$ with an image resolution of 2048 $\times$ 2048 pix^2 were chosen while the time interval between frames was set to $4 \sim 10\mu$s. The scale factor of the images is calculated by taking an image from a custom-made block, Figure 3.12, set in the mid span of the wind tunnel test section where the light sheet was located.

For each phase, 500 image pairs were acquired. The images were collected in several sequential experimental runs since generated vapor on the window of the wind tunnel increased the level of the noise after 50 image pairs. The 80N77 Timer Box (Appendix A) synchronized the laser and camera when it is triggered with a TTL signal from the motor controller. For the highest frequency of the oscillation, the maximum error of triggering is around 0.2^o. It should be noted that since the airfoil is small, one camera was sufficient for capturing the whole field of view and there was no need for an extra laser. Thus, the errors associated with multiple cameras and lasers are removed. Because of the small field of view, the spatial resolution has also been increased. Figure 3.13a shows an image taken for the dynamic case. The particles are visible for both the pressure and suction surfaces.

3.5.2 PIV data processing

For calculating the velocity field, the PIV images were processed with the PIV adaptive method of the Dantec DynamicStudio software and an in-house hierarchical PIV iteration code. The in-house PIV post processing code was written to understand the basics of the PIV post processing algorithms. The accuracy of the in-house code was evaluated with

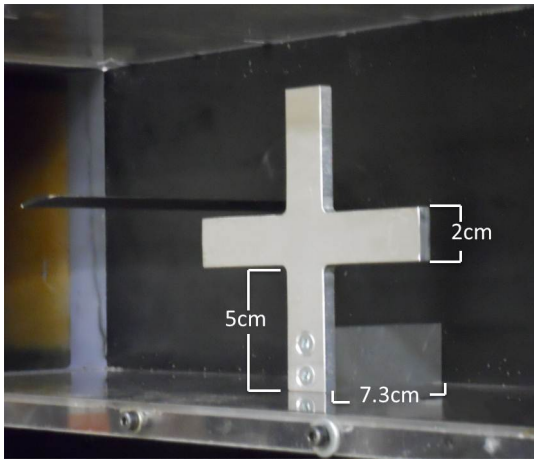

Figure 3.12: Custom-made block for calculating the scale factor of the PIV images

the generated synthetic images, Section 3.5.5, but the experimental PIV images have been post processed with the PIV adaptive method. For the PIV pressure and load calculations, the in-house pressure and load calculation codes were applied which will be discussed in the following sections.

Since the velocity of a fluid is a function of two fundamental dimensions, length and time, by determining the displacement of the particles between two images in the time step, the velocity field is achieved. Image processing calculates the movement of the particle clusters through each area of interest or interrogation area (IA), where one velocity vector is located. Basic PIV data processing algorithms calculate just straight-line displacements of fluid parcels; then, they lose the curvature information of displacements; therefore, these methodologies suffer inherently from a lack of accuracy in the analysis of flows with large velocity gradients. Advanced PIV methods were created to enhance the quantity of detection of particle motion in complex flows. Although these techniques are computationally expensive, they are appealing because of enriching the accuracy of the results and expanding the spatial resolution and dynamic range of the velocity.

The in-house hierarchical PIV iteration code [39, 38] is a combination of predictor corrector and multi-grid interrogation, so-called super resolution FFT. This method is divided into two parts: Dynamic IA location [131, 133] and halving IA size [102]. Here, the hierarchical PIV iteration code was employed for processing the synthetic images. Three level steps with the final refined 32x32 pixels for each IA and a 50% overlap in the interrogation areas were chosen. The number of the particles for each IA was fixed by the synthetic image generation algorithm. For this case, 8 particles for each IA were chosen.

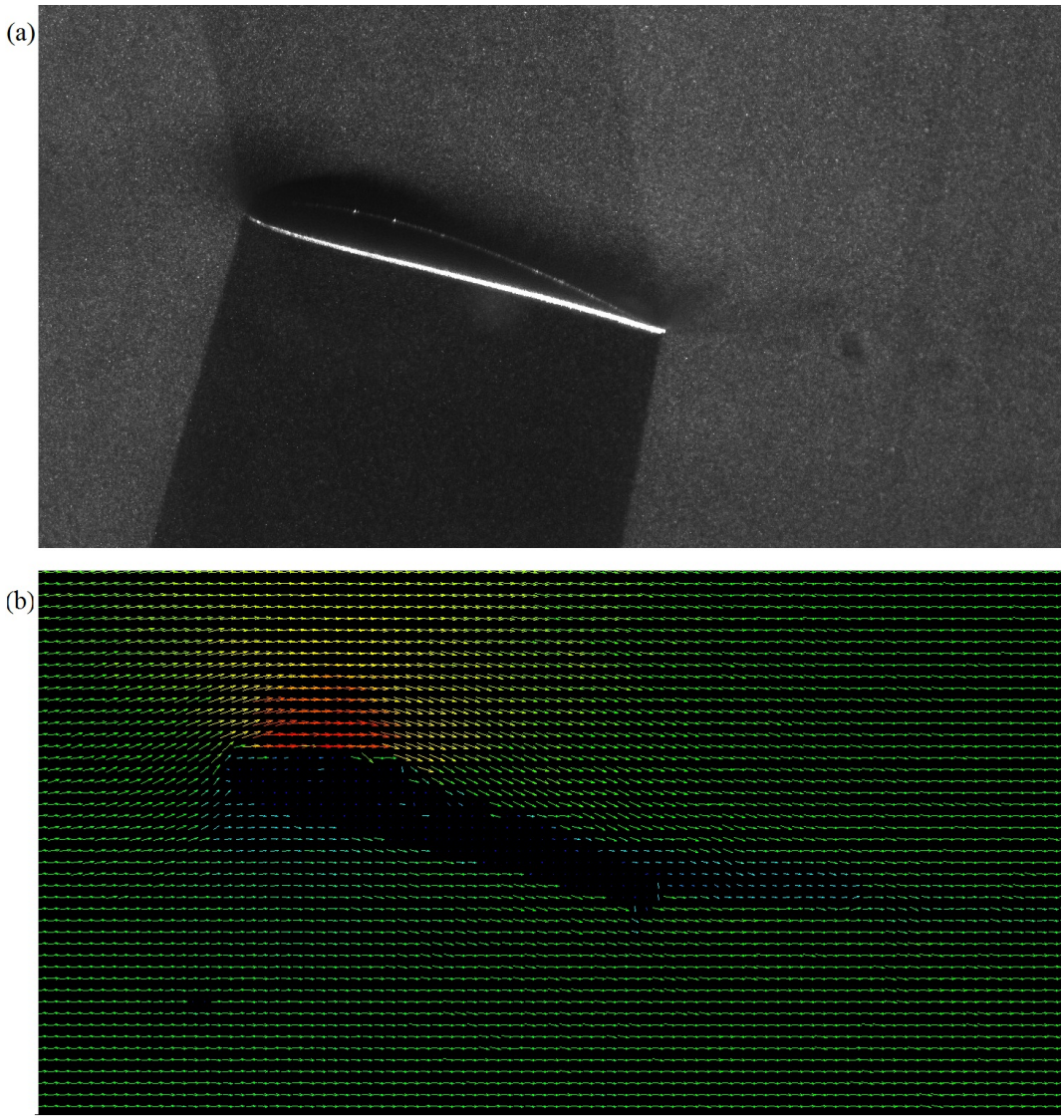

Figure 3.13: PIV results from illuminating the top and the bottom surfaces of an oscillating airfoil; a) an instantaneous PIV image; b) velocity map of one PIV image pair.

If the number of the particles is increased, smaller IA can be applied. Finally the velocity fields were post processed by filtering, interpolation, smoothing and averaging to decrease the erroneous velocity vectors particularly ones located close to the airfoil surface.

The PIV adaptive method of the Dantec DynamicStudio software can change the size and the shape of each IA based on the local flow gradients and particle densities iteratively where the center position distance from an IA to its neighbor was set to 16 pix. This algorithm can work very well for a small field of view similar to the current study. Each resultant velocity vector was validated by the universal outlier detection local neighborhood with size 3 $\times$ 3. Figure 3.13b shows a sample velocity vector map. There are just a few outliers without phase averaging proving the low noise level of the images.

The precision PIV errors are listed in Appendix C which result from uncertainty of velocity fluctuations. For other sources of errors, Particle Image Velocimetry books [3, 90] are suggested.

3.5.3 Integral forces calculation

Based on linear momentum, the aerodynamic loads on an object, surrounded by a control volume (CV) of unit depth fixed in space and bounded by control surface (CS), (Figure 3.14), are determined indirectly by integrating flow variables inside the control volume:

$$\vec{F} = -\int\int\int_V \frac{d}{dt}(\rho\vec{U})dV - \int\int_s \rho\vec{U}(\vec{U}\cdot\hat{n})dS - \int\int_s P\hat{n}dS + \int\int_s (\bar{\bar{\tau}}\cdot\hat{n})dS \tag{3.4}$$

where $\hat{n}$ is the unit vector, $\vec{U}$ the velocity vector, P the flow pressure and $\bar{\bar{\tau}}$ the viscous stress tensor. In the pitch oscillating case, loads are phase averaged due to periodic motion and the unsteady term at low reduced frequency is eliminated:

$$\bar{\vec{F}} = -\rho\int\int_s \bar{\vec{U}}(\bar{\vec{U}}\cdot\hat{n})dS - \int\int_s \bar{P}\hat{n}dS + \int\int_s \bar{\bar{\tau}}\cdot\hat{n}dS \tag{3.5}$$

where the flow is considered as incompressible flow. The overbars show phase averaged values. Assumptions of a 2D domain transfers the integration of the control surface to a line or contour integration. Choosing a counter-clockwise direction for the line integration,

substituting the phase averaged values and ignoring the overbars give the total force ($\vec{F}$):

$$\begin{bmatrix} d \\ l \end{bmatrix} = \rho \oint \begin{bmatrix} -uu\,dy + uv\,dx \\ -uv\,dy + vv\,dx \end{bmatrix} - \oint \begin{bmatrix} P\,dy \\ -P\,dx \end{bmatrix} + \mu \oint \begin{bmatrix} 2\frac{\partial u}{\partial x}\,dy - (\frac{\partial u}{\partial y} + \frac{\partial v}{\partial x})\,dx \\ (\frac{\partial u}{\partial y} + \frac{\partial v}{\partial x})\,dy - 2\frac{\partial v}{\partial y}\,dx \end{bmatrix} + \rho \oint \begin{bmatrix} -u'u'\,dy + u'v'\,dx \\ -u'v'\,dy + v'v'\,dx \end{bmatrix} \tag{3.6}$$

where $\vec{F} = \begin{bmatrix} d \\ l \end{bmatrix}$ represents the drag (d) and lift (l) forces.

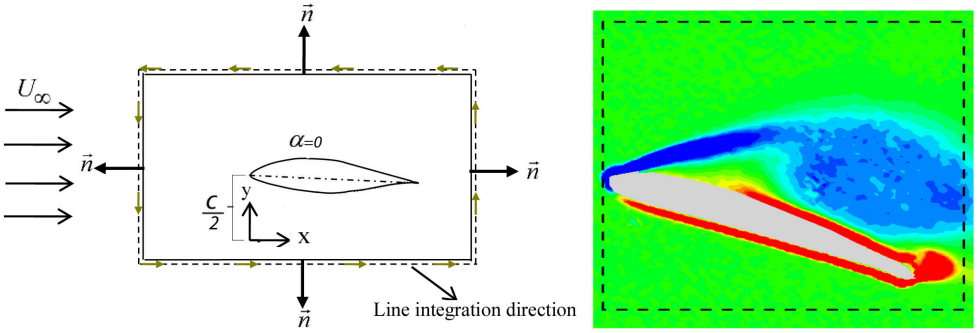

Figure 3.14: Sketch of the 2D control volume and control surface definitions for determining integral aerodynamic forces; right: control volume boundaries for a pitching airfoil during post stall superimposed with the vorticity field.

3.5.4 Pressure determination

Integrating the phase averaged Navier-Stokes equations gives the mean pressure acting on the control surface. The tensor form of the phase-averaged pressure is

$$-\frac{\partial \bar{P}}{\partial x_i} = \rho \bar{U}_j \frac{\partial \bar{U}_i}{\partial x_j} + \rho \frac{\partial \overline{U_i' U_j'}}{\partial x_j} - \mu \frac{\partial^2 \bar{U}_i}{\partial x_j \partial x_j}. \tag{3.7}$$

To integrate gradient information, a 2D surface is generated and then central difference is used in the whole body except along the surface boundaries where forward/backward difference is applied. Figure 3.15 shows an example of the calculated pressure coefficient

(Equation 3.8) field around the dynamic SD7037 airfoil while the low pressure waves in the LEV and TEV are perfectly captured. The pressure coefficient is calculated based on

$$C_P = \frac{P - P_\infty}{\frac{1}{2}\rho U_\infty^2}, \tag{3.8}$$

where P_∞ is the freestream static pressure.

To avoid error propagation associated with integration methods for calculating aerodynamic loads, pressure was calculated through the Bernoulli relation for the upstream and the lower sides of the control surface. The Navier-Stokes equations are integrated numerically by a forward-differencing method in the x-axis direction for the suction side of the control surface. In the wake the downstream side is integrated by a second order central-differencing (standard five-point) scheme while the first and last nodes were known.

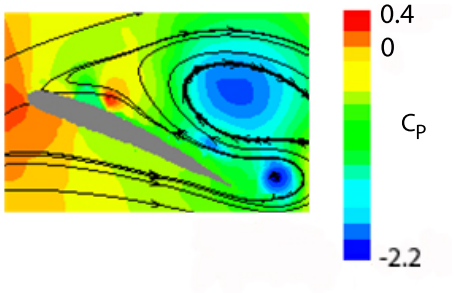

Figure 3.15: PIV pressure field around the SD7037 airfoil at $\alpha = 20.5^o \uparrow$ ($\alpha = 11^o + 11^o sin(2\pi ft)$, $Re = 4 \times 10^4$ and $k = 0.08$); for the details of the case study see Chapter 5.

3.5.5 Synthetic images

For evaluating and validating the custom in-house velocity code and calculated aerodynamic loads, standard or synthetic images generated by an in-house code were used. The synthetic image generation code was developed by Young [142] based on Monte Carlo simulations with basic velocity functions such as a step function. Since there is no open source standard images with an object inside, for this study this code was updated to generate images with an object. e.g. an airfoil. Several (N) resultant velocity fields within the time interval Δt/N from a CFD simulation were interpolated to the uniform Cartesian grid. The rectangular grids were used as input for the particle displacement between synthetic image pairs at N steps. It should be noted that interpolating the CFD velocity field inserts an error by its own nature. Figure 3.16 shows a sample of a synthetic image.

Based on the synthetic images, the accuracy of the velocity flow fields from the in-house code was around 1.2%. For calculating the aerodynamic loads, the information from the CFD velocity field was imported to the load calculation code to minimize the velocity error. The CFD velocity fields were post processed with the PIV control volume approach to get the aerodynamic loads. The aerodynamic loads from the control volume approach were compared with the CFD loads and showed lift coefficient errors between 0.9% and 2% and drag coefficient errors less than 4.5%.

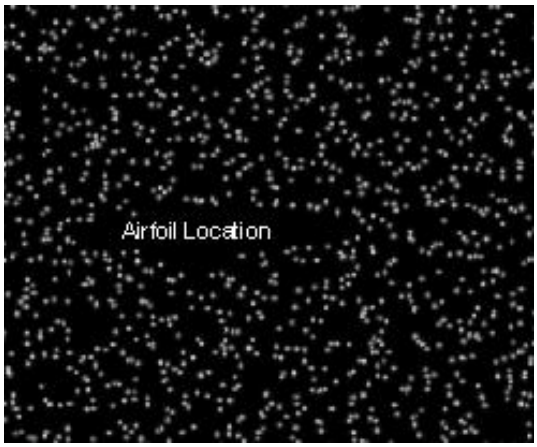

Figure 3.16: Generated synthetic image around an airfoil

3.5.6 Vorticity, circulation and vortex trajectory

The curl of the phase-averaged 2D velocity field

$$\omega_z = \frac{\partial u}{\partial y} - \frac{\partial v}{\partial x} \tag{3.9}$$

defines the vorticity field.

Based on Stoke's theorem, the targeted vortex circulation, Γ, inside a rectangular area A can be calculated,

$$\Gamma = \int\int_A \omega_z dA, \tag{3.10}$$

where, the clock-wise vortex ($\omega_z < 0$) and counter-clockwise vortex ($\omega_z > 0$) are separated and considered for LEV circulation (Γ_{LEV}) and TEV circulation (Γ_{TEV}), respectively

[35, 85]. The center of each individual vortex with the maximum vorticity magnitude was considered as the vortex core. As the distance from the core of the vortex increases, the magnitude of the vorticity decreases and it does not change the circulation values. In Equation 3.10, for each individual vortex covered by A, the size of A was increased manually and gradually until there was no change in the calculated circulation. This indicated that the determined circulation was converged and the optimum size of A was reached. A vortex core which has the maximum circulation can be tracked manually to find the location of that vortex.

Chapter 4

Numerical setup

The Computational Fluid Dynamic (CFD) flow solver packages ANSYS Fluent version 13 [1], for the S809 and SD7037 airfoils, and version 12.1, for the NACA0012 and S822 airfoils, were employed to model the two-dimensional flow field over an oscillating airfoil under a constant freestream velocity as well as an unsteady freestream velocity. In this chapter, turbulence models for dynamic stall phenomena are discussed and compared. Details of the mesh generation and solver setup are presented. The results are validated with wind-tunnel measurements for static and dynamic cases.

4.1 Unsteady Reynolds-Averaged Navier Stokes (URANS)

The unsteady flow field is simulated by solving Unsteady Reynolds Averaged Navier-Stokes (URANS) equations (Equations 4.1 and 4.2) iteratively. In Fluent, URANS equations are solved based on the finite volume method. The following equations are the differential form of the two-dimensional, incompressible time averaged Navier Stokes while their components are replaced by their decomposed form of mean and fluctuation:

$$\frac{\partial u_i}{\partial x_i} = 0, \tag{4.1}$$

$$\frac{\partial u_i}{\partial t} + \frac{\partial \left(u_i u_j + \overline{u_i' u_j'} \right)}{\partial x_j} = \frac{\partial}{\partial x_j} \left[\frac{\mu}{\rho} \left(\frac{\partial u_j}{\partial x_i} + \frac{\partial u_i}{\partial x_j} \right) \right] - \frac{1}{\rho} \frac{\partial p}{\partial x_i}, \tag{4.2}$$

where the overbars for the mean quantities are not shown. For the numerical simulation, modeling the Reynolds stress $\overline{u_i' u_j'}$ term is challenging and it will be discussed in the following section.

4.1.1 SST $k-\omega$ turbulence model

In URANS equations, the Reynolds stresses $\overline{u_i' u_j'}$ can be modeled according to the Boussinesq hypothesis,

$$-\overline{u_i' u_j'} = \frac{\mu_t}{\rho}\left(\frac{\partial u_i}{\partial x_j} + \frac{\partial u_j}{\partial x_i}\right) - \frac{2}{3}k\delta_{ij}, \tag{4.3}$$

where μ_t is the turbulent viscosity and k is the kinetic energy. For turbulence closure, the Shear-Stress Transport, SST $k-\omega$, model [71] is capable of capturing the flow structures of dynamic airfoils associated with leading edge vortex formations for a wide range of the Reynolds numbers [4, 71, 75, 77, 94, 129, 143]. This model is a combination of the $k-\omega$ model of Wilcox [135], for the near-wall region, and the $k-\varepsilon$ model of Jones and Launder [48], for the far field region. The kinetic energy, k, and the specific dissipation rate, ω, transport equations [1] are

$$\frac{\partial}{\partial t}(\rho k) + \frac{\partial}{\partial x_i}(\rho k u_i) = \frac{\partial}{\partial x_j}\left(\Gamma_k \frac{\partial k}{\partial x_j}\right) + \widetilde{G_k} - Y_k \tag{4.4}$$

$$\frac{\partial}{\partial t}(\rho \omega) + \frac{\partial}{\partial x_i}(\rho \omega u_i) = \frac{\partial}{\partial x_j}\left(\Gamma_\omega \frac{\partial w}{\partial x_j}\right) + G_\omega - Y_\omega + D_\omega. \tag{4.5}$$

$\widetilde{G_k}$ and G_ω are generation terms due to mean velocity gradients, Y_k and Y_ω are the dissipation terms, D_ω is the additional cross diffusion term between the $k-\varepsilon$ model and $k-\omega$ formulation, and Γ_k and Γ_ω are effective diffusivity

$$\Gamma_k = \mu + \frac{\mu_t}{\sigma_k} \quad and \quad \Gamma_\omega = \mu + \frac{\mu_t}{\sigma_\omega}, \tag{4.6}$$

where σ_ω and σ_k are modeled with the blending function F_1. The turbulence viscosity, μ_t, is modeled by blending function F_2

$$\mu_t = \frac{\rho k}{\omega}\frac{1}{max[\frac{1}{\alpha^*}, \frac{SF_2}{a_1 \omega}]}. \tag{4.7}$$

Moreover according to Bradshaw's hypothesis, the turbulent shear stress should be proportional to k in the boundary layer which agrees with Equation 4.7 [71]. For more details of this method, the canonical manuscript of Menter [71] is suggested.

Low-Reynolds number correction

Although the SST $k-\omega$ model is for fully turbulent flows, it accommodates the transitional regime with a low-Reynolds number correction. With this correction, the turbulent viscosity (μ_t) is damped by the coefficient α^* [1, 135]

$$\alpha^* = \frac{0.024 + \frac{Re_t}{6}}{1 + \frac{Re_t}{6}}, \tag{4.8}$$

where

$$Re_t = \frac{\rho k}{\mu \omega}, \tag{4.9}$$

and here k and ω are related to the $k-\omega$ model only.

Transition SST model

In this model, the SST $k-\omega$ turbulence model is integrated with a correlation-based transition model of Menter et al. [72, 73] using local variables. The two SST $k-\omega$ equations are coupled to two transport equations: the intermittency, γ, and the transition momentum-thickness Reynolds number, $\overline{Re_{\theta t}}$. Utilizing the advantages of the SST $k-\omega$ model for predicting massively separated flow, the transition SST model (or the $\gamma - \overline{Re_{\theta t}}$ model) can predict the laminar-turbulent boundary layer transition more accurately based on local variables. The intermittency transport equation (Equation 4.10) causes transition onset, considering small instabilities in the laminar flow, based on local variables.

$$\rho[\frac{\partial(\gamma)}{\partial t} + \frac{\partial(U_j \gamma)}{\partial x_j}] = P_{\gamma 1} - E_{\gamma 1} + P_{\gamma 2} - E_{\gamma 2} + \frac{\partial}{\partial x_j}\left[\left(\mu + \frac{\mu_t}{\sigma_\gamma}\right)\frac{\partial \gamma}{\partial x_j}\right], \tag{4.10}$$

where $P_{\gamma 1}$ and $E_{\gamma 1}$ are transition sources and $P_{\gamma 2}$ and $E_{\gamma 2}$ presents the destruction / relaminarization sources.

The nonlocal information of the turbulence intensity, influenced by k decay and freestream velocity variations, and freestream pressure gradient are conveyed by the transitional momentum thickness Reynolds number transport equation:

$$\rho[\frac{\partial\left(\widetilde{Re_{\theta t}}\right)}{\partial t} + \frac{\partial\left(U_j \widetilde{Re_{\theta t}}\right)}{\partial x_j}] = P_{\theta t} + \frac{\partial}{\partial x_i}\left[\sigma_{\theta t}(\mu + \mu_t)\frac{\partial \widetilde{Re_{\theta t}}}{\partial x_j}\right], \tag{4.11}$$

where $P_{\theta t}$ is the source term and $\sigma_{\theta t}$ is the model constant [1]. Further details regarding this model can be found in the work of Menter et al. [73].

4.2 Mesh

A C-grid layout, Figure 4.1, has been generated by ICEM CFD [1], for the S809, SD7037, NACA0012 and S822 airfoils. For the sake of outer boundary effect elimination all the computational domain boundaries were placed about $20c$ from the airfoil surface [136, 137, 143, 35, 34]. For all the airfoils, there are 500 nodes around the airfoil. Close up views of the meshes around the airfoils are shown in Figure 4.2. The non-dimensional wall distance is kept less than one ($y^+ < 1$). Increasing the grid resolution was numerically very expensive especially for a dynamic case. To determine the independence of the results from the grid resolution, the number of cells in the grid was increased to create finer meshes. In some cases the number of the cells were doubled, but testing higher resolution grids gave similar results indicating the independency of the results to the grid size where the criteria for grid independence was based on the aerodynamic loads. The final grid sizes are provided in Table 4.1.

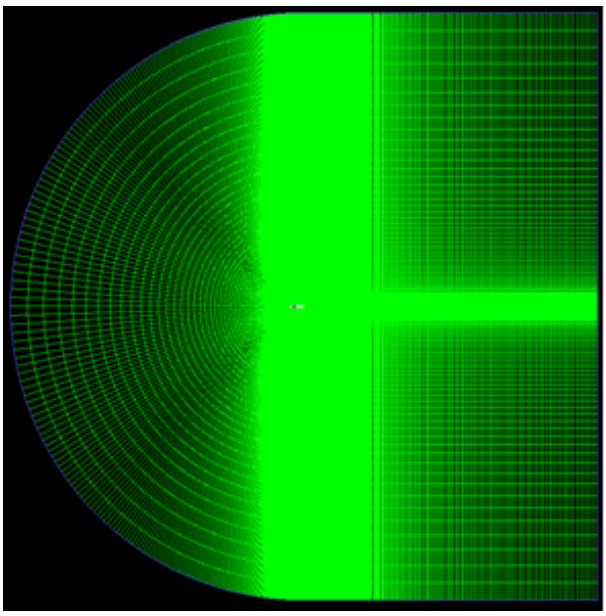

Figure 4.1: Computational domain covered with a C-type mesh

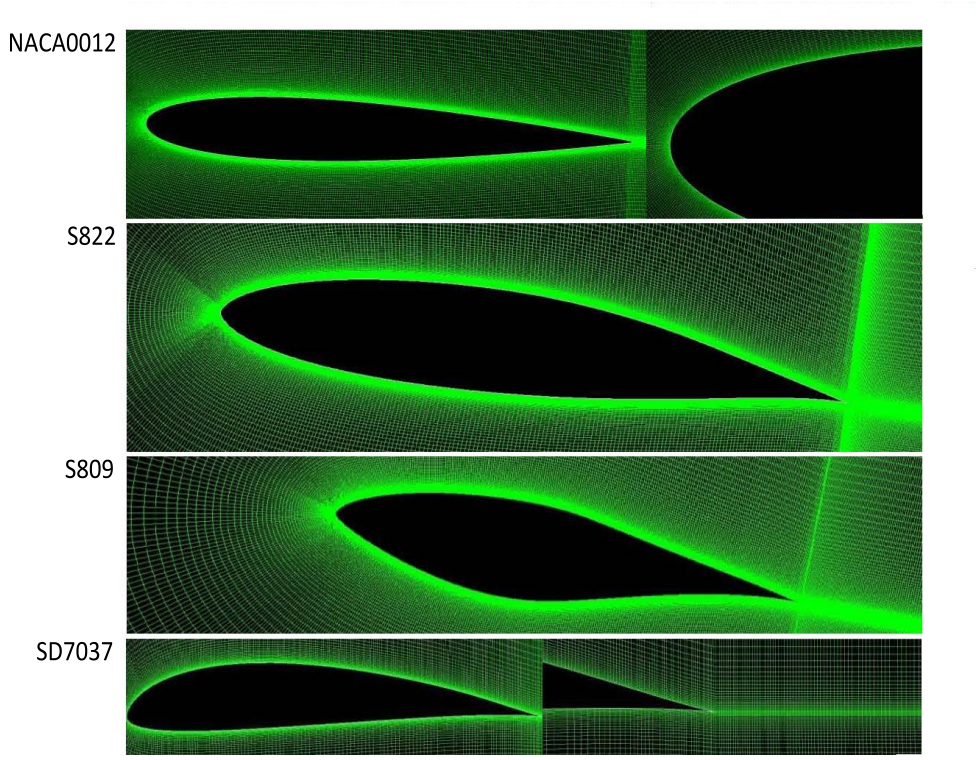

Figure 4.2: Close up view of the C-type mesh around airfoils.

4.3 Solver setup

The airfoil and the whole computational domain were oscillating together according to equation 2.2 like a rigid body about the 1/4 chord location by a compiled user-defined function, Figure 4.3. Besides the dynamic mesh, the velocity of the freestream can oscillate horizontally described by equation 2.5 via a user-defined function to create an unsteady airstream. At different angles, the straight sides of the domain can be either inlet or outlet. Since the boundary conditions were changing during pitching, inlet/outlet velocity was used for all external boundary conditions. The inlet/outlet velocity can be used if the overall continuity of the domain is fulfilled [1] and the boundaries are far from the object. In this study, the inlet and outlet areas normal to the inflow velocity were always equal and the boundaries were located far enough from the object, $20c$. For the airfoil surface, the no-slip condition was set. Since the flow is incompressible, the pressure based Navier Stokes solution algorithm was used. For the pressure-velocity coupling scheme, the SIMPLEC and PISO coupling algorithms for steady and unsteady RANS simulations were chosen. The second order upwind method for spatial discretization gave satisfactory results. The convergence criteria for the residuals were $\mathcal{O}(5 \times 10^{-5})$ in magnitude for all cases. As another criterion for judging the convergence, load values were monitored manually for the first few steps. After the loads and the other residuals were converged, a small time step size was introduced for the rest of the simulation to satisfy that the rest of the steps were converged. Moreover, to determine the optimum time step, a few simulations were run with shorter time steps and the final resultant load loops were compared. When the load loops were temporally independent or were not changed by decreasing the time step, the optimum time step was obtained. The time step size usually is presented based on the characteristic time of the airfoil (τ)

$$dt = \tau(c/U_\infty). \tag{4.12}$$

For each case study, the optimum τ values are reported in Table 4.1. Because a dynamic mesh was used, the first-order temporal discretization was fixed for the transient formulation by the software. After the first pitching cycle, shown in Figure 4.4, the aerodynamic load loops become periodic even for the unsteady freestream velocity cases.

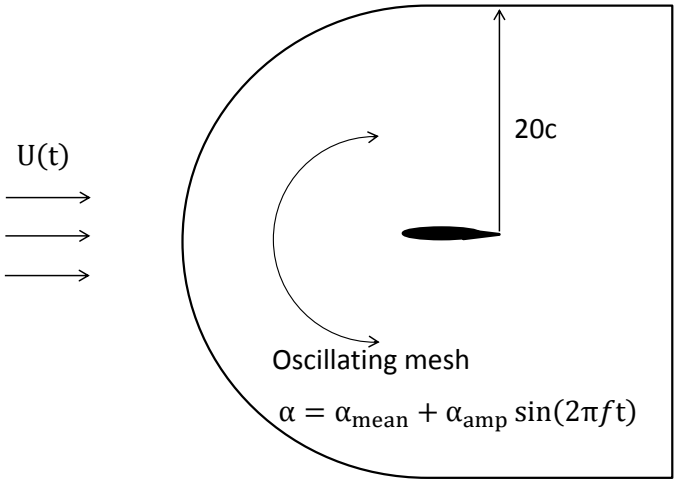

Figure 4.3: Dynamic mesh facing a horizontally steady/unsteady freestream velocity

Table 4.1: Numerical setup information

Airfoil	Size of the mesh (cells)	Method	τ (equation 4.12)
NACA0012	2×10^5	SST $k-\omega$ (low-Re correction)	10^{-2}
S822	2×10^5	Transition SST	10^{-2}
S809	2.5×10^5	Transition SST	10^{-3}
SD7037	2×10^5	Transition SST	10^{-2}

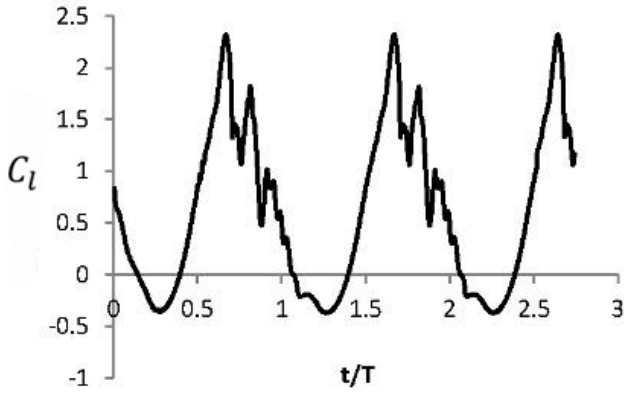

Figure 4.4: History of the lift coefficient for the pitch oscillating NACA0012 airfoil

4.4 Numerical simulation validation

4.4.1 Static case

For the static case, the high angles of attack around the static stall angle were targeted because most discrepancies between numerical and experimental results usually occur at these angles. The numerical results are compared with published experimental results. In Figure 4.5 for the NACA0012 airfoil at $Re = 1.35 \times 10^5$, the numerical results of the $k-\omega$, the SST $k-\omega$ with low-Reynolds number correction and the transition SST models are compared with experimental results of Lee and Gerontakos [57]. More information regarding the experimental study is provided in Chapter 7. For the S809 airfoil at $Re = 10^6$, Figure 4.5, the numerical results with the SST $k-\omega$ model with low-Reynolds number correction and the transition SST models are compared with the experimental results of Somer [113], measured at the Delft low speed, low-turbulence wind tunnel. Moreover, for the fully turbulent simulation, the results of Johansen [46] using the SST $k-\omega$ model are shown. For both cases, the superiority of the transitional prediction methods to the fully turbulent models is obvious. The SST $k-\omega$ with low-Reynolds number correction and the transition SST models agree well with the experimental results, but after stall, the transition SST results are more accurate for predicting separated flow fields.

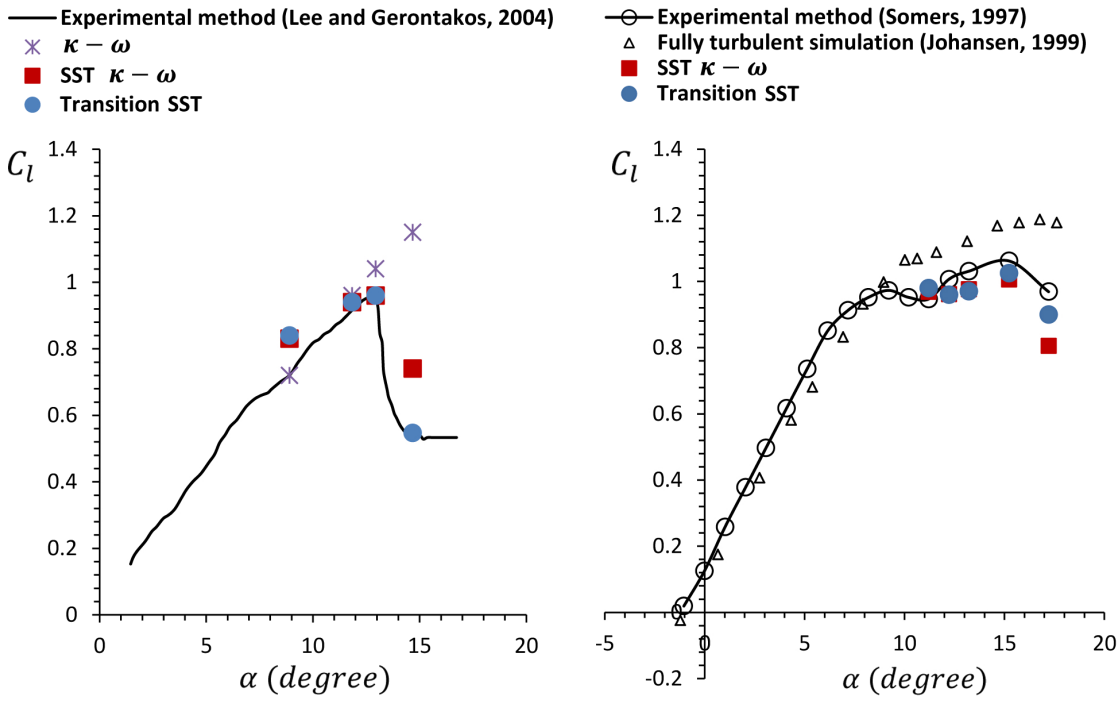

Figure 4.5: Static lift coefficients from experimental and numerical methods; Left: NACA0012 airfoil, $Re = 1.35 \times 10^5$; Right: S809 airfoil, $Re = 10^6$.

4.4.2 Dynamic case

SST $k-\omega$ model

To confirm the accuracy of the numerical simulation, the instantaneous loop loads for the NACA0012 airfoil ($Re = 1.35 \times 10^5$) are compared with the existing experimental results of Lee and Gerontakos [57] for sinusoidal pitch oscillation with a steady freestream in Figure 4.6. More information about this case study is provided in Chapter 7. This case was also numerically modeled by Wang et al.[129]. They applied the same turbulence model, the SST $k-\omega$ model with low-Reynolds correction, but the aerodynamic loads showed an unstable behavior particularly during upstroke as shown in Figure 4.7. It was found in this study that one of the key parameters to give a more stable simulation is the cell skew factor. For the current mesh, the cell equi-angle skew is almost zero except for two small areas close to the leading and trailing edges with the maximum value of 0.1. If the value of this factor increases, the results become more unstable. Although the cell skew factor is always important for a quality mesh [1], sometimes a value much higher can give good results for different cases, but for dynamic stall phenomena, this factor should be as small as possible. Wang et al. [130] in another study improved the results which are shown and compared with the current result also in Figure 4.7. At pitch down motion, the current lift loop slightly oscillates around the experimental lift curve and it is closer to the experimental one than that of Wang et al. [130] which covers the upstroke curve instead of the downstroke one. These small oscillations during downstroke are a result of reattachment and relaminarization and are not related to the mesh quality.

Besides integral lift and drag forces, the wake streamwise velocity profiles from numerical and experimental methods are compared in Figure 4.8. The numerical model predicts a narrower wake and smaller wake deficit. At $\alpha = 15^\circ \uparrow$ (upstroke), the flow is attached with a narrow wake. In this region there is good agreement between the two methods. At higher angles of attack with separated flow, the wake deficit and the wake thickness increase. The wake profile at $\alpha = 25^\circ$ demonstrates massive separation after stall. The overall trends of the curves for $y/c < -0.3$ differ. There will be a discussion later that the numerical simulation advances the dynamic stall point. Thus, the vortical structures as well as wake velocity profiles during post stall cannot be exactly the same for both methods.

Transition SST model

The chosen pitch oscillating parameters for the S809 airfoil ($Re = 10^6$) provide the opportunity to validate the simulated predictions with the experimental results of Ramsay

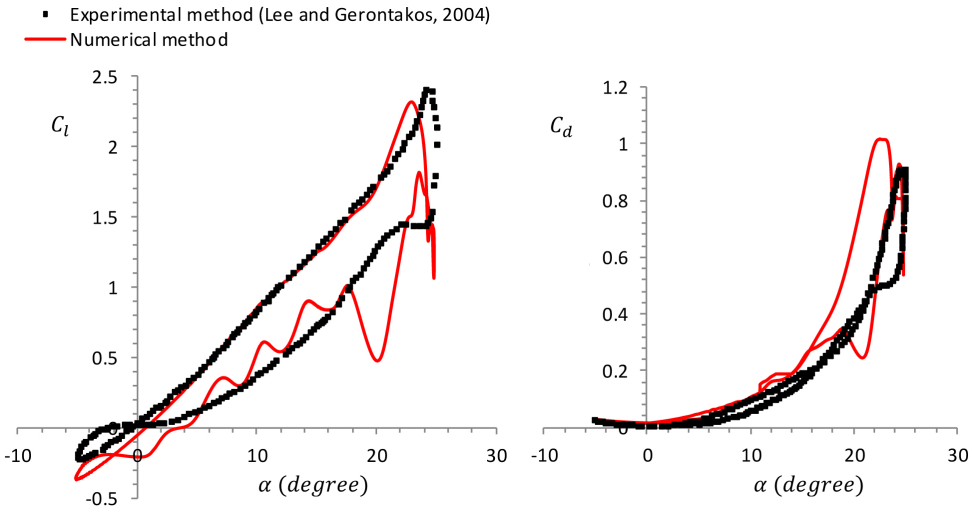

Figure 4.6: Comparison of dynamic load loops from the current numerical simulation and experimental method [57] for the NACA0012 airfoil; Legend: ■ experimental data [57], __ simulation.

et al. [93] with the same parameter values. The information regarding this case study is reported in Chapter 8. In Figure 4.9, the lift coefficient and the drag coefficient from numerical and experimental methods are compared. Although the aerodynamic loads are slightly over predicted at the dynamic stall angle, good overall agreement between the results of the two methods indicates the ability of this numerical method to predict such a complicated flow structure. The advantage of the transition SST model for capturing the correct location of dynamic stall, which is usually challenging, is also visible. For complicated flow fields associated with dynamic stall, during downstroke the boundary layer is significantly separated and interaction of the separated vortices expands the wake. Thus, numerical prediction of the aerodynamic loads during downstroke is inherently challenging. Figure 4.9 demonstrates that at downstroke the two curves from experimental and numerical methods are very close.

4.5 Summary

The agreement between the numerical and experimental methods is an indication of the reliability of the current numerical setup which is a combination of many chosen parameters such as a qualified mesh, an optimum time step and a proper turbulence model. More

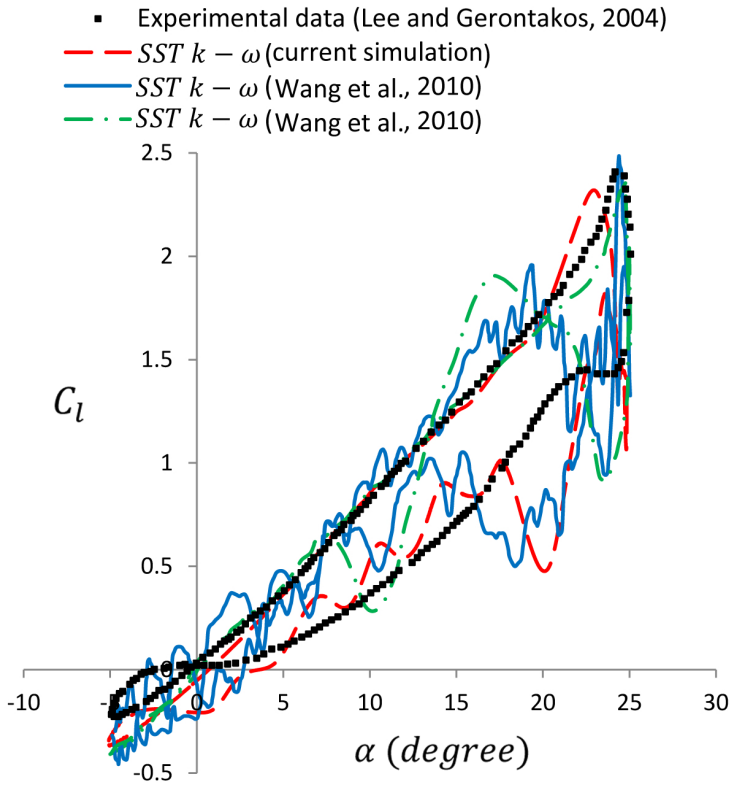

Figure 4.7: Dynamic lift loops for the NACA0012 airfoil; Legend: ■ experimental data [57], _ _ current simulation, __ numerical results of Wang et al. [129], _ . _ numerical results of Wang et al. [130].

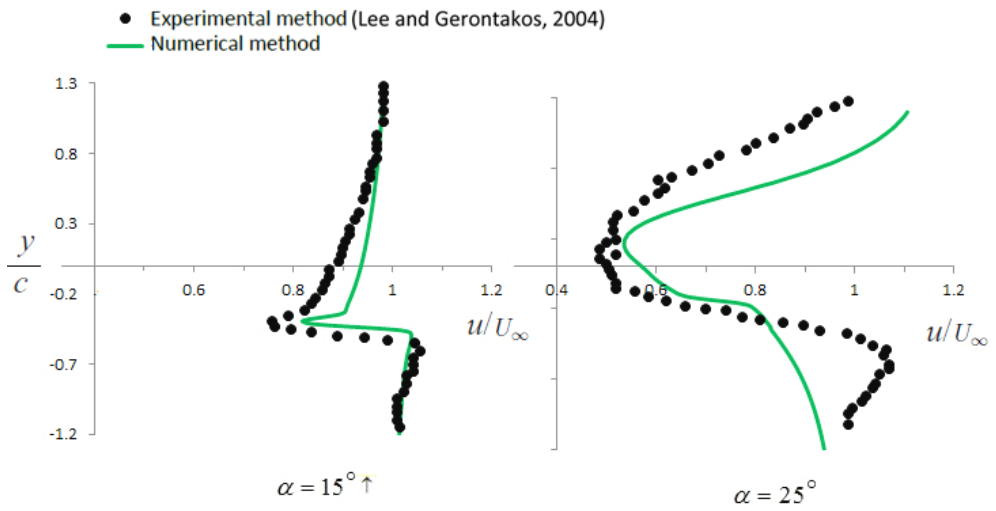

Figure 4.8: Wake streamwise velocity profiles at one chord from the trailing edge of the NACA0012 airfoil.

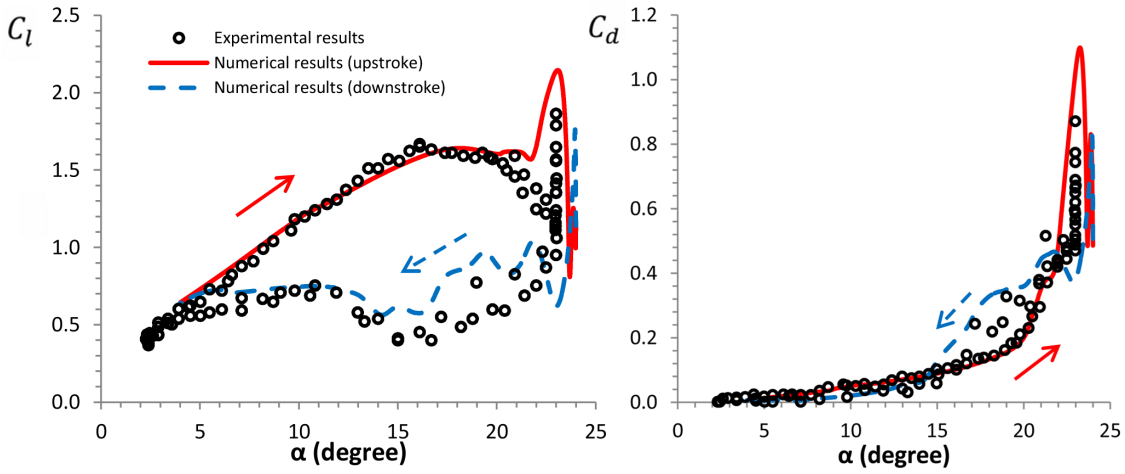

Figure 4.9: Instantaneous numerical aerodynamic loads and experimental measurements [93] for the pitch oscillating S809 airfoil under steady incident velocity.

validations for each individual case study will be in their corresponding chapters. The SST $k-\omega$ with low-Reynolds number correction and the transition SST models could predict static stall and deep dynamic stall which are challenging numerically. The transition SST model was slightly superior than the SST $k-\omega$ for predicting the exact location of the dynamic stall (maximum lift value) and gave more robust results during pitch down motion. It should be noted that the SST $k-\omega$ model is capable of capturing the flow structures of dynamic airfoils associated with leading edge vortex formations for a wide range of Reynolds numbers with an acceptable accuracy [4, 77, 94]. The disadvantage of the transition SST model is that it has two more equations causing longer simulation time. In this study, simulations were run over 8 CPUs, for the SST $k-\omega$ turbulence model, and over 16 CPUs, for the transition SST model, in parallel using the facilities of the Shared Hierarchical Academic Research Computing Network (SHARCNET) and Compute/Calcul Canada. The transition SST method was used for all the cases except for the NACA0012 airfoil because the first series of simulations were done for the NACA0012 airfoil with the maximum 8 parallel CPUs. After SHARCNET increased the number of ANSYS licenses, for the rest of the airfoils, the transition SST model was used with 16 parallel CPUs.

Chapter 5

Load determination and vortex study (SD7037 airfoil, $Re = 4 \times 10^4$)

An examination into the dynamic stall phenomena of the oscillating SD7037 airfoil has been performed experimentally and numerically. PIV post processing has been done to calculate aerodynamic loads and pressure fields which are challenging for the dynamic airfoils. For a reduced frequency range of $0.05 \leq k \leq 0.12$, the behavior of the laminar separation bubble and dynamic stall vortices have been studied in detail.

5.1 Case studies and approaches

Sinusoidal pitch oscillation, Equation 2.2, of the SD7037 airfoil is considered in this chapter while $\alpha_{mean} = 11^o$ and $\alpha_{amp} = 11^o$. The effects of the reduced frequency (k), Equation 2.3, are investigated with $k = 0.05$, 0.08 and 0.12. For all cases, the Reynolds number of 4×10^4 was fixed. The Cartesian coordinate system with its origin is shown in Figure 3.14.

The experimental part of the current study employed particle image velocimetry (PIV) while a computational fluid dynamics (CFD) simulation was performed for the same flow field with the transition SST method.

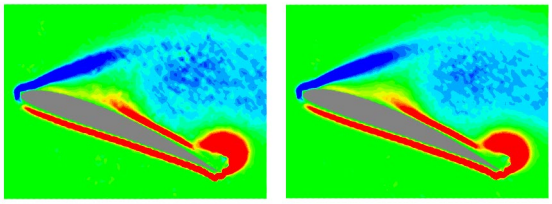

Figure 5.1: Effects of the number of image pairs on visualization; vorticity field of $k = 0.08$ and $\alpha = 20^o \uparrow$.

5.2 PIV-based load determination

5.2.1 Uncertainty analysis

Besides statistical uncertainty analysis, given in Appendix C, the uncertainty of the PIV-load values has been considered by using the relevant sources such as the number of samples, the location of control-volume surfaces and spatial resolution.

Number of samples

Increasing the number of samples or image pairs (N) decreases the statistical errors, given in Appendix C. For visualization purposes, the effects of the number of samples on the resultant vorticity field are presented in Figure 5.1 for the dynamic case of $k = 0.08$ at $\alpha = 20^o \uparrow$ with highly separated flow after dynamic stall. The vortical structure demonstrates no significant difference by increasing the number of image pairs twenty times and the details of the vortical structure are captured well. On the contrary, the calculated loads in Table 5.1 indicate the load sensitivity when the number of images is changing from 250 to 500. The effects of the number of image pairs on load calculation is more significant for dynamic cases especially for the cases with dominant vortices. For N$>$ 500, it does not change the estimated loads significantly. It can be concluded that for visualization purposes, very low N values (50 images with high quality raw images) give satisfactory results and all the main flow structures are captured but for load calculation purposes, after 500 samples loads remain insensitive.

Table 5.1: Load determination sensitivity to the number of samples.

k	α	load	N=250	N=500	N=1000
0	12^o	C_l	0.66	0.70	0.71
		C_d	0.24	0.18	0.17
0.05	$17^o \downarrow$	C_l	1.30	0.63	0.63
		C_d	0.70	0.43	0.44
0.08	$20^o \uparrow$	C_l	1.00	1.40	1.40
		C_d	0.65	0.53	0.50

Control-volume surface location

The examination of all cases shows that the loads are not very sensitive to the locations of the upstream and the lower boundary surfaces, Figure 3.14. Changing the location of the top surface results in $\pm 4.5\%$ and $\pm 5\%$ uncertainty for the lift and drag values, respectively. It also should be noted that the top surface should not be very close to the airfoil because the level of the image noise in that area is high. Changing the location of the downstream surface gives $\pm 3\%$ uncertainty for lift values. The maximum uncertainty was observed for high angles of attack during dynamic stall regardless of the reduced frequency value and after static stall for the static case. Calculating drag values are very challenging. Some correction methods for the drag determination were introduced by Scarano, Van Oudheusden and their colleagues [43, 91, 124, 125, 126]. For the dynamic case, the situation should be worse since stronger vortices with high velocity variation introduce significant uncertainties in the pressure field. In this study, when the effects of the control-volume surfaces were investigated and at the same time the corresponding vortical structure was examined, the trends of the results showed a significant uncertainty for the calculated drag value when a vortex center was close to the downstream control-volume surface. Figure 5.2 is used as an example for the case that the wake is dominated by vortices at $\alpha = 20.5^o \uparrow$ for $k = 0.08$. Three different locations (I, II and III) are marked in the near wake. According to the numerical simulation, C_d for this angle is predicted as 0.48 while the calculated PIV drag coefficients are 0.45, 1 and 1.2 when the downstream boundary is located at locations I, II and III, respectively, but the lift values do not differ. That means, closer to the center of the vortex, more uncertainty in the drag value is expected. Hence, there is a strong dependency of the drag value to the boundary location when the vortices are present. High velocity gradients from the vortices increase the level of uncertainty of calculated

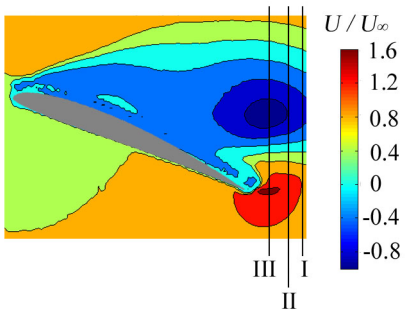

Figure 5.2: Downstream control-volume boundary locations; velocity field of $k = 0.08$ and $\alpha = 20.5^o \uparrow$.

pressure arrays. Since the magnitude of the drag is small compared to the lift and the pressure term is a dominant term for the load calculation, errors in the calculated pressure values result in inaccurate drag values; it can be concluded that the wake vortices affect the accuracy of the drag values.

Shifting the top boundary and the downstream boundary locations from close to the airfoil to $c/2$ away from it changes the lift values slightly for each angle of attack; averaging the mentioned calculated lift values give the final lift load for that angle. For drag calculation, the same method was used just for the top boundary. For the drag calculation, the control volume downstream boundary is fixed where the wake is less disrupted with the vortices. In some cases, the whole wake inside the field of view is covered with vortices and finding a good location for the downstream boundary is impossible; then, a larger field of view would be helpful, but the effects of spatial resolution should be considered.

Spatial resolution

The spatial resolution is introduced as the number of pixels over the chord length. Considering the same IA (16 pix), the fields of view $\frac{x}{c} = \frac{y}{c} \approx 1.4$ and $\frac{x}{c} = \frac{y}{c} \approx 3$ results in a maximum spatial resolution of 1500 pix/c and a minimum spatial resolution of 700 pix/c, respectively. In Table 5.2, for the static case at $\alpha = 6^o$, the calculated PIV lift value is almost converged for the resolution greater than 1200 pix/c and captures the numerical lift with an acceptable accuracy. Conversely, the drag value of this static angle is more accurate when the field of view is large; i.e. the spatial resolution of 700 pix/c. Figure 5.3 shows that at a small angle of attack, the near wake is occupied with a trailing edge vortex sheet, for the nature of a vortex sheet see Chapter 6. According to the discussion in the last

section, the vortices introduce error in PIV drag calculation; hence, for a large field of view, the downstream control volume can be far from the airfoil trailing edge where the effects of the vortex sheet can be ignored. For $k = 0.05$ at an angle of attack of $9^o \uparrow$ in Table 5.2, the PIV load values follow the same trends as the static case, but shifting to the dynamic airfoil, the contribution of the spatial resolution in calculating loads specially drag values is increased. At $\alpha = 17^o \uparrow$, the vortex sheets are replaced with rolling vortices, thus the small field of view of 1500 pix/c provides a reliable value for the drag since the whole near wake is not covered with vortices. At high angles, because of the highly separated flow, the PIV load values from the spatial resolution of 1500 pix/c are closer to the numerical ones than those from lower spatial resolution of 1200 pix/c. Figure 5.4 shows a comparison between the PIV drag cycle and the numerical drag loop, for the statistical uncertainties see Appendix C. For calculating the drag values from the PIV velocity fields, the large field of view (700 pix/c) for $0^o \leq \alpha \leq 11^o$ during upstroke and $0^o \leq \alpha \leq 5^o$ during downstroke was used and for the rest, the small field of view (1500 pix/c) was selected. There is good agreement between two methods.

The contribution of the spatial resolution will be highlighted by increasing k. In Table 5.2, For $k = 0.08$, the large field of view can not give a correct drag value for the angle of attack of $5^o \uparrow$, since a higher reduced frequency requires more spatial resolution; hence, for $k = 0.08$ and 0.12, if the spatial resolution of the large field of view is increased, drag values at low angles of attack provide accurate values. For the lift calculation, a higher reduced frequency requires more spatial resolution. For example in Table 5.2, for high spatial resolution, the difference from the numerical value is high for $\alpha = 21^o$ during upstroke because of the high reduced frequency ($k = 0.12$) as well as high angle of attack where the flow is highly separated. As another example, for $\alpha = 9^o \uparrow$ which is located in the linear part of the load curves with an unseparated boundary layer, the lift coefficient differences between the high spatial resolution PIV and the numerical approaches are 0.04, 0.07 and 0.13 for $k = 0.05$, 0.08 and 0.12, respectively. Therefore in this study, for load calculation purposes, the minimum possible field of view will be chosen to have the maximum spatial resolution. For the drag value, increasing the field of view increases the possibility of finding a proper location for the downstream boundary which is not covered with vortices, but at the cost of spatial resolution which plays a significant role in capturing real loads.

5.2.2 Static case

For the static case, as another alternative, the open source XFOIL program [23] has been used which is very popular for analysis and design of an airfoil. The XFOIL code calculates lift and drag of a subsonic airfoil based on the pressure distribution. The experimental

Table 5.2: Load determination sensitivity to the spatial resolution.

k	α	load	700 pix/c	1200 pix/c	1500 pix/c	numerical result
0	6^o	C_l	0.68	0.85	0.86	0.88
		C_d	0.04	0.03	0.02	0.04
0.05	$9^o \uparrow$	C_l	0.76	1.90	0.95	1.10
		C_d	0.09	0.03	0.02	0.08
0.05	$17^o \uparrow$	C_l	1.30	1.80	1.71	1.60
		C_d	0.12	0.50	0.48	0.45
0.08	$5^o \uparrow$	C_l	0.35	-	0.59	0.67
		C_d	-0.04	-	0.02	0.05
0.08	$21.5^o \downarrow$	C_l	0.32	-	1.06	1.00
		C_d	0.05	-	0.50	0.43
0.12	$21^o \uparrow$	C_l	1.04	-	2.20	1.95
		C_d	-0.02	-	0.70	0.79

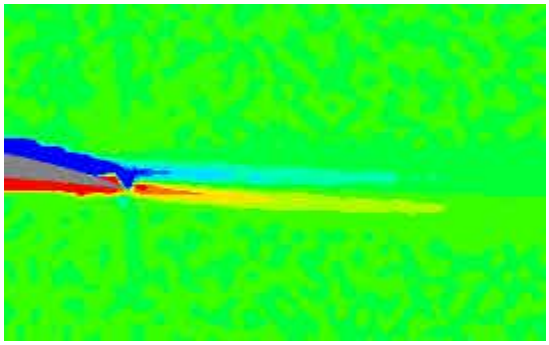

Figure 5.3: Trailing edge vortex sheet for the static airfoil at $\alpha = 6^o$.

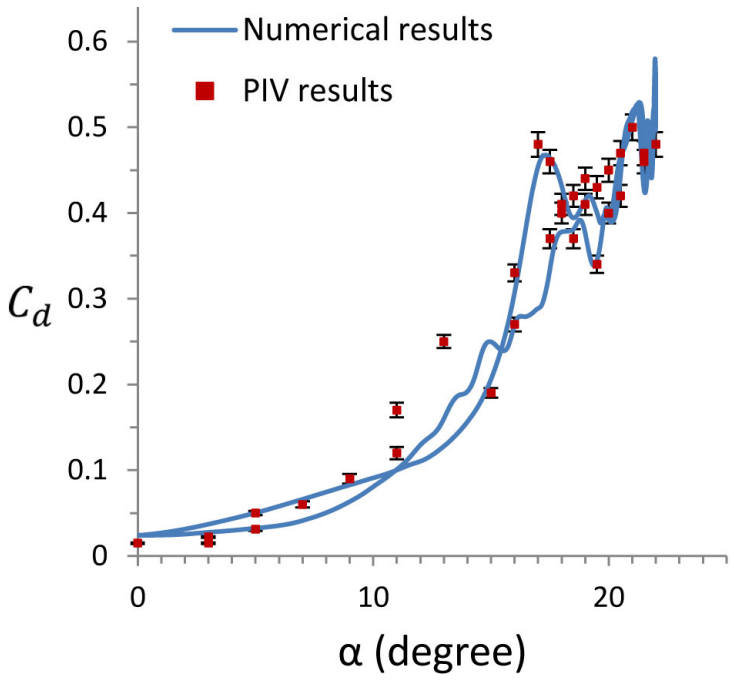

Figure 5.4: Comparison of the determined PIV (with the error bars) and numerical drag cycles for $k = 0.05$.

results of Selig et al. based on the pressure integration method [104] are available for Re $= 6 \times 10^4$. In Figure 5.5, the static lift values from the PIV method are compared with those of XFOIL [23] and the experimental results of Selig et al. [104]. For Re $= 6 \times 10^4$ at higher angles, XFOIL overpredicts the lift and drag values compared to the experimental method of Selig et al. [104]. The same condition was applied for Re $= 4 \times 10^4$; the XFOIL load values are higher than the current PIV results (except the drag values close to stall) and the stall points are very close. The trends of the load curves after stall are almost the same. This figure shows that the calculated PIV load values are reliable for the static case.

5.2.3 Dynamic case

Figure 5.6 shows a comparison between the numerical and experimental lift cycles for $k = 0.08$. The linear part of the lift cycle during upstroke, $\alpha \leq 16^o \uparrow$, from both methods almost cover each other with the same trend. For the area close to the dynamic stall angle ($\alpha = 18.5^o \uparrow$), the numerical simulation underpredicts the lift values. Both methods can predict two load peaks during upstroke. The most marked discrepancy between the PIV and numerical results occurs during downstroke motion because of the three dimensional nature of the flow during downstroke [128]. Although there is good overall agreement between the numerical and experimental load cycles especially during upstroke, analyzing the details of the vortical structure can be used as another indicator to show if the calculated loads correspond with the nature of the vortical structures.

The stages of the dynamic stall process from both PIV and numerical methods are plotted in Figure 5.7 for varying upstroke and downstroke angles, for the statistical uncertainties see Appendix C. Static pressure coefficient contours are also plotted in Figure 5.8. During upward pitch motion the flow is mainly attached except a small separated flow at the trailing edge as well as where the LSB is formed. A further increase in the angle of incidence results in LEV formation which is shown at $\alpha = 16^o \uparrow$ in Figure 5.7 and then at $\alpha = 17^o \uparrow$ in Figure 5.8 where the clock-wise LEV covers half of the suction side with low pressure values. Hence, the LEV causes a large pressure difference between the pressure and suction sides, resulting in high lift; then, when the LEV is developing the slope of the aerodyanmic load should be increased noticeably which is visible in Figure 5.6. The lift coefficient reaches the absolute maximum at the dynamic stall point. The stall angle is $\alpha = 18.8^o \uparrow$ by numerical prediction and $\alpha = 18.5^o \uparrow$ according to PIV data. The numerical approach postpones the dynamic stall about 0.3^o. Consequently, some of the subsequent aerodynamic events are postponed. Figure 5.7 illustrates that at the dynamic stall point the LEV covers the entire suction side with very low pressure. After the airfoil stalls, a

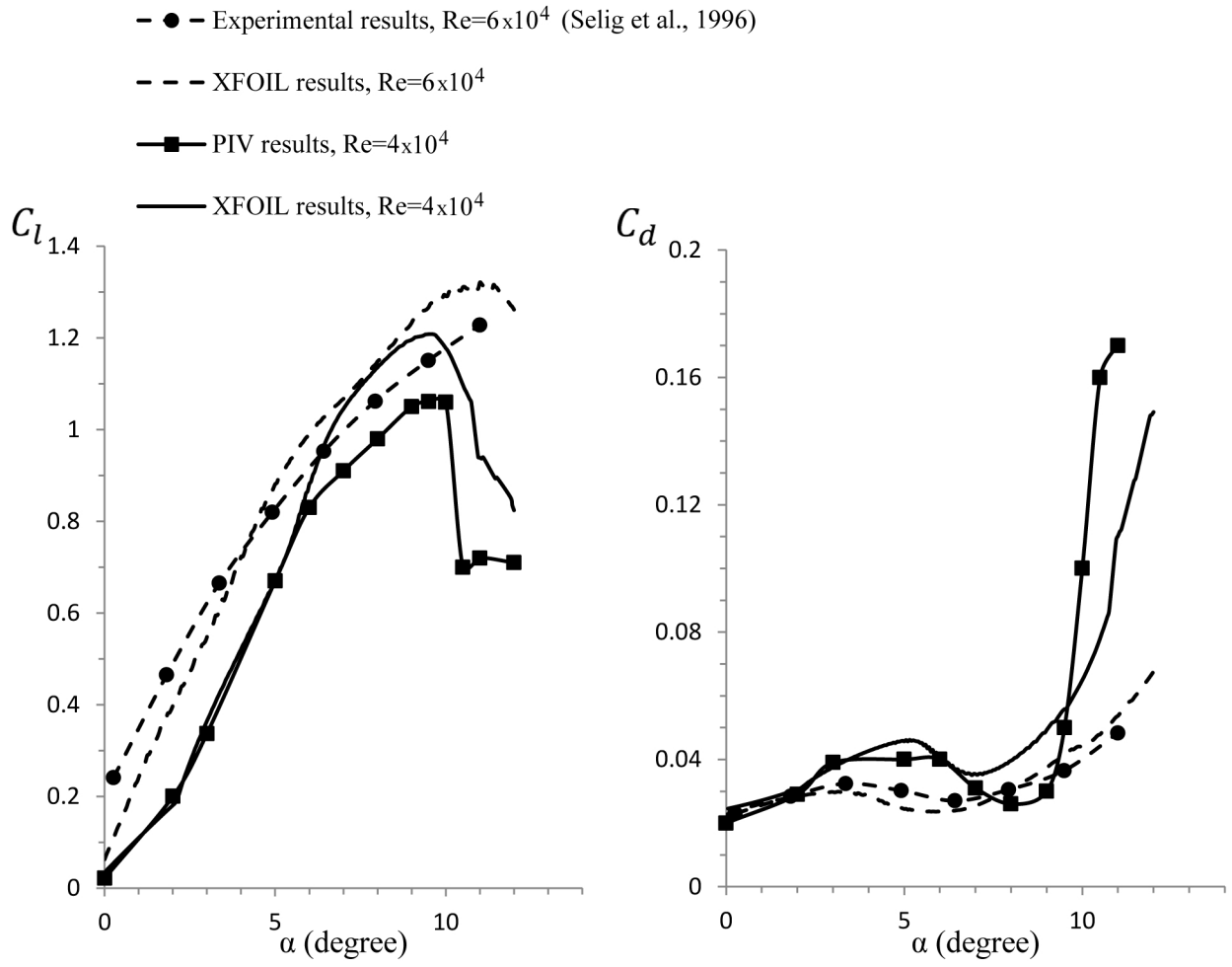

Figure 5.5: Static lift and drag coefficients of the SD7037 airfoil versus angle of attack including XFOIL results for $\mathrm{Re} = 4 \times 10^4$ and $= 6 \times 10^4$ and experimental results of Selig et al. for $\mathrm{Re} = 6 \times 10^4$ [104] and current PIV results for $\mathrm{Re} = 4 \times 10^4$.

counter-clockwise vortex from the pressure surface gradually rolls up at the trailing edge resulting in a quick drop in lift. At the end of full stall, this TEV reaches its maximum size and is shed into the wake. Following the streamline plots, emergence of a second LEV is evident at $\alpha = 20.5^o \uparrow$ from the PIV method and $\alpha = 20.7^o \uparrow$ from the numerical method, Figure 5.7. The growth of the second LEV enhances the lift performance during the upstroke motion though its strength subsides in comparison with the first LEV, Figure 5.6, as is evidenced by the higher pressure, Figure 5.8. At $\alpha = 22^o$ from the PIV method and $\alpha = 21.8^o \uparrow$ from the numerical method, the second LEV reaches the end of the airfoil, corresponding with a second lift peak during the upstroke motion while slightly before it the first trailing edge vortex is shed. As for the downward pitch motion, at $\alpha = 20.5^o \downarrow$ from the numerical simulation, the new LEV covers the whole suction side. The LEVs during the downstroke motion are not as strong as the upstroke and in turn do not significantly alter the aerodynamic loads. At $\alpha = 5^o \downarrow$ there is no sign of vortex formation, and the flow remains attached until the end of the cycle. It can be concluded that the load cycle trend coincides with the vortical structures of the flow.

5.3 Reduced frequency effects

5.3.1 LSB characteristics

Here the effects of the reduced frequency on the LSB characteristics and the laminar-turbulent transition are investigated with the aid of the PIV method. Since a LSB is smaller in dynamic cases compared to that found in static cases [57], capturing the laminar-to-turbulent transition and the LSB characteristics shows the ability of the high resolution PIV technique to detect the details of the boundary layer. For the location of the transition, normalized Reynolds shear stress $-\overline{u'v'}/U_\infty^2$ has been used as an indicator, similar to the study of Bansmer and Radespiel [6] who used $-\overline{u'v'}/U_\infty^2 \geq 0.1\%$. The laminar turbulent transition location (X_T) based on the chord length is shown in Figure 5.9. Moreover, the streamlines in this figure demonstrate the separation location (X_S) based on the chord length. The figure also shows the dependency of the separation and the transition locations on the reduced frequency. The trends of the transition location variation are shown in Figure 5.10a. Increasing the reduced frequency moves the transition location upstream. Moreover, a higher angle of attack results in an earlier transition location which is consistent with the results of other studies [30, 47, 64, 79]. The transition point moves upstream faster when the corresponding angle is closer to the LEV formation angle; thus in Figure 5.10a, a significant drop in the $k = 0.05$ curve exists. Based on the discussion in Section 2.4, the

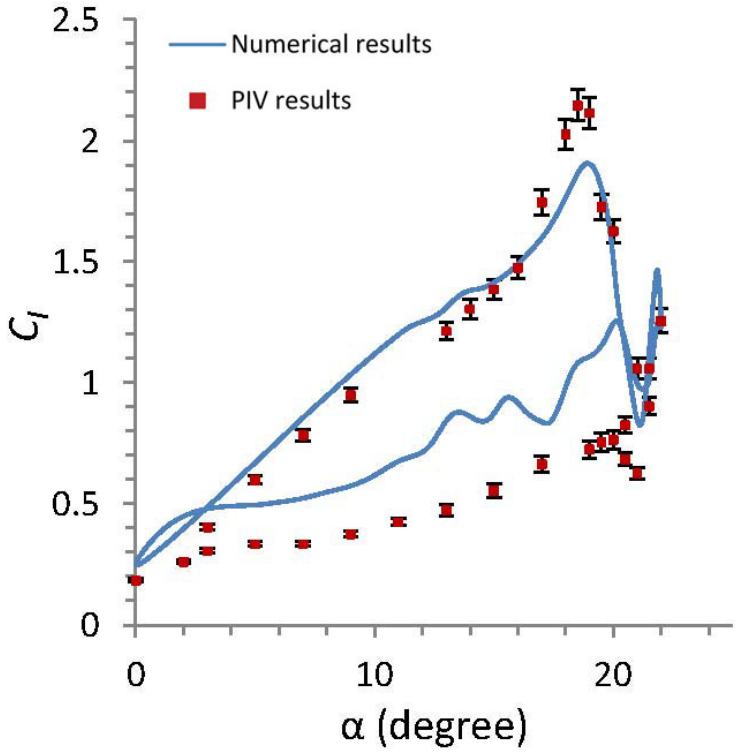

Figure 5.6: Comparison of the determined PIV (with the error bars) and numerical lift cycles for $k = 0.08$.

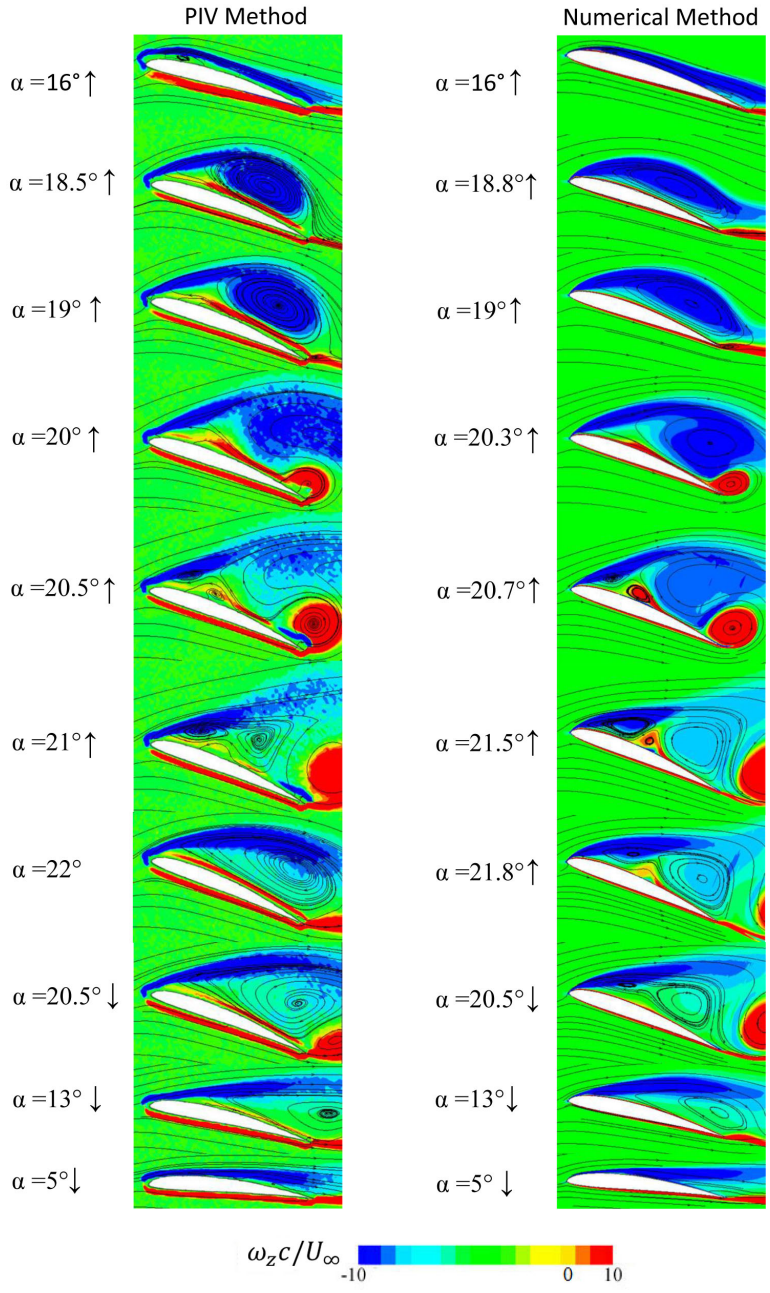

Figure 5.7: Experimental and numerical vortical structures for a pitch cycle of $k = 0.08$.

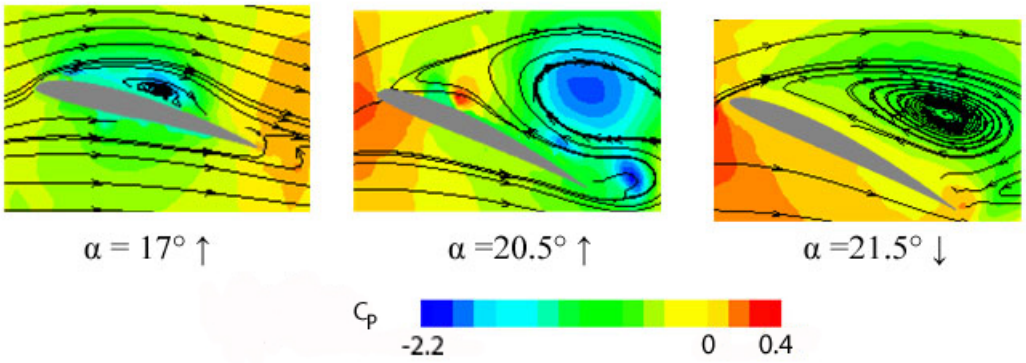

Figure 5.8: PIV pressure coefficient for $k = 0.08$.

height of the LSB (h_b) (the height of the LSB at transition location) is an indicator for the LSB size for a dynamic airfoil. Figure 5.9 as well as Figure 5.10b show a reduced frequency increase results in a thin LSB; therefore, the contribution of the LSB to aerodynamic effects is reduced when the reduced frequency is increased. It is obvious that higher Reynolds shear stress dominates the shear layer at a higher reduced frequency. The higher shear stress increases the energy of the boundary layer and then the separated bubble reattaches faster resulting in a smaller LSB. Figure 5.10b also indicates an almost linear trend of the h_b augmentation versus the angle increase. The h_b difference between the two angles is also visible in Figure 5.11. The h_b augmentation versus angle of attack increment is very similar to the trend of the bubble length versus angle of attack of a static Eppler 61 airfoil for $Re = 4.6 \times 10^4$ [101].

5.3.2 Lift cycles

Experimental lift coefficients from different reduced frequency values are shown in Figure 5.12. A high reduced frequency of 0.12 delays dynamic stall resulting in an augmented lift value. For $k = 0.12$, the only peak lift during upstroke is observed close to the end of the upstroke cycle. Decreasing k to 0.08 results in two lift peaks in pitch up motion while the maximum lift magnitude is decreased compared to that of higher k. A similar result was observed by McCroskey et al. [68] for a NACA0012 airfoil while k varied considerably. Further k reduction results in three lift peaks with much lower lift values. For $k = 0.12$, the first lift peak during downstroke is noticeable; for $k = 0.08$, the magnitude of the first downstroke lift peak is decreased and for $k = 0.05$ the peak has almost vanished. Based on the vortical structure, each lift peak indicates a developing LEV which meets the trailing

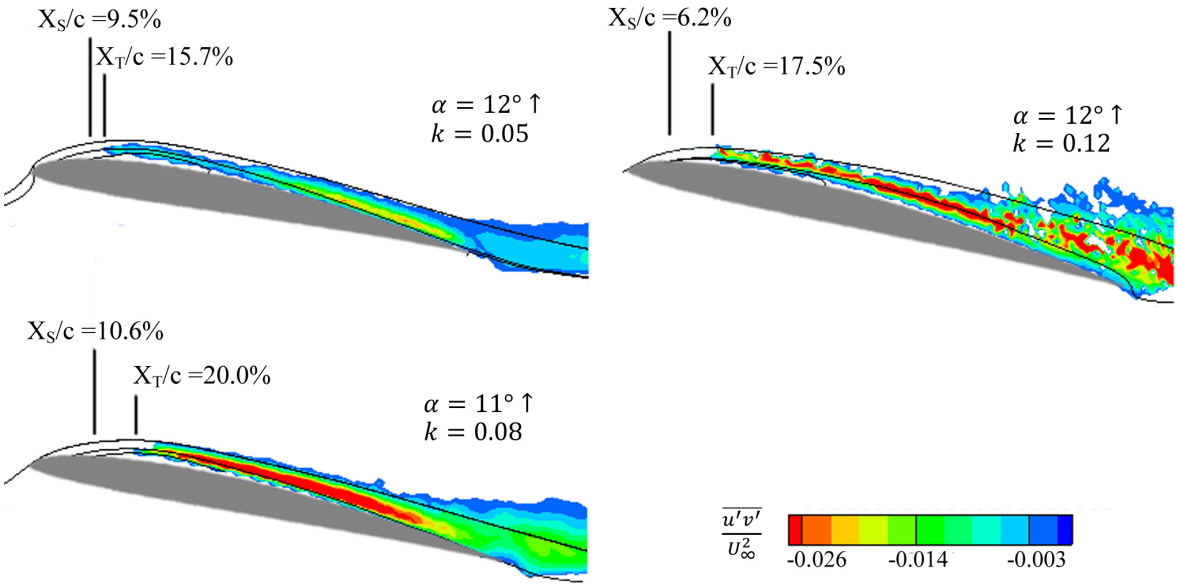

Figure 5.9: LSB characteristics versus reduced frequency based on normalized shear stress superimposed with the streamlines; X_T: laminar-turbulent transition location based on the chord length; X_S: separation location based on the chord length.

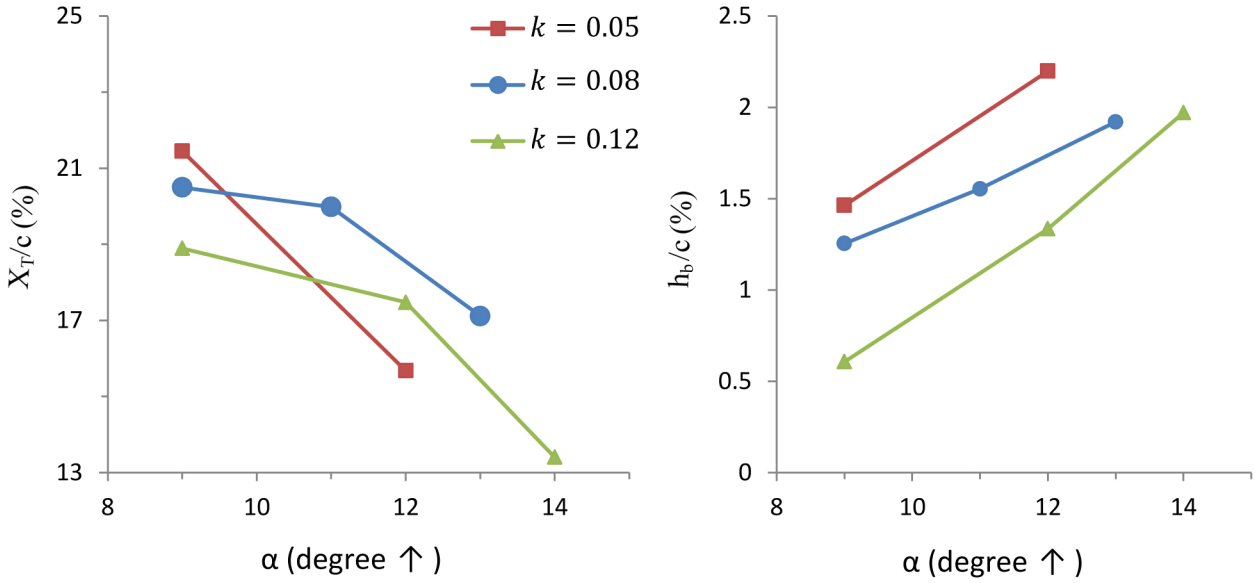

Figure 5.10: Reduced frequency effects on (a) Laminar-turbulent transition location, X_T, and (b) LSB height, h_b (the height of the LSB at the transition location); lines for visualization only.

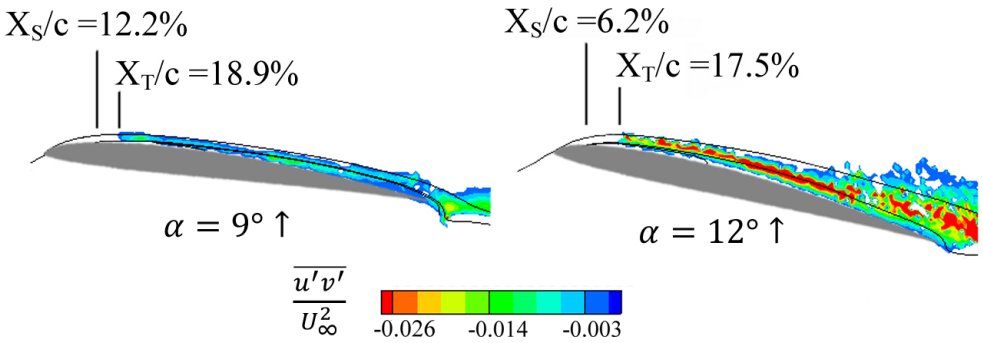

Figure 5.11: LSB characteristics versus angle of attack (k = 0.08) based on normalized shear stress superimposed with the streamlines; X_T: laminar-turbulent transition location based on the chord length; X_S: separation location based on the chord length.

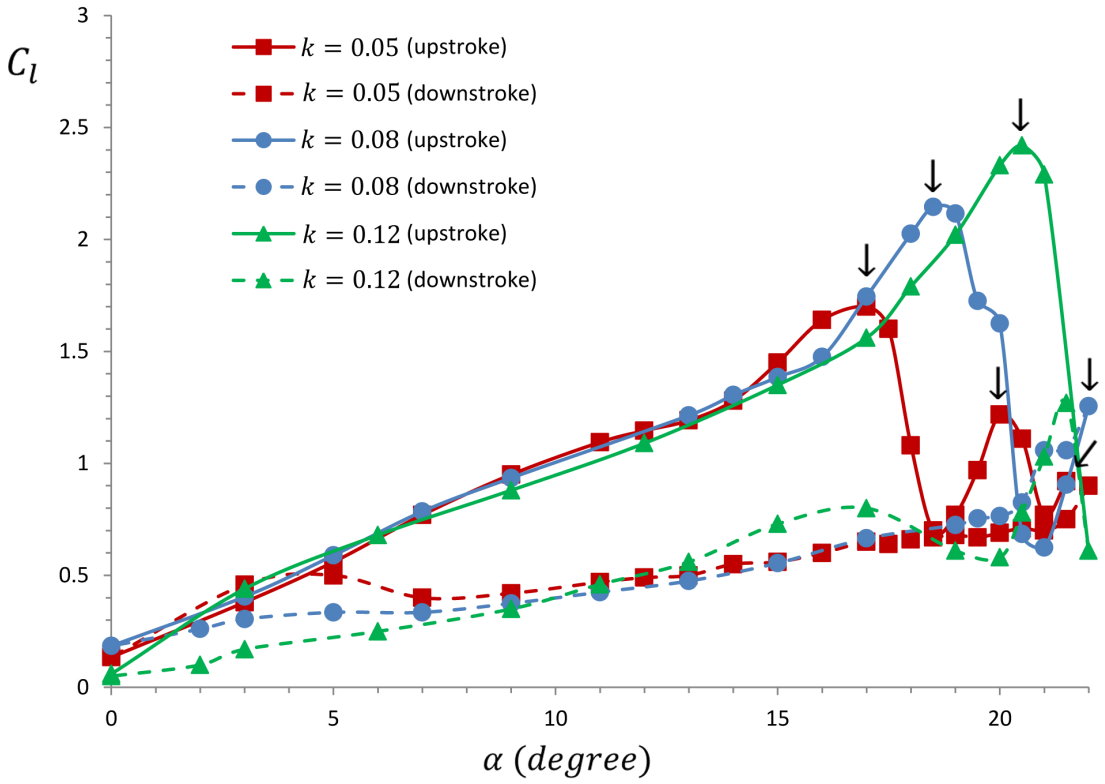

Figure 5.12: Effects of the reduced frequency on determined lift coefficients from the PIV velocity fields; arrows show lift peaks during upstroke.

edge of the airfoil. Since decreasing the reduced frequency advances dynamic stall, the boundary layer feeds low strength dynamic stall vortices (see Section 5.3.3); then, the results show that the PIV lift calculation method can capture the lift peaks associated with even weak vortices.

5.3.3 Vortex circulation

Comparison between Figures 5.12 and 5.13 reveals the contribution of the LEV to the lift trend. A higher reduced frequency increases the circulation of the LEV vorticity resulting in lift augmentation. After stall the TEV rolls up and increases in size and strength. Significant lift reduction during post stall indicates the negative effects of the TEV. Therefore, there should be a strong correlation between the strength of the LEV and the correspond-

ing TEV in terms of the magnitude of the circulation as is obvious in Figure 5.13 which agrees well with the results of Prangemeier et al. [85]. When the TEV reaches its maximum circulation, it separates from boundary layer and at this angle the lift value starts to increase because the next formed LEV causes the second lift peak. The higher lift peak at dynamic stall results in a lower lift value at the end of the lift reduction process. That means, the higher TEV circulation results in more lift drop during post stall.

It should be noted that for $k = 0.12$, the lift drop occurs in a very short time between angles 22^o and $21.8^o \downarrow$ where the TEV reaches the maximum value. Because of the high frequency of oscillation for this case, it was impossible to get the experimental data between angles 22^o and $21.8^o \downarrow$. Thus, in Figure 5.13, the experimental circulation values of the TEV are not available between angles 22^o and $21.8^o \downarrow$. To fill out this gap, the numerical circulation values of $k = 0.12$ are provided in this figure. A good agreement between numerical and experimental results exists. As discussed before, the numerical results slightly underpredict the lift values during stall and then the corresponding vortex circulation from the numerical simulation is slightly lower. The dynamic stall angle difference between the two methods is about 0.5^o which is visible as a 0.5^o shift between the curves of the two methods in Figures 5.13.

Phase delay ($\Delta\alpha$) and pinch-off process

When the LEV is fed by the boundary layer, the strength of the vortex is increased until it pinches off while the circulation of the vortex reaches the maximum value. The phase difference between the dynamic stall angle and the angle of the maximum vorticity circulation of the dynamic stall LEV is called phase delay ($\Delta\alpha$). Rival et al. [95] found for their case study that there was a negligible phase delay and thus the rolled-up TEV formation occurred right after the maximum LEV circulation. Panda and Zaman [82] mentioned that after vortex separation, the lift drops. Here, with the aid of the high resolution velocity gradients from the PIV velocity field, it is possible to see a significant phase delay ($\Delta\alpha$) and the rolled-up TEV formation occurred right after the maximum lift value (dynamic stall angle). Based on the current results, Figure 5.13, the LEV does not always separate immediately after stall and it depends on the reduced frequency. For $k = 0.12$, 0.08 and 0.05, $\Delta\alpha = 1^o$, 0.5^o and 0^o are seen, respectively, which all agree with those of the numerical results. For the first LEV, the vortex growth time, the time between the vortex generation until vortex pinch-off, shows an increased rate as k increases. That means, as the vortex growth time increases, the boundary layer feeds the vortex resulting in higher vorticity values and then a higher lift peak. As the vortex growth time decreases, more LEVs are observed during upstroke, two LEVs for $k = 0.08$ and three LEVs for $k = 0.05$

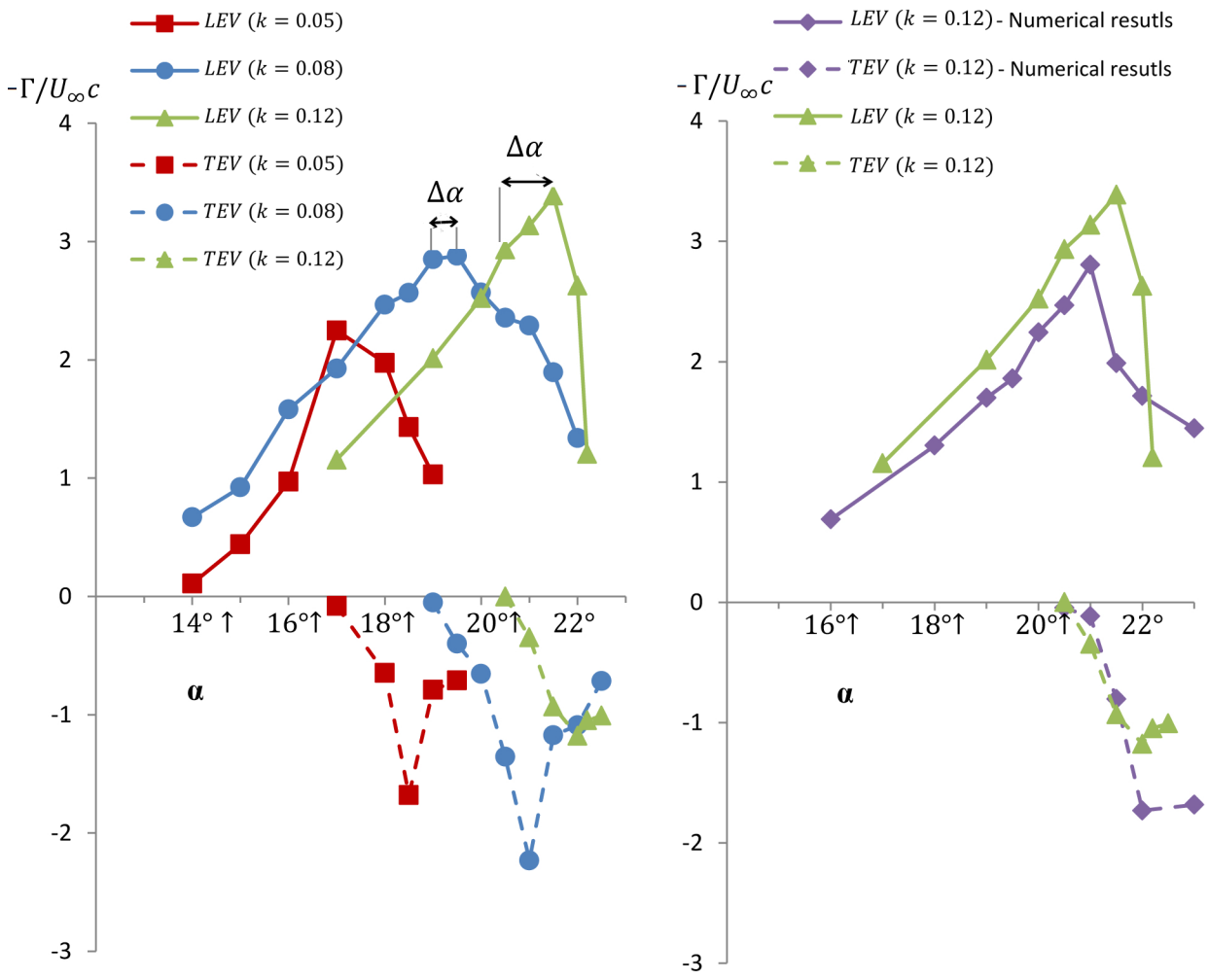

Figure 5.13: Circulation of dynamic stall vortices; left: PIV results for k =0.05, 0.08 and 0.12; right: PIV and numerical results for k =0.12.

which agree with the numerical results as well.

5.3.4 Vortex trajectory

The locations of the dynamic stall vortices are tracked in Figure 5.14. Slightly after LEV formation, the slope of the lift curve increases which corresponds to $\alpha = 15^o$, 16^o and 17^o for $k = 0.12$, 0.08 and 0.05 in Figure 5.12, respectively. Figure 5.14 shows that despite the reduced frequency and the angle difference, the streamwise location of the LEVs at these three angles is the same. Before stall, the LEV is located close to the top surface of the airfoil, as the angle of attack increases the center of the vortex mass moves down with the airfoil surface. At higher frequency, since the angle of the vortex formation and development is higher, the curves in Figure 5.14 are located slightly lower. The approximate speeds of the LEV traveling over the top surface of the airfoil are $13\% - 20\%$ of the freestream velocity. Recorded speeds of LEV convection over an airfoil show noticeable variation such as 30% of the freestream velocity from Chandrasekhara and Carr [20] and 55% of the freestream velocity from Ericsson and Reding [25]. Different locations of the LEV at the dynamic stall angle have also been reported. The midchord location was reported by McCroskey et al. [68] while Lee and Gerontakos [57] located the vortex close to the trailing edge. Here, when dynamic stall occurs ($\alpha = 20.5^o$, 18.5^o and 17^o for $k = 0.12$, 0.08 and 0.05), the centers of the vortex mass are at 75% of the chord length. Interestingly, it is the same location for all three observed cases. After stall, both TEVs and LEVs move upward, but as the vortex vorticity increases (for higher k values), it moves upward more slowly and it is closer to the airfoil surface. LEV separation from the boundary layer does not affect the trend of the vortex location. On the contrary, when the TEV reaches the maximum strength and pinches off ($\alpha = 18.5^o$, $\alpha = 21^o$ and $\alpha > 17^o$ for $k = 0.05$, 0.08 and 0.12), both LEV and TEV shift downstream and for the LEV a significant downward drop is observed. For a LEV with small vorticity (low k value), the drop is more significant. After a small angle change of 0.5^o, the LEV moves downstream and upward. It should be noted that the data between angles 22^o and $21.8^o \downarrow$ for $k = 0.12$ are not available showing that in this small angle increment the vortex grows and moves very rapidly. For the TEV of $k = 0.08$, at $\alpha = 22^o$, changing the direction of airfoil pitch at the end of the stroke results in a significant downward movement of the vortex and after a small angle of 0.5^o, the vortex moves upward during downstroke. For far downstream, upward movement of the vortices is the same for both up and down strokes, as was observed in other studies in far downstream [137].

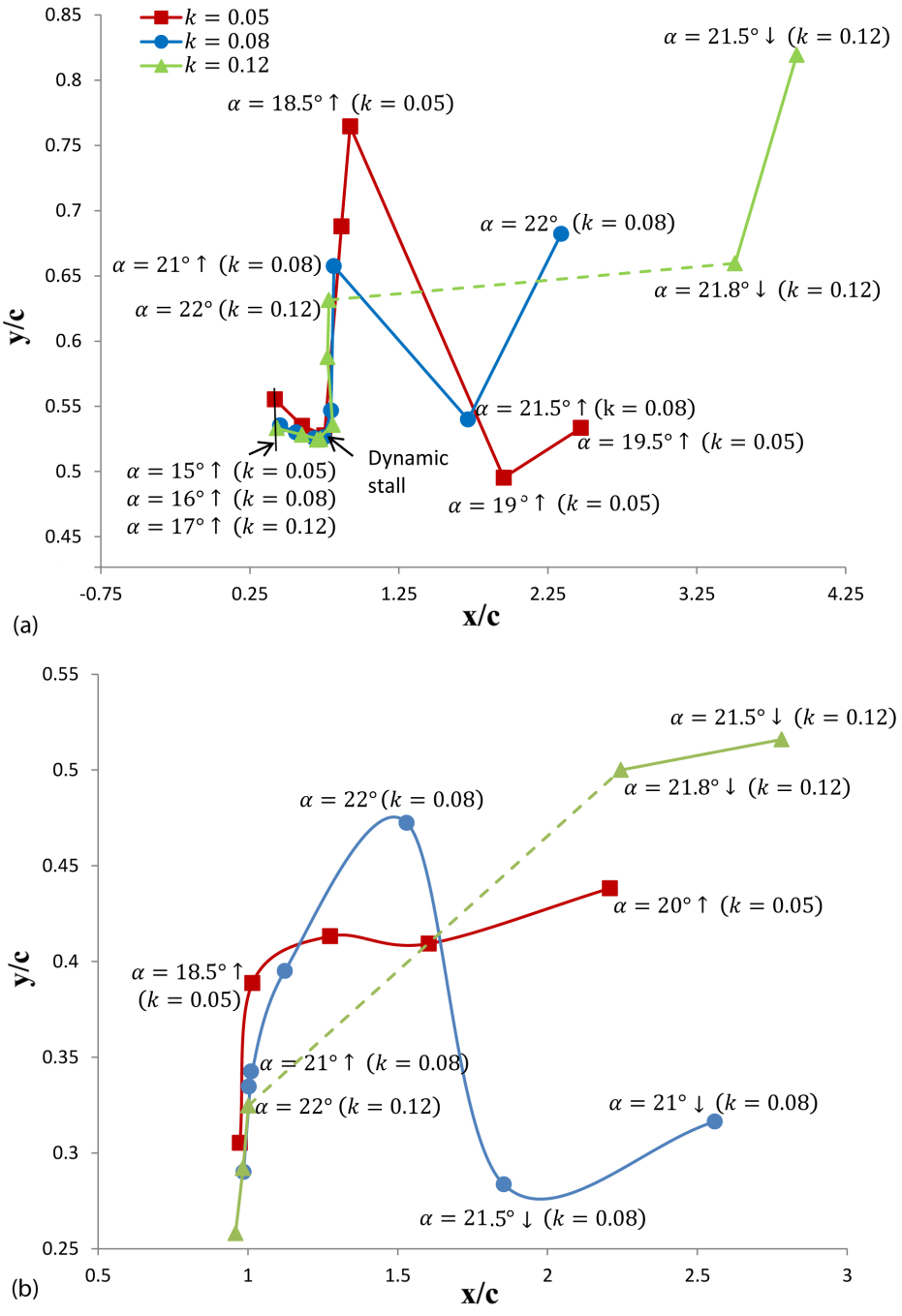

Figure 5.14: Locations of center of vortices for different k and α; (a) LEV ; (b) TEV; broken line: data is not available; lines for visualization only.

5.4 Summary

The main achievement of this chapter was calculating aerodynamic loads from the PIV control volume approach not only for the dynamic airfoils but also for deep dynamic stall phenomena. In this regard for a qualified PIV load determination strategy, the following points should be considered. Increasing the number of images above 500 does not provide more accurate loads and for visualization purposes a much lower number of images are sufficient. The PIV drag errors are mostly attributed to the high velocity gradient from vortical structure of the wake. In this regard, finding a location for the downstream control-volume boundary which is not distributed with the vortices is essential, but the lift coefficient is not very sensitive to the vortical structure. The PIV load determination accuracy depends directly on the spatial resolution especially for dynamic cases with high reduced frequencies and high angles of attack. To decrease the small discrepancy coming from the varying location of the top and downstream control-volume boundaries, the resultant calculated lift was averaged for the specific domains but for calculating drag, the downstream boundary is excluded. There is a reasonable agreement between the numerical load and PIV load loops. Moreover, the determined PIV lift loops correspond with the all vortical structure of the follow.

The results have also shown that, a low reduced frequency advances the dynamic stall angle and moves the fully developed secondary LEV to the upstroke. For $k = 0.05$, three LEV form during upstroke, for $k = 0.08$, the number of the LEVs reduces to two and finally for $k = 0.12$, just one LEV is fully developed during the upstroke while the lift augmentation regarding this vortex is significantly higher than the others.

In this range of the Reynolds number, the LSB appears in the oscillating cycles before LEV formation. The LEV advances at lower angles of attack with the reduction of k. That means, the LSB disappears faster for low k values. Normalized shear stress contours show that the transient location is moving upstream when either the reduced frequency or angle of attack is increased. The transition point moves upstream faster when the corresponding angle is closer to the LEV formation angle. Increasing k reduces the height of the bubble. Since the LSB usually affects the overall performance of the airfoil, LSB height reduction by increasing the reduced frequency should be considered.

Vortex circulation reveals more details regarding vortex characteristics. As the reduced frequency increases, the magnitude of the vortex (both LEV and TEV) circulation increases which corresponds with the lift behavior. Higher reduced frequencies increase the phase delay showing that even with a significant lift drop after stall, the boundary layer still feeds the LEV. There is a good agreement between calculated circulations from the numerical

and experimental methods; the numerical simulations underpredict the circulation values of the dynamic stall vortices similar to the dynamic stall lift. It is suggested that for the numerical methods, besides load comparison with the experimental ones, as another indicator, the circulations from the vortices should be compared. With the aid of the calculated whole velocity field from the PIV method, then calculating the circulations is possible.

The trajectory of the vortices shows that dynamic stall occurs when the center of the LEV is at 75% of the chord length regardless of the reduced frequency values. Not only is the circulation of the LEV and TEV linked together, the TEV contributes to the LEV location and vice versa. For example, when the LEV reaches the stall point (not the maximum circulation), the TEV starts rolling up; after stall, the LEV moves upward, but it does not move downstream until the TEV reaches its maximum circulation.

Chapter 6

Unsteady flow structures before stall (S822 airfoil, $3.5 \times 10^4 \leq Re \leq 10^5$)

The trailing edge vortices have a significant impact on the resultant wake structure and aerodynamic loads (Section 2.2), but less attention has been given to these vortices at low angles of attack when they appear mostly like vortex sheets. In Chapter 5, it was shown that the generated vortex sheet affects the load determination from the control-volume approach; a question is raised regarding the real structure of a vortex sheet. This chapter is organized to answer this question by experimental and numerical investigation of an S822 airfoil in pitching motion at low angles of attack for two Reynolds numbers, one without a laminar separation bubble and the other with the bubble. More details of the wake and the aerodynamic loads are also presented for the oscillating case within static stall angle.

6.1 Case studies and approaches

The airfoil oscillates sinusoidally according to Equation 2.2 where $\alpha_{mean} = 0^o$ and $\alpha_{amp} = 4^o$ and 8^o are presented for the experimental and numerical setup. The reduced frequency of $k = 0.025$, Equation 2.3, was fixed for all cases.

Smoke wire flow visualization [80] and PIV images show the vortical structures of the static and dynamic cases for $Re = 3.5 \times 10^4$ and $Re = 10^5$. The airfoil was sized to maximize the Reynolds number. Laser Doppler Anemometry (LDA) was employed for the wake study and mean drag measurements for $Re = 10^5$ while the data were measured at

the mid-span of the airfoil at $x/c = 1.25$ from the trailing edge; the coordinate system is shown in Figure 3.9.

For all cases, a numerical simulation with the Transition SST method for $Re = 10^5$ and with the laminar assumption for $Re = 3.5 \times 10^4$ has been employed.

6.2 Flow visualization

Numerical and experimental flow visualization of static and dynamic cases are presented for two Reynolds numbers ($Re = 3.5 \times 10^4$ and 10^5). For $Re = 3.5 \times 10^4$, Figure 6.1 shows repeatable shedding vortex structures resembling von Karman vortex-shedding patterns. As the angle of attack increases, the separation points move forward [49] and the trailing edge boundary layer thickness increases resulting in larger vortices with lower shedding frequencies. At $\alpha = 8^o$, the shear layer filament of this thick airfoil is extended in the streamwise direction in the near wake. Vortex shedding frequencies of 340 Hz and 580 Hz were reported for $\alpha = 8^o$ and $\alpha = 0^o$ [80], respectively. The vorticity field from the numerical simulation agrees well with the smoke wire experimental results. Shifting to the dynamic case, the same vortex pattern was obtained, shown in Figure 6.2. The vortex shedding pattern resembles the von Karman pattern and the dynamic oscillation of the airfoil does not change the organized vortex pattern. Similar to the instantaneous images, the same repeatable shedding vortex pattern is visible in the phase averaged PIV vorticity field as well as the numerical results. From the figures of the static and dynamic cases, the boundary layer is separated from the suction surface. Oil surface visualization also showed that the separated boundary layer was not reattached for the static case of $Re = 3.5 \times 10^4$ [80].

As the Reynolds number increases the separated bubble reattaches to the airfoil and forms an LSB. For $Re = 10^5$ of this study, the separated boundary layer is reattached to the suction surface, Figure 6.3a at $\alpha = 3^o$. Also in Figure 3.3, the separation and reattachment lines marked by the oil surface visualization technique indicated the existence of the LSB. Yarusevych et al. [140] showed that for the static NACA 0025 airfoil, as the Reynolds number increases and the LSB forms ($Re = 1.5 \times 10^5$), the vortical structure was affected and an unorganized vortex pattern with a narrow wake was formed. The PIV images in Figure 6.3 at $Re = 10^5$ show that there is no specific shedding vortex pattern and the random location of the vortices in the wake results in two parallel shear layers of phase averaged PIV velocity fields in the near wake. As the angle of attack increases, the location of the LSB moves forward [80] (Figure 6.3b shows an attached flow in the vicinity of the trailing edge). Figure 6.4 shows that similar to the static case, the vorticity fields of the

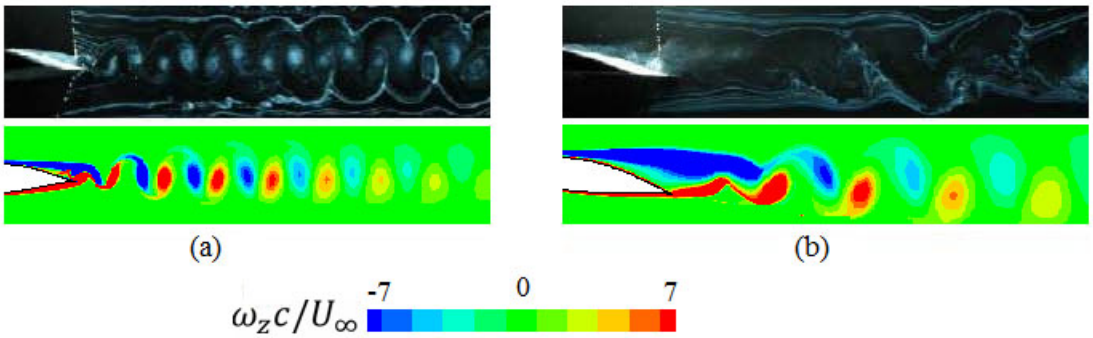

Figure 6.1: Flow patterns of the static case for $Re = 3.5 \times 10^4$; upper: smoke wire photographs [80]; lower: vorticity field from numerical simulation; a) $\alpha = 0^o$; b) $\alpha = 8^o$.

PIV method as well as numerical simulation of the dynamic airfoil show that the random locations of the vortices form vortex sheets as they convect downstream until they separate from the shear layer. In this case, the LSB forms at $\alpha > 5^o$, showing a delay of boundary layer transition compared to the static case, agreeing with the results of Gerontakos [30]. Figure 6.4a shows that at $\alpha = 3^o \uparrow$ the flow is separated without reattachment, but at higher angles of attack such as $\alpha = 8^o$ the flow is mostly attached to the airfoil, Figure 6.4b. That means, regardless of the LSB existence, the vortex patterns are not organized for the dynamic case at higher Reynolds number resulting in trailing edge vortex sheets which are also consistent with the numerical results.

6.3 Wake study at $Re = 10^5$

The numerical results for $Re = 10^5$ are also validated by the LDA measurements shown in Figure 6.5. This figure illustrates the averaged mean velocity for dynamic cases with amplitude of 4^o and 8^o showing good agreement between the numerical and experimental results. Increasing the amplitude changes the structure of the averaged mean velocity from one peak structure to a double peak structure with a lower velocity deficit. Figure 6.6 shows that a higher amplitude causes a broader velocity wake profile with a smaller velocity deficit at most phase angles causing the double peak structure for the averaged one shown in Figure 6.5. The airfoil oscillation makes a narrower wake than that of the static airfoil resulting in increased velocity deficit, Figure 6.6, also shown by Lee and Gerontakos[57]. For the static case, the LSB decreases the size of the velocity wake [139], but in Figure 6.6a for the dynamic case, no significant changes in the wake velocity profile are seen after LSB

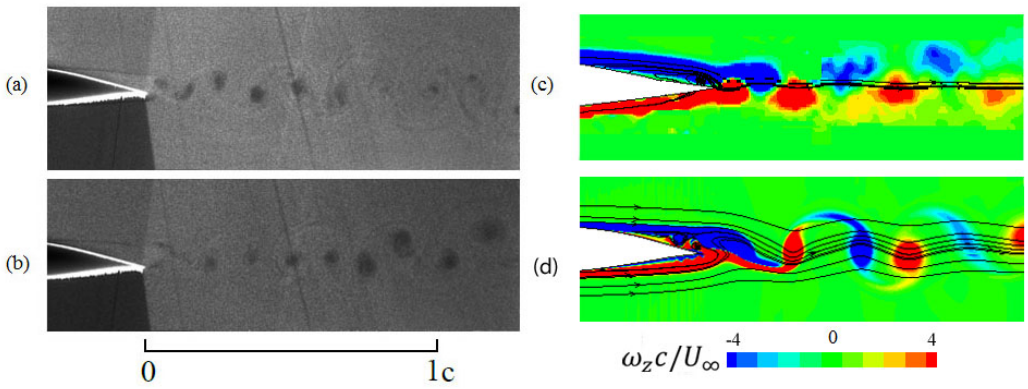

Figure 6.2: Flow patterns of the dynamic case for $Re = 3.5 \times 10^4$, $\alpha = 8\sin(2\pi ft)$ and $k = 0.025$; a) $\alpha = 0^o \uparrow$ (an instantaneous PIV image); b) $\alpha = 0^o \downarrow$ (an instantaneous PIV image); c) $\alpha = 0^o \uparrow$ (phase averaged PIV vorticity field); d) $\alpha = 0^o \uparrow$ (numerical vorticity field).

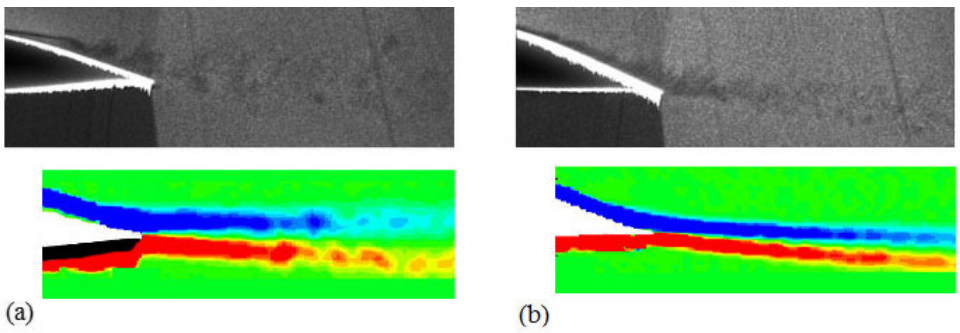

Figure 6.3: Flow patterns of the static case within 1c of the wake for $Re = 10^5$; upper: instantaneous PIV image; lower: phase averaged PIV vorticity field; a) $\alpha = 3^o \uparrow$; b) $\alpha = 8^o$; for legend see Figure 6.2.

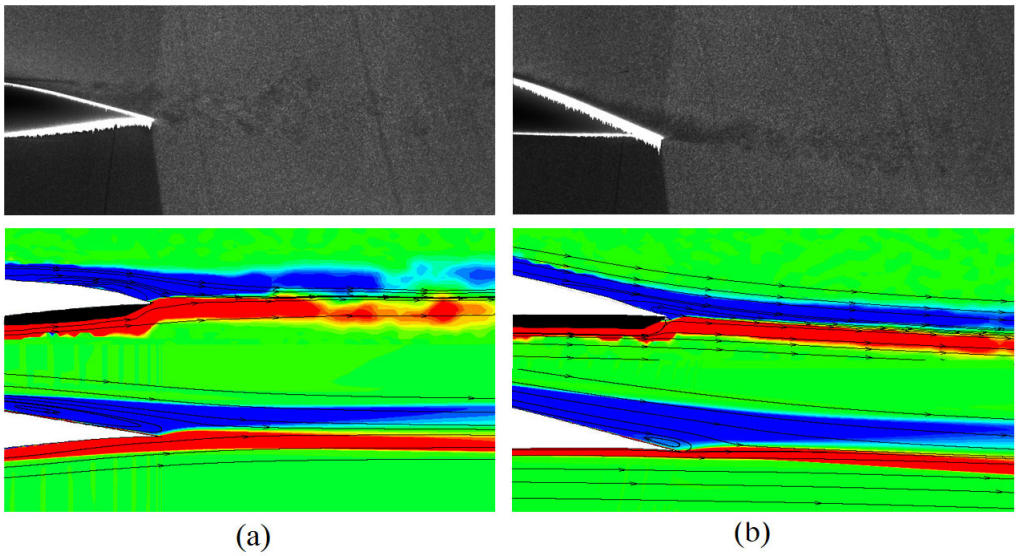

Figure 6.4: Flow patterns of the dynamic case within 1c of the wake for $Re = 10^5$, $\alpha = 8\sin(2\pi ft)$ and $k = 0.025$; upper: instantaneous PIV images; middle: phase averaged PIV vorticity fields; lower: numerical vorticity fields; a) $\alpha = 3^o \uparrow$ (upstroke); b) $\alpha = 8^o$; for legend see Figure 6.2.

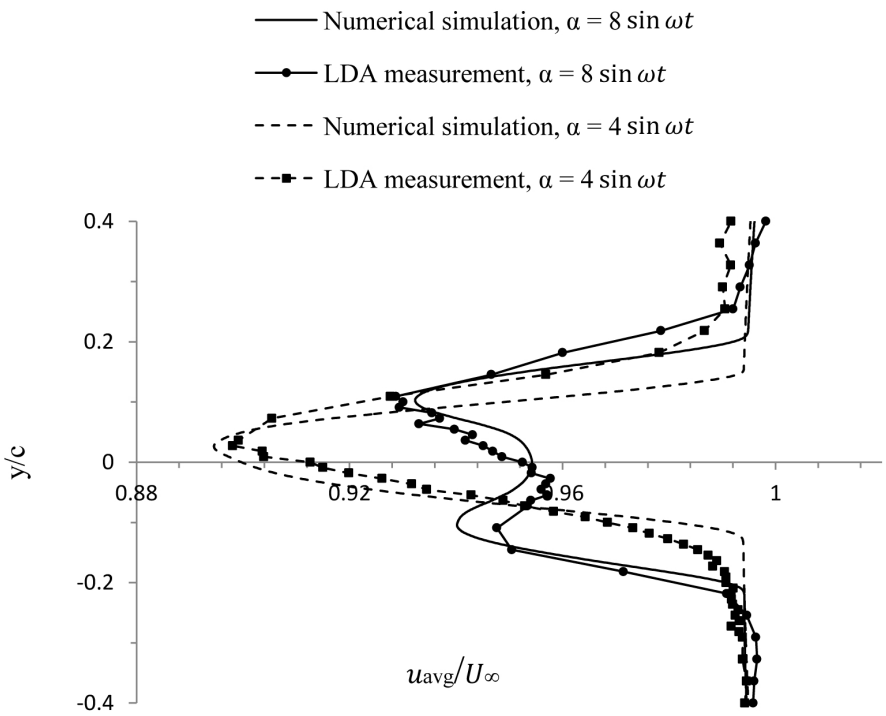

Figure 6.5: Averaged streamwise mean velocity profiles ($x/c = 1.25$ and $Re = 10^5$)

formation.

For the simulations, Turbulent Viscosity Ratio (TVR) contours indicates laminar-to-turbulent transition. The TVR is defined as

$$\text{Turbulent Viscosity Ratio (TVR)} = \frac{\text{turbulent viscosity } (\mu_t)}{\text{molecular viscosity } (\mu)} \tag{6.1}$$

and is an indicator of the flow turbulence behavior. If μ_t is greater than almost two orders of magnitude of μ, the flow can be considered as turbulent [129]. Here, based on the TVR field, the flow is considered as turbulent when the TVR is close to 100. For dynamic cases at low angles of attack, the bubble does not reattach. Figure 6.7a indicates that laminar to turbulent transition occurs in the separated boundary layer area close to the trailing edge of the airfoil when $\alpha = 4sin(2\pi ft)$. Figure 6.7b, c show the averaged turbulent intensity and kinetic energy profiles at $x/c = 1.25$. The discrepancy between

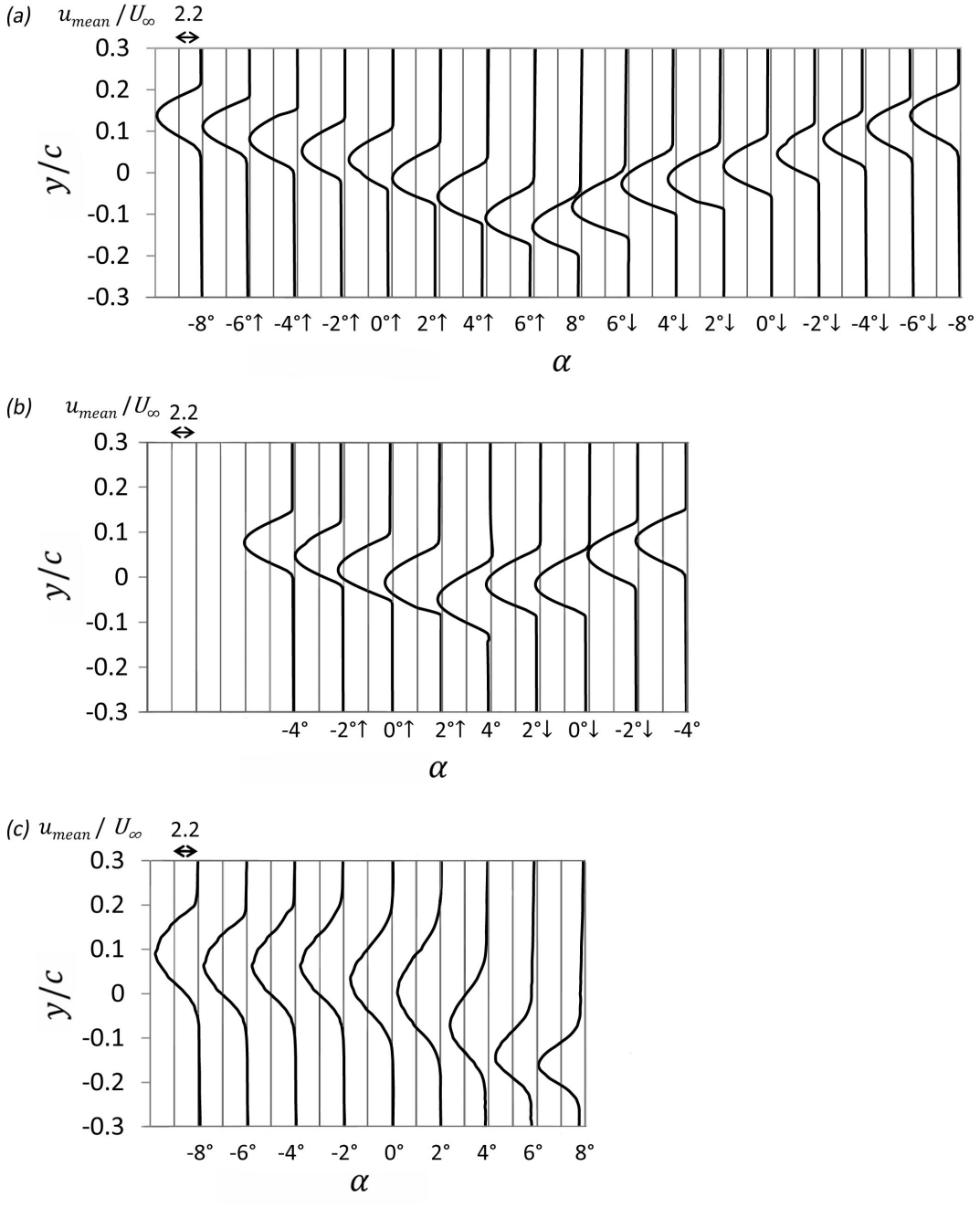

Figure 6.6: Streamwise mean velocity profiles; a) $\alpha = 8sin(2\pi ft)$, numerical results; b) $\alpha = 4sin(2\pi ft)$, numerical results; c) static case, LDA measurement (averaged values).

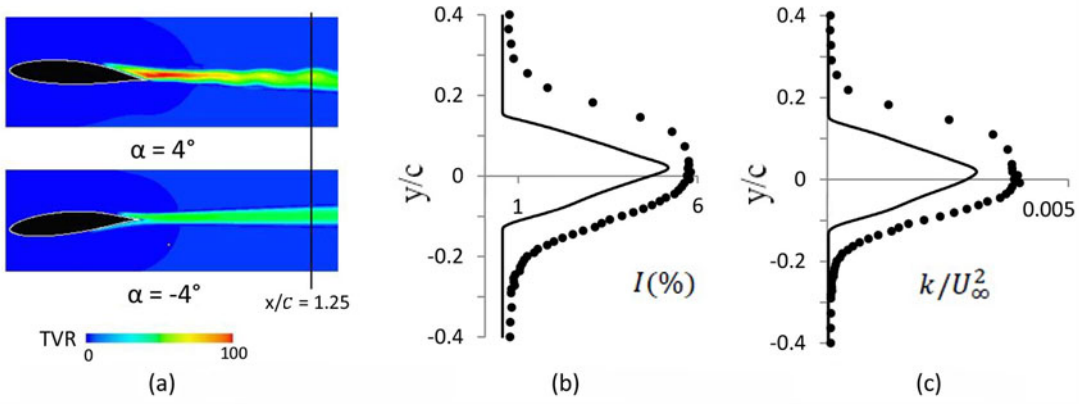

Figure 6.7: Turbulent parameters for $\alpha = 4\sin(2\pi ft)$ ($Re = 10^5$); (a) Turbulent Viscosity Ratio (b) averaged turbulent intensity ($x/c = 1.25$) (c) non-dimensional averaged kinetic energy ($x/c = 1.25$); solid line: numerical results; data: LDA measurement.

numerical and experimental results show that the Transition SST method predicts a narrower and less turbulent wake compared to the experimental results. Numerical turbulent intensity profiles for each phase and experimental turbulent intensity profiles for the static case are shown in Figure 6.8. For all phases, a double peak structure is obvious representing the shear layer cores [139]. Although the numerical method underpredicts the turbulent variables, a comparison between dynamic and static cases reveals a narrower, but more turbulent wake for the dynamic cases [57].

6.4 Aerodynamic loads

Figure 6.9 shows the range of the unsteady loads that the blade element experiences at each cycle compared with the static case from experimental results [105]. For the selected amplitudes and reduced frequency reported here the aerodynamic loads are very close to the static ones, but the unsteady behavior of the loading would imbalance the rotor. At each cycle, the mean drag value from the LDA measurement is also determined from equation 3.3 where $x/c = 1.25$. For $\alpha = 4\sin(2\pi ft)$, the mean drag values from numerical and LDA measurement are 0.0268 and 0.0275S$\pm$0.0009, respectively. For $\alpha = 8\sin(2\pi ft)$, the mean drag values from numerical and LDA measurement are 0.0282 and 0.0323$\pm$0.0011. The information related to the statistical uncertainties has been provided in Appendix C.

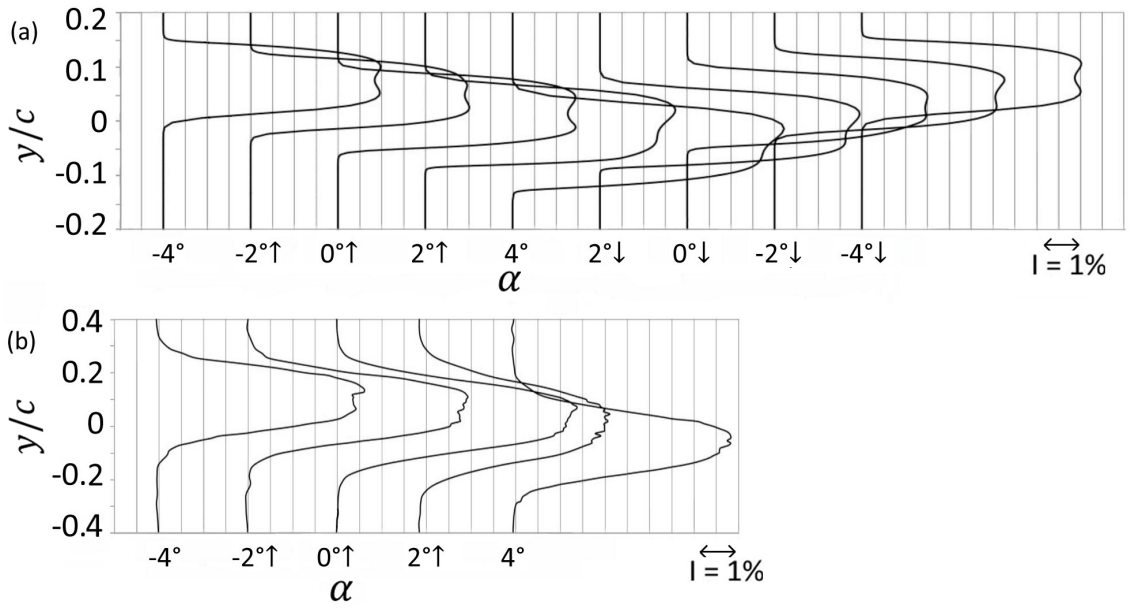

Figure 6.8: Turbulent intensity profiles ($x/c = 1.25$ and $Re = 10^5$) (a) $\alpha = 4\sin(2\pi ft)$, numerical simulation (b) static case, LDA measurement.

6.5 Summary

For both static and dynamic cases, there is overall agreement between numerical and experimental results. This study has revealed that at a low Reynolds number of 3.5×10^4, shedding vortices for dynamic and static cases resemble the von Karman vortex street. The organized shed vortices are also visible in PIV phase averaged vorticity fields as well as the numerical vorticity fields.

For both static and dynamic cases, numerical simulations predicted the separated boundary layer at $Re = 3.5 \times 10^4$ and the LSB at $Re = 10^5$. Compared to the static case, dynamic cases delay the LSB formation and the laminar to turbulent boundary layer transition. Although there is a good agreement between numerical and experimental results, the transition SST model slightly underpredicts the turbulent parameters.

For $Re = 10^5$, regardless of static or dynamic cases and with or without LSB formation, vortex sheets are replaced by vortices that shed to the wake without any organized pattern. Because of the random pattern of these vortices, following each individual vortex in an instantaneous vorticity field does not provide useful information; instead, the resultant vortex sheets can be studied. It is interesting that during dynamic stall, these random

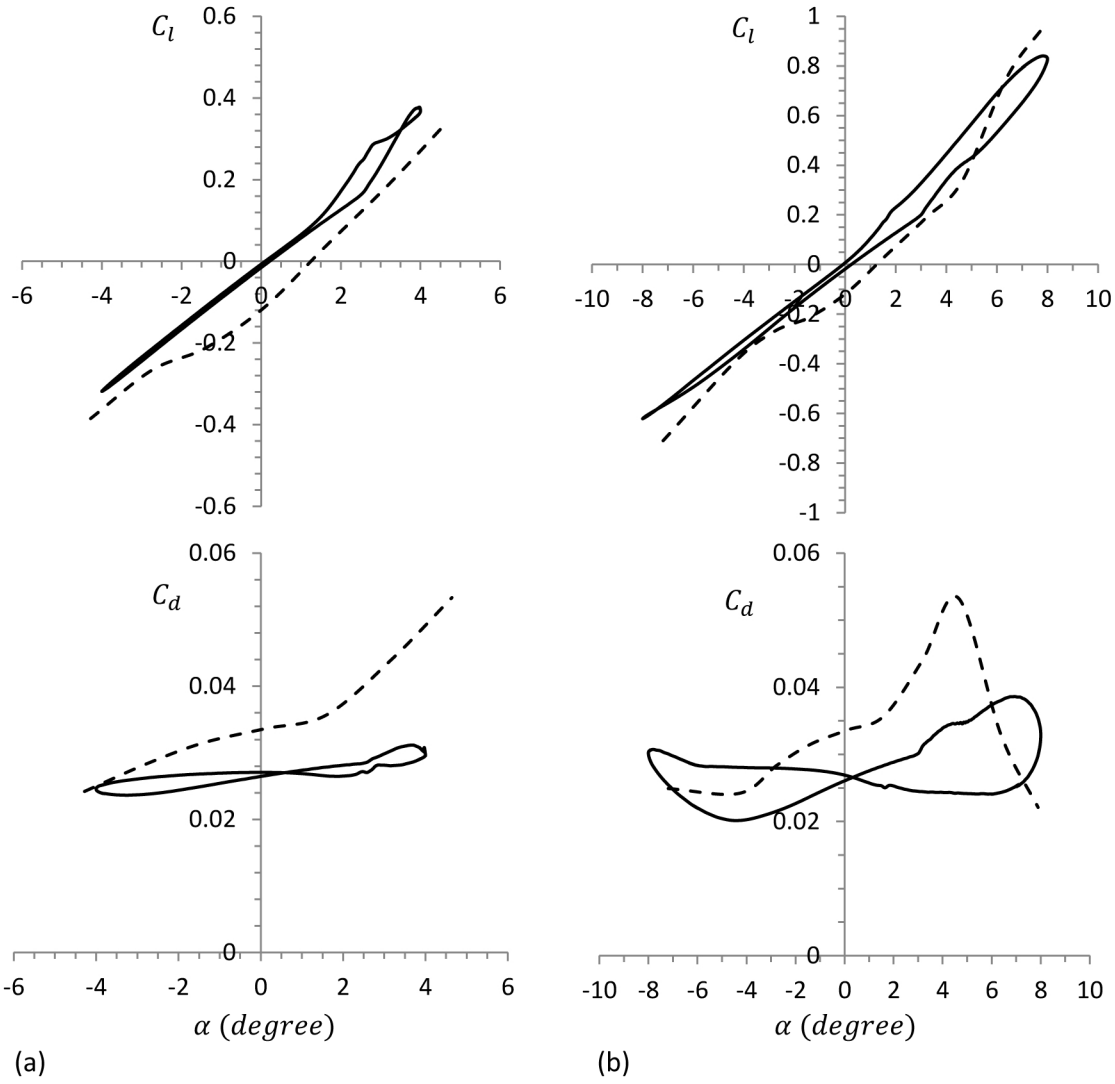

Figure 6.9: Aerodynamic loads ($Re = 10^5$); Solid lines: dynamic cases from numerical simulation; Broken lines: static cases from experimental result [105]; (a) $\alpha = 4\sin(2\pi ft)$, (b) $\alpha = 8\sin(2\pi ft)$

vortices are replaced with organized leading and trailing vortices; then one more definition should be added to the dynamic stall phenomena: dynamic stall phenomena shifts the random vortical pattern to the organized repeatable vortical pattern.

It should be noted that the results indicate the reason for selecting the S822 airfoil for this chapter. For the selected low Reynolds number boundary layer separation was observed and for the higher Reynolds number a LSB formed; then, the study could cover the contributions of the LSB.

For $Re = 10^5$, compared to the static case, the airfoil oscillations decrease the wake thickness but have higher turbulent intensity. The LSB decreases the wake thickness of the static airfoil, but it does not affect the wake thickness of the dynamic airfoil.

Increasing the amplitude of the oscillations makes a thicker boundary layer resulting in a low velocity deficit.

In one cycle, except at the LSB and the small trailing edge separated flow, the flow is mainly attached to the airfoil. Dynamic loads are close to the static values as expected from attached flows, but present unsteady aerodynamic coefficients that each blade element will face at each cycle. Overall, the results show that with the S822 airfoil at $Re = 10^5$, no significant difference between the static and dynamic cases with $\alpha_{amp} < \alpha_{static\ stall}$ was observed; then for large scale wind turbines, the small yaw errors do not change the overall performance of the blade element. Although the rotor experiences unbalanced loads, the maximum loads remain less than static stall ones.

Chapter 7

Unsteady freestream and dynamic stall (NACA0012 airfoil, $Re = 1.35 \times 10^5$)

Dynamic stall was studied under a steady freestream velocity in Chapter 5. Here effects of horizontal oscillations of the freestream velocity superimposed on a pitch oscillating NACA0012 airfoil are investigated using Computational Fluid Dynamics (CFD). Because of the oscillating freestream, discussions regarding the variation in the loads, the circulation of the dynamic stall vortex pairs, the critical angles, vortex growth time and the secondary lift peak locations are the objectives of this chapter. There is also a study in the shape and size of the vortex sheets (trailing edge vortices before stall, Chapter 6) and their contribution to load augmentation.

7.1 Specifications of simulated cases

A Single Oscillating State (SOS) means just the angle of attack is oscillating and the freestream is steady. The combination of both oscillating angle of attack and oscillating freestream is called a Coupled Oscillating State (COS).

Here, a NACA0012 airfoil was pitch oscillating according to the sinusoidal mode given in Equation 2.2. For the sinusoidally varying freestream, the horizontal velocity was oscillating governed by Equation 2.5. The details of the cases in this study are provided in Table 7.1 where the phase difference between the oscillation of the airfoil and the oscillation of the freestream velocity, Φ, and the reduced amplitude, λ, were defined in Equations 2.5 and 2.6. It should be noted that because of the availability of experimental results for a

Table 7.1: Details of simulated cases ($Re = 1.35 \times 10^5$); values of all the parameters except those of freestream velocity oscillation are the same for both the numerical and the experimental setups [57].

Airfoil	NACA0012
Reynolds number, Re	$1.35{\times}10^5$
Inlet turbulent intensity	0.08%
Angle of attack oscillation (Equations 2.2 and 2.3)	
Reduced frequency, k	0.1
Mean angle of attack, α_{mean}	10°
Amplitude of oscillation, α_{amp}	15°
Freestream velocity oscillation (Equations 2.5 and 2.3)	
Reduced frequency, k	0.1
Reduced amplitude, λ	0.4,0.6,0.8
Phase difference of oscillations, Φ	$0, \frac{\pi}{4}, \frac{\pi}{2}, \frac{3\pi}{4}, \pi$

pitch oscillating condition [57] to validate the CFD results, the pitch oscillating parameters are consistent for all cases. For the numerical approach, the SST $k-\omega$ model coupled with a low-Reynolds number correction was applied for $Re \approx 10^5$, when the airfoil was under dynamic stall. In Section 4.4.2, the results of the current numerical simulation for sinusoidal pitch oscillation with a steady freestream have been validated by the existing experimental results of Lee and Gerontakos [57].

7.2 Pitching angle of attack with in-phase freestream velocity oscillation

For this case, the airfoil is sinusoidally pitch oscillating with

$$\alpha = 10 + 15\sin(2\pi f t) \quad [deg] \tag{7.1}$$

while a time-varying freestream velocity,

$$\frac{U(t)}{U_\infty} = 1 + 0.6\sin(2\pi f t) \tag{7.2}$$

is superimposed. The rest of the information can be found in Table 7.1. For this case, when the angle of attack increases, the freestream velocity accelerates and in the same manner,

at pitch down motion, the time varying freestream velocity decelerates. To see the dynamic effects of in-phase movement ($\Phi = 0$), all the results for this case are compared with the pitch oscillating case with a steady freestream condition, the SOS.

7.2.1 Aerodynamic loads

Figure 7.2.1 shows the aerodynamic loads for a pitch cycle for both the SOS and COS. The main interest in dynamic stall phenomena is the load augmentation compared to the static stall, which are summarized in Table 7.2.1. At points A and A' (prime ($'$) indicates the COS), the reversed flow at the trailing edge moves upstream. For the steady freestream velocity, the aerodynamic coefficients are increased slightly compared to the static stall case. At this point, for the SOS, the values from experimental and numerical results are very close showing that at upstroke the curves overlap as shown in Figure 4.6. For the unsteady freestream velocity, the lift coefficient is slightly higher at point A'. The lift coefficient increases with a constant slope until a Leading Edge Vortex (LEV) forms. The growing LEV increases the slope of the lift curves at point B and B'. Compared to the experimental results, the numerical simulation for the SOS advances the stall point around 1.5°. The maximum lift value is underpredicted by less than 4.5% showing this numerical simulation can predict dynamic stall with good accuracy. The in-phase unsteady freestream velocity advances the stall point (point C') about 1.2° with an increase in more than 2.68 lift coefficient units compared with point C. Drag coefficients start to rise dramatically after points A and A'. Compared to the static stall, drag increases for points C and C' are 0.96 and 2.12 units for the SOS and COS, respectively, showing the high impact of dynamic cases on the drag coefficients. After static stall (point SS), the drag coefficient increases, but after dynamic stall the drag coefficient drops significantly similar to the lift coefficient. There is a discrepancy between steady and unsteady freestream velocity during post stall. For the COS, after point C', another peak in aerodynamic loads is visible representing a very energetic leading edge vortex. More details are discussed in the next section. After points D and D', the first LEV at pitch down motion helps to recover part of the load coefficients leading to the first downstroke peak [57, 89, 129]. The same scenario as the first upstroke maximum peak occurs for the first downstroke maximum peak; that means, point E is advanced compared to that of the experimental results and point E' occurs earlier than point E. Lift and drag values for point E' are 1.85 and 0.85 units higher than point E. For both the SOS and COS, the flows are fully attached close to $\alpha = -5°$.

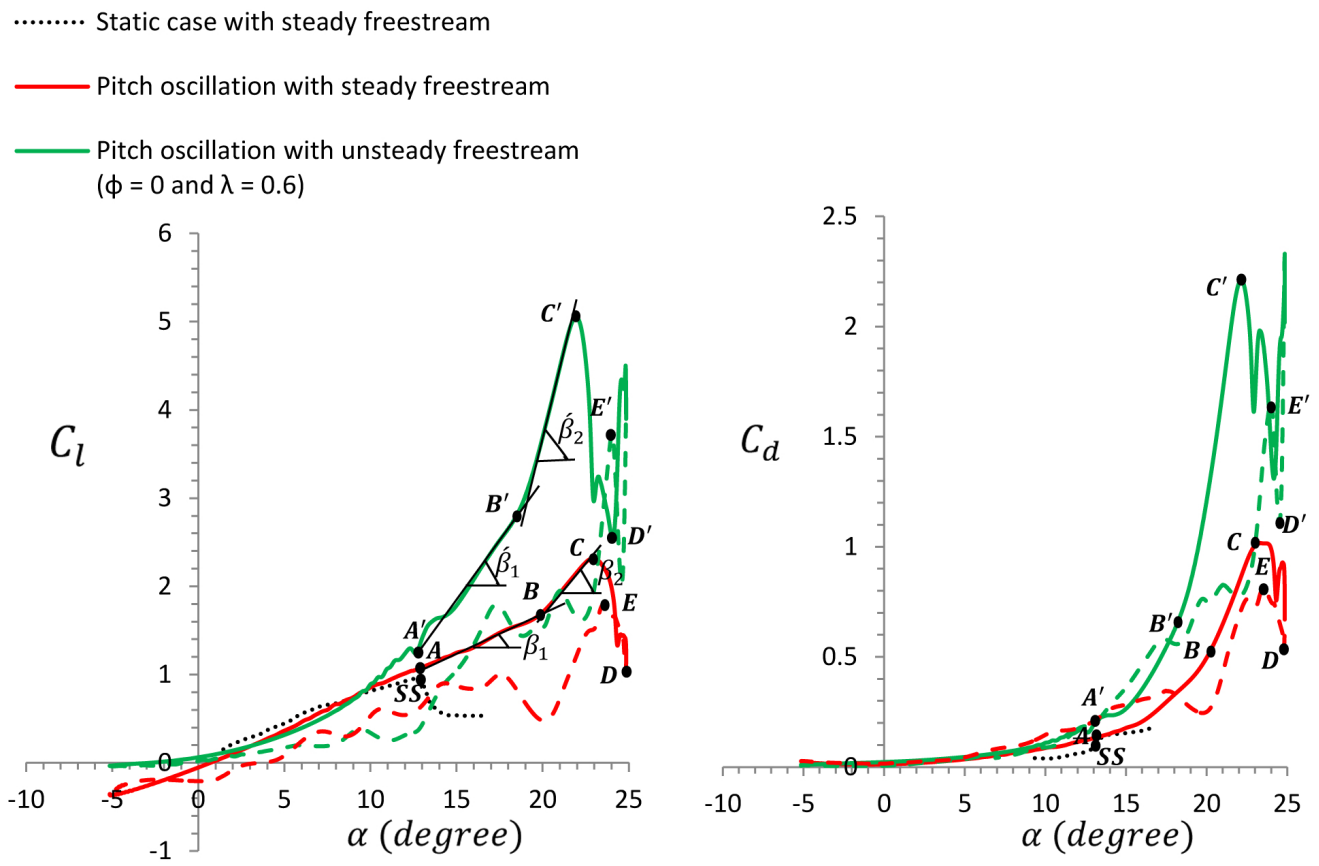

Figure 7.1: Comparison of loads; (A, A′) flow reversal, (B, B′) LEV, (C, C′) stall point, (C-D, C′-D′) full stall, (E, E′) maximum downstroke peak, and (SS) static stall. Solid lines: upstroke, and broken lines: downstroke. ′ indicates the COS.

Table 7.2: Summary of load augmentation ($Re = 1.35 \times 10^5$)

	SOS(Experimental method) [57]			SOS(Numerical method)				COS(Numerical method) (λ = 0.6 and Φ=0)			
	$\dot{\alpha}$	$\Delta C_l{}^*$	$\Delta C_d{}^{**}$	Point	α	$\triangle C_l{}^*$	$\triangle C_d{}^{**}$	Point	α	$\Delta C_l{}^*$	$\Delta C_d{}^{**}$
Flow reversal	12.9°	0.12	0.00	A	12.9°	0.12	0.06	A′	12.9°	0.50	0.13
LEV formation	21.9°	0.93	0.31	B	20.3°	0.85	0.46	B′	18.1°	1.77	0.58
First upstroke lift peak	24.7°	1.52	0.76	C	23.2°	1.40	0.96	C′	22.0°	4.08	2.12
First downstroke lift peak	21.8°	0.50	0.42	E	23.6°	0.95	0.75	E′	24.0°	2.80	1.60

$^*\triangle C_l = C_l - C_l(SS)$ where $C_L(SS)$ is 0.92 [57].
$^{**}\triangle C_d = C_d - C_d(SS)$ where $C_d(SS)$ is 0.0625 [57].

7.2.2 Flow structure

To interpret the behavior of the flow field under dynamic stall, the following figures have been prepared: Figure 7.2 for the TVR, Figure 7.3 for the pressure cefficient and Figure 7.4 for the non-dimensional vorticity field while Figures 7.2 and 7.3 are superimposed with streamlines. The TVR is defined in Equation 6.1. Based on the TVR field, Figure 7.2, the flow is considered as turbulent when the TVR is close to 100 [130]. The pressure coefficient is introduced in Equation 3.8 where P_∞ is the static pressure of the incoming flow at one chord ahead of the airfoil location.

Beginning with upstroke, the flow field undergoes different flow phenomena in a full cycle of pitch oscillation demonstrated in the following:

Attached flow and flow reversal: At a very low angle of attack, laminar flow is attached to the airfoil surface except in the small trailing edge region which was also seen in experiments [57]. The reversed flow at the trailing edge for both the SOS and COS starts moving upstream at $\alpha = 12.9°$. For the numerical simulation in Figure 7.5, a superimposition of velocity vectors, vorticity field and streamlines indicates the existence of the reversed flow at the trailing edge ($\alpha = 16° \uparrow$ for the SOS). Reversed flow at the trailing edge was also reported in the experimental results [57]. According to the experimental results, another characteristic is a roughly linearly increasing lift coefficient [57]. Figure 7.2.1 shows that the lift coefficient from the numerical simulation during $12.9° < \alpha < 20.3°$ has an almost constant slope β_1. For the COS, a constant lift slope β_1' during $12.9° < \alpha < 18.1°$ is also seen. The in-phase oscillating freestream is not changing the linear behavior of the lift augmentation, but the slope is much higher than that of the SOS, $\beta_1' > \beta_1$. Later in this section, there will be a discussion about the wake differences between these two cases.

Leading Edge Vortex (LEV) formation: Later a LEV forms, grows and moves toward the trailing edge. Based on the experimental results [57], LEV formation caused a sudden rise in aerodynamic loads. The same trend has been observed in the numerical loads (Figure 7.2.1). The slopes of the lift curve change suddenly after $\alpha = 20.3°$ (point B) and $\alpha = 18.1°$ (point B') for the SOS and COS, respectively. LEV formations are shown in Figures 7.2, 7.3 and 7.4. For the SOS, the LEV length is 28% of the chord length, twice the initial LEV length from experimental results. A LEV, a very low pressure vortex, enriches the strength of circulation resulting in an overshoot in the lift coefficient, shown in Figure 7.2.1. For the COS, an accelerating freestream velocity results in the advancement of point B' by 2.2° compared to that of the SOS (point B) and increases the strength of the LEV causing higher aerodynamic loads before stall. After the LEV generation, the lift curve rises almost linearly with an increased slope $\beta_2 > \beta_1$ and $\beta_2' > \beta_1'$ for the SOS and COS,

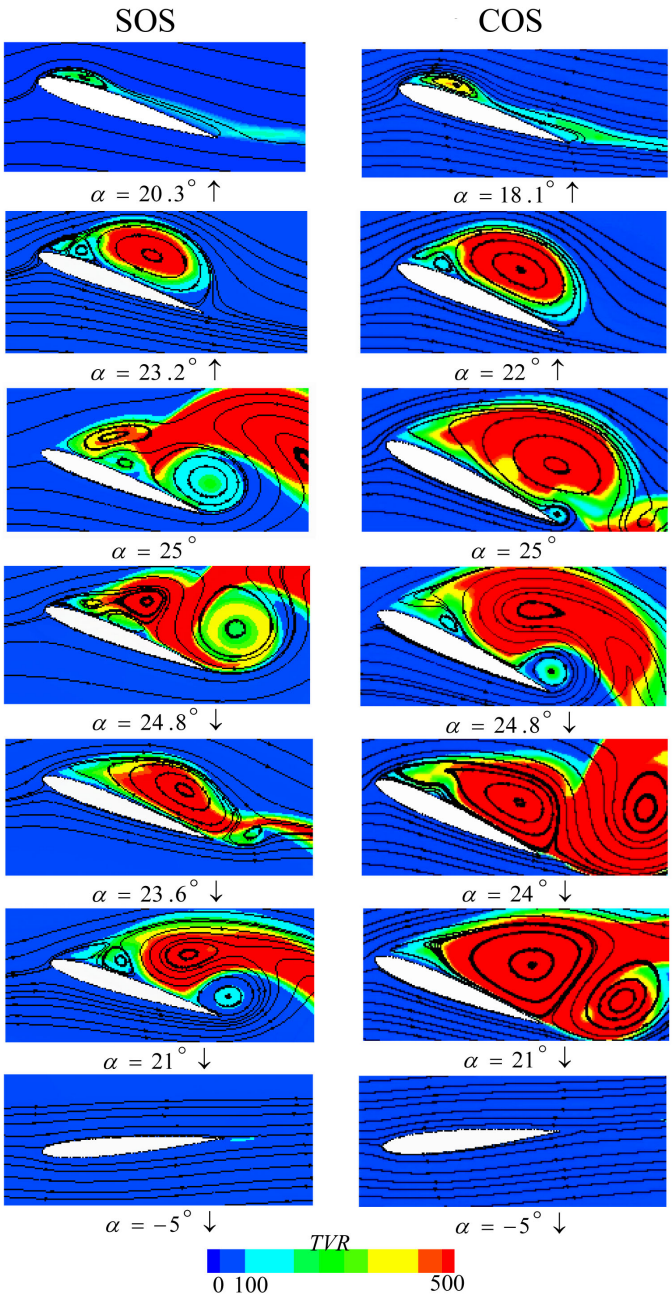

Figure 7.2: Turbulent viscosity ratio field superimposed with flow streamlines for the SOS and COS (λ= 0.6 and Φ=0 for the COS).

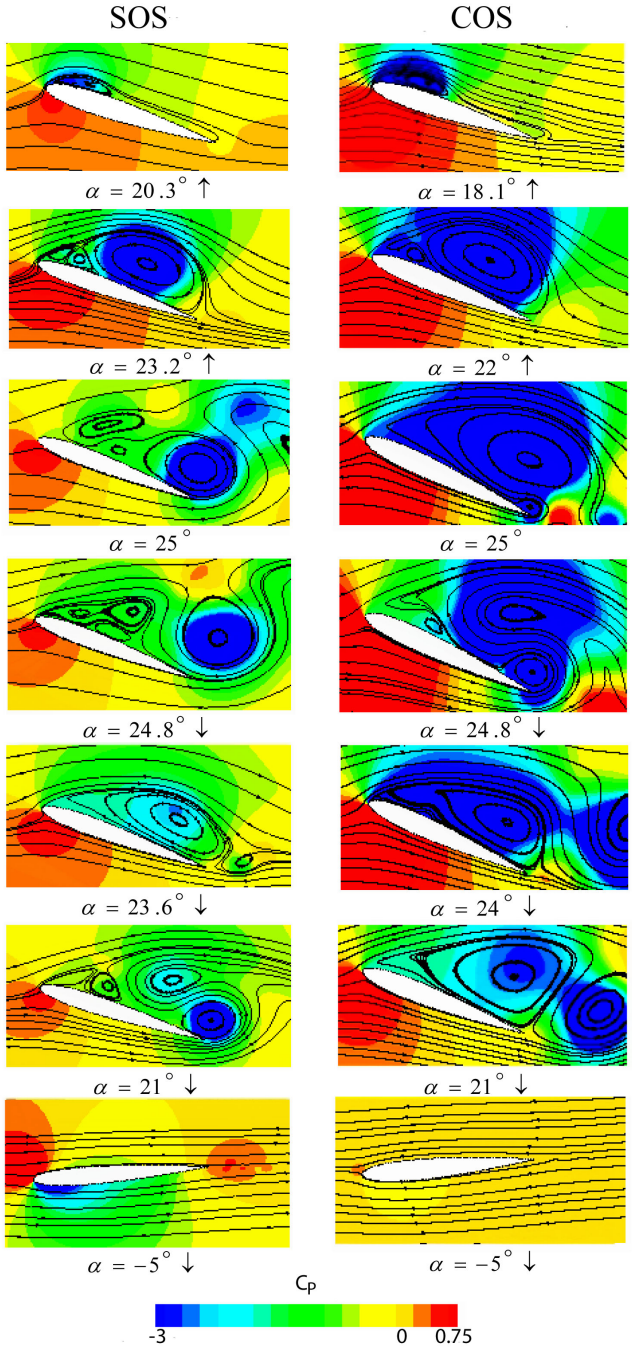

Figure 7.3: Pressure coefficient field superimposed with flow streamlines for the SOS and COS ($\lambda = 0.6$ and Φ=0 for the COS).

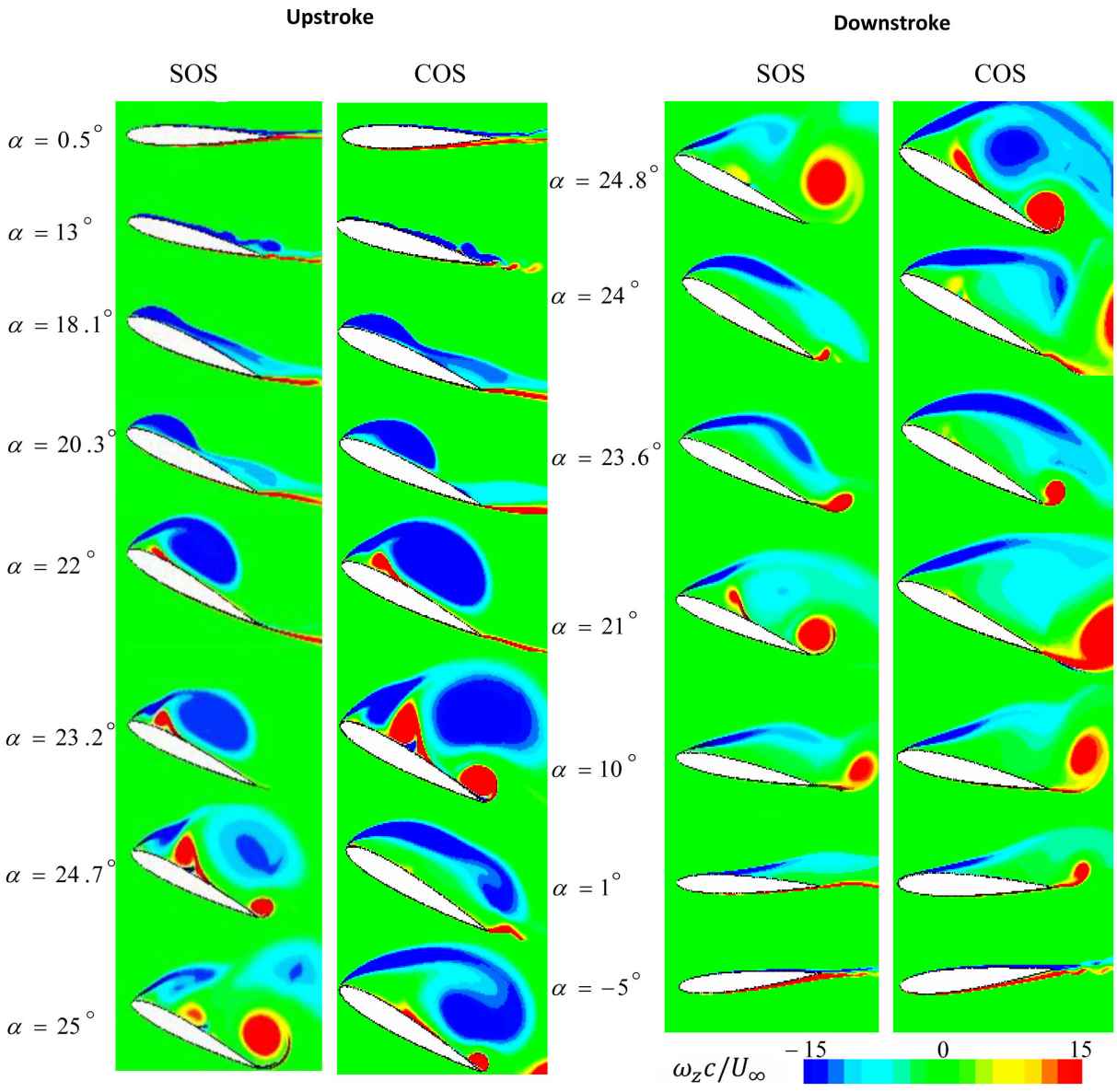

Figure 7.4: Instantaneous vorticity field for the SOS and COS ($\lambda = 0.6$ and Φ=0 for the COS).

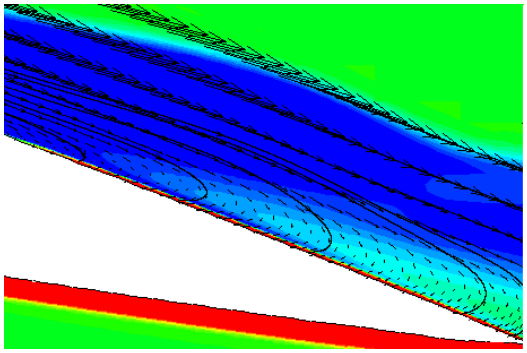

Figure 7.5: Close up view of the flow reversal at $\alpha = 16^o \uparrow$ for the SOS; the reversed flow visualized by velocity vectors and streamlines superimposed by the vorticity field which agrees with Lee and Gerontakos [57], for legend see Figure 7.4.

respectively, while $\beta_2' > \beta_2$ (Figure 7.2.1).

Trailing edge vortex (TEV): A counter-clockwise rotating vortex which is another source of circulation exists to satisfy conservation of circulation. The difference in vortical structures can be visually enhanced if the vorticity fields are simply subtracted [137]. Figure 7.6 shows this instantaneous subtraction ($\omega_{z,\,COS} - \omega_{z,\,SOS}$). Before dynamic stall, the TEV mostly appears in vortex sheet form as shown in Figure 7.6, for $\alpha = 10.5^o$ (before LEV formation), $\alpha = 18^o$ and $\alpha = 20.3^o$ (close to stall). After the airfoil passes the mean angle of attack (10^o), where the velocities of the SOS and COS are the same, the difference between the aerodynamic loads between the two cases increases. At $\alpha = 10.5^o$, aerodynamic loads from the COS are slightly higher than those of the SOS. Although there is no sign of the LEV, the size of the TEV and the way that it is convected downstream can be one reason for the load difference. The TEV from the COS appears as a longer vortex sheet. The longer vortex sheet from the COS follows Katz and Plotkin [51] in that a longer vortex sheet of small vortices is favorable for a lift increase. At higher angles, the sheet of vortices are longer and their differences are more visible. Wong et al. [137, 136] also showed that the trailing edge vorticity variation affects the force history. For the COS, the velocity during upstroke is accelerating. By considering just the longitudinal freestream velocity after the mean angle of attack, the distance that a particle moves from the trailing edge under an unsteady freestream ($\int U(t)dt$) is more than that of the steady freestream ($U_{mean}\Delta t$). If the particles travel faster, the vortex sheet extends further to form a longer vortex sheet. The longer vortex sheet reduces the lift reduction caused by the TEV.

Secondary LEV formation: During the first LEV growth, a counter-clockwise vortex is generated close to the leading edge, shown at $\alpha = 22^\circ$ in Figure 7.4. Beside it, a clockwise

LEV is formed later to form a pair of LEV, shown at $\alpha = 23.2°$. Gradually, the clockwise LEV is growing while the counter-clockwise one is moving rearward and disappearing. This complicated structure indicates an unstable boundary layer during the second LEV formation [129].

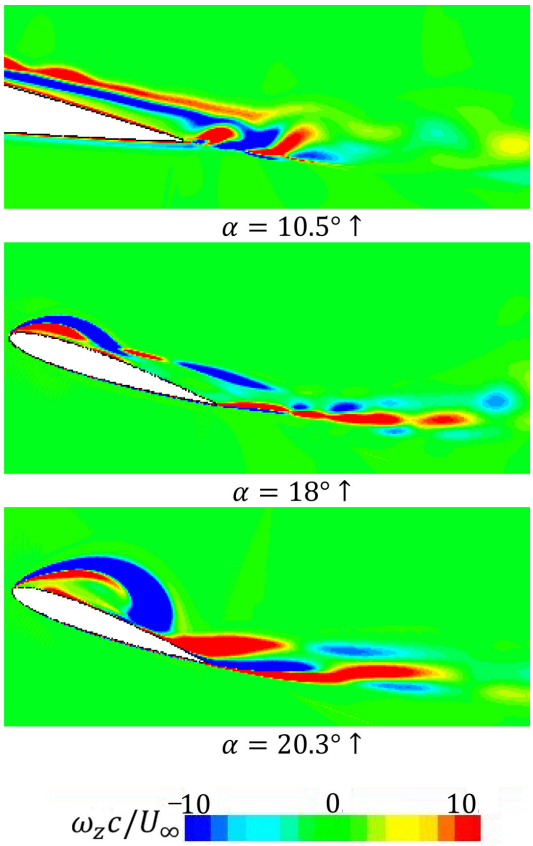

Figure 7.6: Instantaneous vorticity field subtraction between the COS ($\lambda = 0.6$ and Φ=0) and SOS before dynamic stall.

Stall: As LEVs are growing, the first low pressure LEV occupies more of the suction surface area resulting in an increase of the normal force on the pressure surface. Dynamic stall occurs when the lift reaches its maximum value and based on the vorticity field, dynamic stall occurs when the outer surface of the LEV meets the trailing edge. Figure 7.7 shows a close up view of the vortical field of dynamic stall overlaid with the streamlines for the COS. For all cases in this study, the outer surface of the LEV streamlines meets the trailing edge also seen in the vorticity field. Streamlines in Figures 7.2 and 7.3 show

the LEV for the SOS at $\alpha = 23.2°$ and for the COS at $\alpha = 22°$. At this point the airfoil is stalled and a high TVR dominates the LEV as shown in Figure 7.2. In Figure 7.3, for the COS, very low pressure on the suction side and very high pressure on the pressure side compared to the steady freestream velocity indicates high loading on the airfoil.

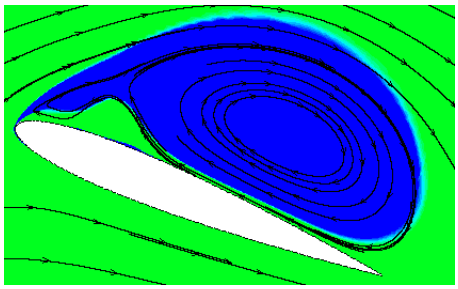

Figure 7.7: Close up view of dynamic stall vorticity field (negative values) overlaid with streamlines for the in-phase COS; for legend see Figure 7.4.

LEV shedding: After stall, the LEV keeps growing in size and then leaves the suction surface. In Figure 7.4, the first separated LEV in the wake is visible at $\alpha = 24.7°$ and $\alpha = 23.2°$ for the SOS and COS, respectively. During the shedding process, a large area on the suction surface has high TVR values especially for the COS seen in Figure 7.2.

Full stall TEV: After dynamic stall, the counter-clockwise vortex gradually rolls up and finally sheds to the wake. Figure 7.4 shows the growing and shedding of the first negative roll up vortex after $\alpha = 23.2° \uparrow$ to $\alpha = 24.8° \downarrow$ for the SOS. For the COS, the process of formation to shedding of the first TEV occurs in 2°, after $\alpha = 22° \uparrow$ to $\alpha = 24° \uparrow$. The developed TEV has a TVR value (Figure 7.2) greater than 100, a very low static pressure level (Figure 7.3) and high vorticity magnitude (Figure 7.4). The TEV has been shed to the wake before the next LEV covers the whole suction surface and then the next TEV is initialized.

Secondary upstroke LEV growth and shedding: The boundary layer of the COS feeds a secondary LEV with high vorticity. Therefore, this very low pressure secondary LEV grows in size rapidly and then creates the second load peak at $\alpha = 24.7° \uparrow$ where this secondary LEV covers the whole suction surface, shown in Figure 7.4, and then it is shed to the wake, $\alpha = 25°$ in Figure 7.4. For the SOS, the secondary LEV is shed at downstroke. For the rest of the cases, the location of the second maximum lift peak related to the secondary LEV will be discussed in sections 7.3 and 7.4.

First downstroke LEV growth and shedding: Gradually, at downstroke, the negative vortex of the leading edge vortex pair occupies the suction surface. Similar to

the first LEV, increasing the size of the vortex recovers the lift force to create a maximum peak in downstroke. For the SOS, at $\alpha = 23.6° \downarrow$, the vortex reaches the trailing edge and then starts to shed. For the COS, the maximum lift occurs at $\alpha = 24° \downarrow$. Figures 7.2.1 and 7.4 show that the first downstroke LEV is not as strong as the upstroke one and that the aerodynamic coefficients do not recover to the values at the stall point.

Small vortices: Figure 7.2.1 shows small lift peaks after the secondary LEV for both the SOS and COS. These are the result of small vortices which have very low circulations. Figure 7.4 shows some of these small vortices after $\alpha = 23.6° \downarrow$, and $\alpha = 24° \downarrow$ for the SOS and COS.

Reattached flow: At $\alpha = 1° \downarrow$ for both the SOS and COS, all small vortices have disappeared, but the flows are not fully attached at the trailing edge which agrees with the experimental results [57].

7.2.3 Circulation and pinch-off process

Figure 7.8 compares the dimensionless circulation for the first LEV and the following TEV for the SOS and COS. For the COS, the circulation of the LEV has a greater slope and reaches the maximum value sooner in comparison to that of the steady case. The accelerating freestream speeds feeding of the LEV in the boundary layer. Dynamic stall is advanced for the COS about 1.2^o compared to the SOS while the circulation is 1.5 times greater. In Figure 7.8, the phase delay ($\Delta\alpha$) shows that the maximum LEV circulation occurs later than the peak lift distribution (dynamic stall). According to Figure 7.8, this phase delay ($\Delta\alpha \approx 1.4^o$) cannot be ignored and the TEV is formed after dynamic stall. Figure 7.9 shows the TEV clearly after dynamic stall and before peak circulation for the SOS. This means that after dynamic stall, the boundary layer keeps feeding the LEV where $\frac{\Delta\Gamma_{LEV}}{U_\infty c} = 0.45$ and 0.7 for the SOS and COS, respectively and at the same time the TEV is growing and rolling up where $\frac{\Delta\Gamma_{TEV}}{U_\infty c} = 2$ and 2.8 for the SOS and COS, respectively. Since the TEV has a negative effect on lift augmentation, an increase in the TEV circulation contributes to the lift reduction despite the LEV growth. When the LEV pinches off, the boundary layer stops feeding it and this location is the maximum circulation. The overall trends of the TEV circulation curves are similar in Figure 7.8. The TEV circulation curve for the SOS, compared to that of the COS, is shifted due to the dynamic stall delay and has lower circulation similar to the LEV circulation cases above. This indicates that the strengths of the LEV and the TEV are strongly connected which agrees with the results of Chapter 5.

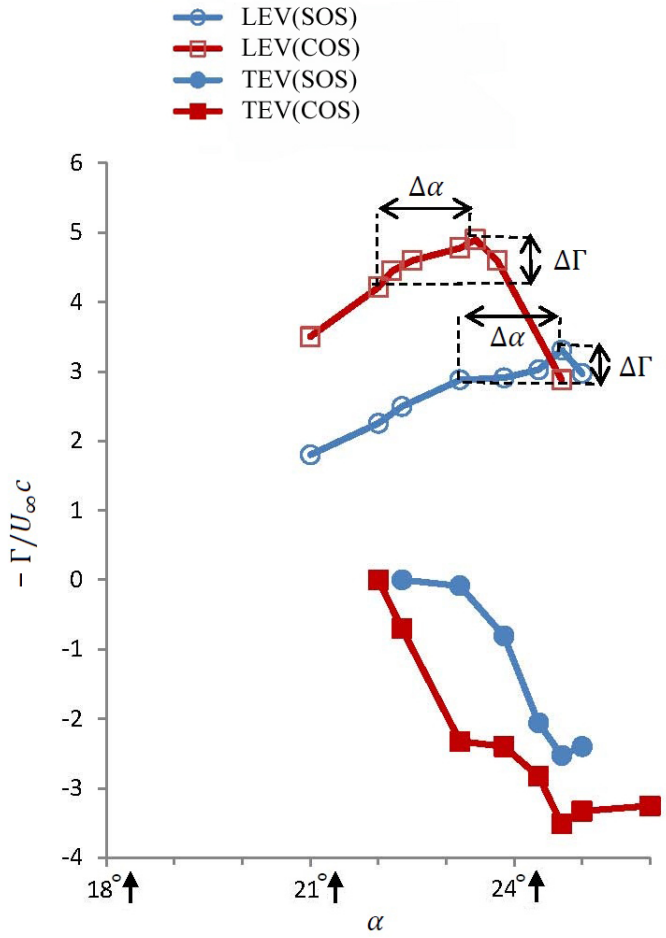

Figure 7.8: LEV and TEV dimensionless circulation for the SOS and COS ($\lambda = 0.6$ and Φ=0). Lines are for visualization only. $\Delta\alpha$: Phase delay between the maximum lift (dynamic stall) and the maximum circulation.

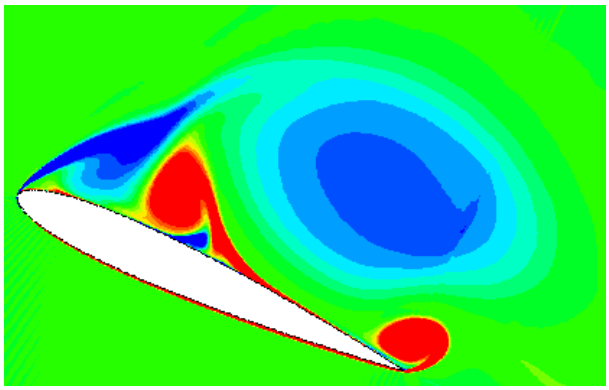

Figure 7.9: TEV formation after dynamic stall and before LEV separation at $\alpha = 24.4^o \uparrow$ for the SOS; for legend see Figure 7.4.

Table 7.3: Summary of critical angles of attack ($Re = 1.35 \times 10^5$).

COS		First upstroke Lift peak	Second upstroke lift peak	First downstroke lift peak
λ	Φ			
0.4	0	22.3°	24.8°	22.9°
0.6	0	22.0°	24.4°	24.0°
0.8	0	21.7°	24.0°	24.5°
0.6	$\pi/4$	21.0°	24.0°	24.1°
0.6	$\pi/2$	20.2°	24.3°	21.0°
0.6	$3\pi/4$	22.4°	-	24.0°
0.6	π	24.6°	-	20.3°

7.3 Reduced amplitude, λ, influences

Three different reduced amplitude (λ = 0.4, 0.6 and 0.8) cases were studied. For this section, Φ=0 was chosen while the rest of the information is the same as in Table 7.1. A comparison of aerodynamic coefficients in Figure 7.10 shows that increasing 0.2 units of λ advances the stall point slightly (Table 7.3) and increases the lift and drag coefficients almost 1 and 0.5 units, respectively, because the velocity of the freestream during dynamic stall is higher. Aerodynamic load enrichment with increasing λ has also been reported by Leishman [58]. At low angles of incidence, there is no significant difference. The overall form of the curves is almost the same for these cases and the secondary lift peak at upstroke from the secondary LEV exists for all three cases. The behavior of the boundary layer in advancing the secondary peak will be discussed in the next section.

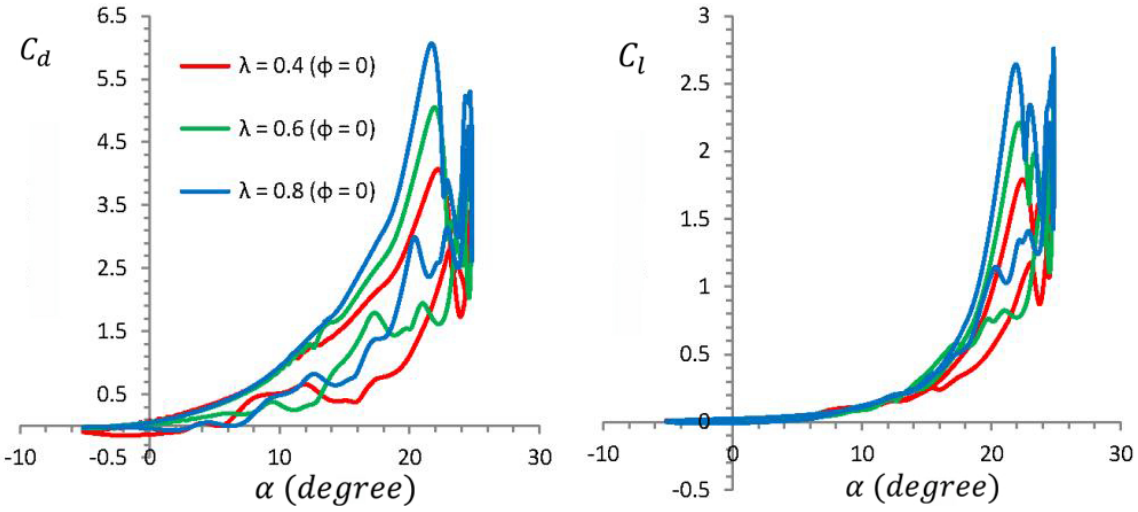

Figure 7.10: Aerodynamic loads for $\lambda = 0.4$, 0.6 and 0.8 with Φ=0.

7.4 Phase difference of oscillation, Φ, impacts

The effects of the phase difference between the oscillation of the airfoil and oscillation of the freestream velocity on aerodynamic loads are now considered. For this section, $\lambda = 0.6$ was chosen and the rest of the information is the same as in Table 7.1. Figure 7.11 shows lift and drag coefficients for $\Phi = 0, \frac{\pi}{4}, \frac{\pi}{2}, \frac{3\pi}{4}$ and π. The results show the significant impact of the Φ parameter on loads. For $\Phi \leq \frac{\pi}{2}$, the loads are significantly high, the first maximum peak moves forward and the second LEV shedding occurs at upstroke. More details about the critical angles of attack are provided in Table 7.3. For $\Phi > \frac{\pi}{2}$, the second LEV shedding is postponed to the downstroke (for $\Phi = \frac{3\pi}{4}$, it is completely at downstroke) which is similar to that of pure pitch oscillation and is consistent with the results of Favier et al. [29] from their experimental facilities. For $\Phi > \frac{\pi}{2}$, although separation of the first LEV is postponed, the LEV cannot increase the aerodynamic loads. For the $\Phi = \pi$ case, the aerodynamic loads during the dynamic stall process ($\alpha > 15^\circ \uparrow$) are much smaller than those of the pitch oscillating case with uniform freestream velocity; that means, dynamic loads are damped significantly.

The behavior of the boundary layer based on vortex growth time from the LEV formation to dynamic stall is shown in Figure 7.12 which reveals two different trends. In this figure, the time is made dimensionless by the frequency of the oscillations, f. The time difference between curves for each Φ shows the vortex growth time. As Φ increases from the zero value to $\Phi = \frac{\pi}{2}$, the vortex growth time is decreasing continually, but for $\Phi > \frac{\pi}{2}$,

the trend is reversed and vortex growth time increases. Thus, the chart is divided in two regions. In the first region, as Φ increases from the zero value, the maximum freestream velocity, U_{max}, shifts forward slightly before the dynamic stall angle which affects the force history before stall while the freestream velocity during dynamic stall (DS), U_{DS}, is greater than U_{mean}. If dynamic stall happens sooner, it becomes closer to U_{max}, which is suitable for load augmentation and then the vortex growth time is decreased. Moreover, in this region, all the secondary lift peaks occur during upstroke. For a SOS, the second lift peak can be advanced to an upstroke location when the reduced frequency is decreased, Chapter 5. Under low reduced frequency, the aerodynamic loads are decreased, but for the COS the loads are significantly increased when the second peak is located during upstroke $0 \leq \Phi \leq \frac{\pi}{2}$. It is concluded that in the first region, the boundary layer does not follow the behavior of pitch oscillating airfoils as mentioned in [68]. For the second region, $\Phi > \frac{\pi}{2}$, U_{DS} is lower than U_{mean} and U_{max} occurs away from dynamic stall at very low angles. In this range, the boundary layer delays dynamic stall to increase the loads. As a result, vortex growth time is increased. It should be mentioned that because U_{DS} is very low, the overall load cannot be increased in this range. In these two regions, the boundary layer behaves differently and then the previous assumption of increasing the vortex growth time for load augmentation cannot always be correct.

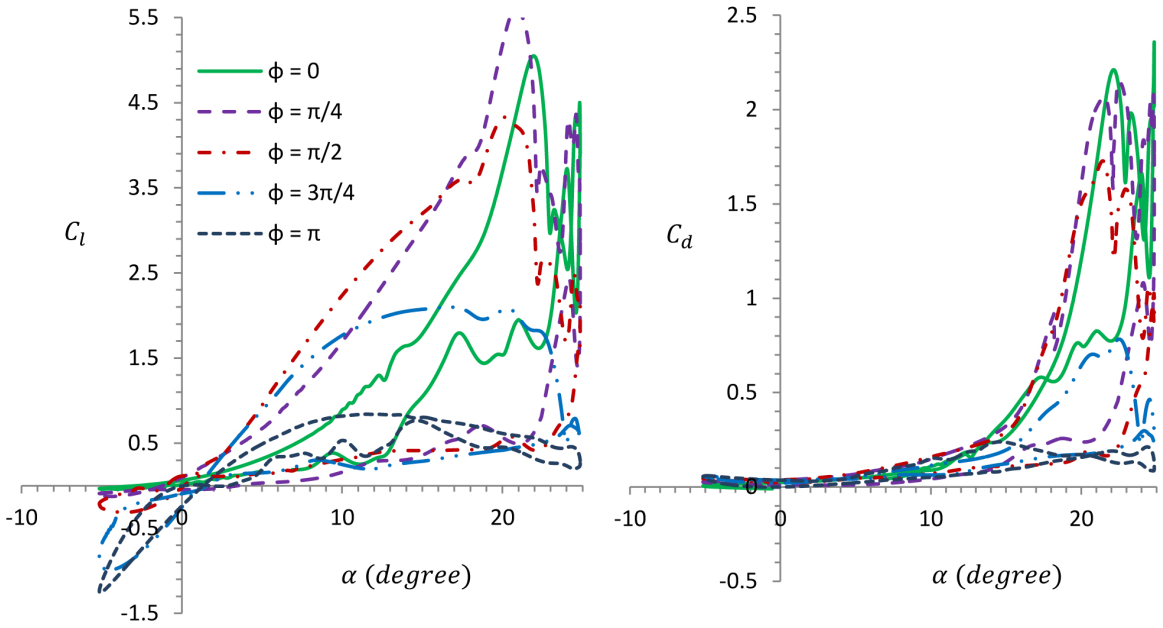

Figure 7.11: Aerodynamic loads for $\Phi = 0, \frac{\pi}{4}, \frac{\pi}{2}, \frac{3\pi}{4}$ and π with $\lambda = 0.6$.

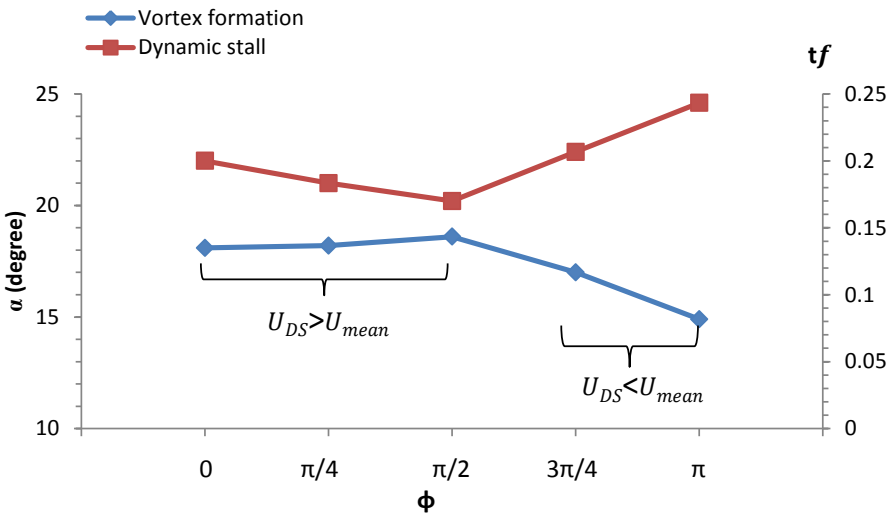

Figure 7.12: Angles and times of LEV formation and dynamic stall versus Φ during upstroke ($\lambda = 0.6$); time difference between two curves for each Φ shows the vortex growth time; lines are for visualization purposes.

7.5 Summary

A pitch oscillating NACA0012 airfoil was simulated numerically to understand the problem of a lifting object under dynamic stall associated with an unsteady freestream velocity at low Reynolds number, $Re \approx 10^5$. The cyclical integral forces and flow structures including LEV and TEV initiation, propagation and shedding agreed well qualitatively and quantitatively with those existing in the literature.

Increases in loads in the dynamic case are challenging from design and control points of view. From the results of this study, the aerodynamic loads show that for a pure pitch oscillating airfoil under a uniform freestream velocity, the stall point lift coefficient is 2.5 times greater than that of the static airfoil. The lift augmentation is more significant when the pitch oscillating airfoil is combined with an oscillating freestream with $0 \leq \Phi \leq \frac{\pi}{2}$. The in-phase oscillations, $\Phi = 0$, showed 5.4 times greater lift than that of the static freestream. This value was amplified when the reduced amplitude was increased. The low pressure LEV caused a very high pressure difference between the pressure surface and the suction surface when the flow was not attached indicating that very high loads are applied to the airfoil for the $\Phi = 0$ case. As a future study, three dimensional modeling of the flow field will reveal more details of the dynamic stall phenomena. Comparing

the steady and in-phase unsteady freestream cases showed that high LEV circulation was favorable for high lift values and the coupled strength of the LEV and TEV resulted in higher circulation for the TEV. Vortex circulation revealed a significant phase delay of LEV pinch-off (maximum circulation) after dynamic stall (maximum lift). During this phase lag, the TEV was growing, rolling up and decreased the lift values although the boundary layer was feeding the LEV. The contribution of the TEV on lift values was more visible when it appeared like a vortex sheet before dynamic stall. An accelerating freestream during dynamic stall speeds the vortex sheet expansion in the wake. The resultant longer vortex sheet for in-phase unsteady freestream increased lift significantly before stall since the longer trailing edge vortex sheet was favorable for increasing lift values.

The high phase difference, $\Phi > \frac{\pi}{2}$, decreases the aerodynamic loads. For the $\Phi = \pi$ case, the lift and drag loads are almost 3 and 5 times, respectively, lower than those of the SOS. The dynamic stall loads for this case were even lower than those of static stall which is opposite to the concept of dynamic stall which usually augments loads.

The location of the maximum freestream velocity affects the force history before stall. Despite variation in the loads, decreasing Φ from $\Phi = \frac{\pi}{2}$ and increasing Φ from $\Phi = \frac{\pi}{2}$ have an important common characteristic: they both increase the vortex growth time. This result reveals an important insight that increasing vortex growth time can either increase or decrease the dynamic stall loads.

Chapter 8

On interactions of angle and freestream oscillations (S809 airfoil, $Re = 10^6$)

Based on the results of Chapter 7, the unsteady freestream showed significant impact on the flow field of the oscillating angle of attack. The current chapter is organized to reveal the contribution of the airfoil type and the Reynolds number on the angle and freestream oscillations while $-\pi \leq \Phi \leq \pi$ is covered. For these purposes, a CFD simulation of a pitch oscillating S809 airfoil subjected to an oscillating incident velocity with $Re = 10^6$ is considered. The effects of the interacting oscillating systems when the airfoil undergoes dynamic stall will be discussed in relation to the vortical structure and resultant aerodynamic loads.

8.1 Simulated cases

The S809 airfoil is oscillating sinusoidally. The resultant angle of attack is based on Equation 2.2, while the incident velocity variation can be described as Equation 2.5.

The descriptions of each parameter and their values are described in Table 8.1. For the steady incident velocity, a uniform freestream (U_∞) is considered and for the unsteady freestream velocity, $U_{mean} = U_\infty$. Both SOS and COS have the same frequency of oscillation, f, with the same reduced frequency (k), Equation 2.3. In order to understand the effect of the unsteady incident velocity, different phase differences, $\Phi = 0$, $\pm\frac{\pi}{4}$, $\pm\frac{\pi}{2}$, $\pm\frac{3\pi}{4}$ and π, were selected. Other constant oscillating system parameters, shown in Table 8.1, were chosen since they produce a strong LEV and TEV (or LEV-TEV pair) during dynamic stall as well as the experimental results of pure pitching motion with constant

Table 8.1: Details of simulated cases ($Re = 10^6$)

Parameters		**value**
Chord length	c	0.45m
Reynolds number	Re	10^6
Mach number	Ma	0.1
Reduced frequency	k	0.077
Mean angle of attack	α_{mean}	14°
Amplitude of oscillation	α_{amp}	10°
Reduced amplitude	λ	0.6
Phase difference of oscillations	Φ	$0, \pm\frac{\pi}{4}, \pm\frac{\pi}{2}, \pm\frac{3\pi}{4}, \pi$

velocity exist in the literature [93]. In Section 4.4.2, the results of the simulation for the pitch oscillating case under steady freestream have been validated with the experimental results of Ramsay et al. [93] considering the same parameter values.

8.2 COS versus SOS

Vortical structure and aerodynamic loads provide further insight into the behavior of the airfoil boundary layer under different circumstances. The temporal evolution of vortices based on the angle of attack has been plotted over one cycle in Figure 8.2 for $-\pi \leq \Phi \leq \pi$ of the COS versus the SOS. The vorticity, ω_z, is made dimensionless with chord length and U_{mean} (note that for the SOS $U_{mean} = U_\infty$). The plots start from the upstroke. After the dynamic airfoil passes its static stall angle of attack ($\alpha_{static\,stall} = 15.23°$ [113]), a small LEV with a negative voriticity value is formed and gradually grows. In Figure 8.2, at an angle of attack of 22.5° ↑, a LEV is visible for all cases. When the first LEV during upstroke meets the trailing edge, dynamic stall occurs and then a TEV with a positive vorticity value forms and gradually is growing and rolling up. In Figure 8.2, a TEV (the first TEV after dynamic stall except for $\Phi = 0$, $\pm\pi/4$ and $\pi/2$ cases showing the second one) close to the trailing edge is visible for all cases at an angle of attack of 24°. The LEV separates from the suction surface with a phase delay after DS. For the SOS, one LEV is fully developed in the upstroke and the second LEV meets the trailing edge of the airfoil during downstroke. Aerodynamic load comparisons between the SOS and COS are presented in Figure 8.2 for in-phase and different out-of-phase oscillating cases. Details regarding critical angles of attack are indicated in Table 8.2. Comparing the SOS and COS results shows significant discrepancies and they are discussed in the following section.

One of the important dynamic stall characteristics is significant load augmentation. For the SOS, the dynamic stall load values are $C_{lDS} = 2.14$ and $C_{dDS} = 1.09$. For COS, changing Φ results in variable dynamic stall loads. Figure 8.3 shows the dynamic stall load difference ($\Delta load_{DS}$) compared to the constant values from the SOS:

$$\Delta load_{DS} = load_{DS}(COS) - load_{DS}(SOS), \tag{8.1}$$

where load can be either lift coefficient, C_l or drag coefficient, C_d. This figure shows that the lift coefficients can increase close to three units, for $\Phi = \pi/4$, or decline almost two units, for $\Phi = \pi$ and $-3\pi/4$, compared to those of the SOS; they are even lower than the static stall value [113]. The drag values can also be almost 1.5 units higher or 1 unit lower than those of the SOS.

The loads are decreasing as the magnitude of Φ increases (Figure 8.2) and the upstroke and downstroke curves are switched between $\Phi < 0$ and $\Phi > 0$; that means the downstroke aerodynamic loads are higher than upstroke ones for $\Phi < 0$ which are different from the SOS load loops.

For the SOS, the dynamic stall load value is the maximum (max) value in the whole cycle, $C_{lDS} = C_{lmax}$ and $C_{dDS} = C_{dmax}$. On the contrary, for the COS, the maximum load may differ from the dynamic stall load; see Table 8.2 for dynamic stall angles as well as maximum load angles. Figure 8.3 also shows the maximum load difference ($\Delta load_{max}$) compared to the constant values from the SOS:

$$\Delta load_{max} = load_{max}(COS) - load_{DS\ or\ max}(SOS). \tag{8.2}$$

For out of phase oscillations, the dynamic stall loads are not always the maximum loads in each cycle. The maximum values (for $\Phi = -\pi/2$, $\pm 3\pi/4$ and π) can appear even at low angles, as shown in Figure 8.2.

After TEV pinch off, the LEV-TEV vortex pair is shed to the wake. The counter-rotating LEV-TEV vortex pair convect downstream while another pair is ready to develop. Typical behavior of LEV generation for the SOS is that the first LEV has the maximum vorticity. On the contrary, for some cases such as $\Phi = -\pi/4$, shown in Figure 8.2 during downstroke, the level of vorticity for the first downstroke vortex pair is higher than that of the first upstroke pair.

The TEV before LEV formation appears as a vortex sheet visible in Figure 8.2 at $\alpha = 12^\circ \uparrow$, but for $\Phi \leqq -\pi/4$, the length of the vortex sheet is very short.

For the SOS, one load peak is observed during upstroke, but for low Φ values, e.g. $\Phi = 0$, the second load peak is also at upstroke.

To explain these discrepancies, the range of Φ is divided into some sub-domains based on the freestream acceleration during dynamic stall (a_{DS}) and the freestream velocity during dynamic stall (U_{DS}).

8.3 Effects of freestream velocity and acceleration during dynamic stall

In Figure 8.4, the angle of attack oscillation and streamwise freestream velocity oscillations with different Φ values are presented versus time (t), made dimensionless by the frequency of the oscillation (f). A part of the angle of attack oscillation curve is shown as the dynamic stall domain, $22° \uparrow \quad < \alpha < 24° \uparrow$, where for all cases, dynamic stall occurs inside this domain (see Table 8.2). During dynamic stall, located inside the dynamic stall domain, the freestream is accelerating ($a_{DS} > 0$) for $\Phi \leq 0$, and for the rest of the domain, the freestream velocities are decelerating ($a_{DS} < 0$). The freestream velocity during dynamic stall is higher than the mean velocity ($U_{DS} > U_{mean}$) when $-\pi/2 < \Phi \leq \pi/2$ and for the rest $U_{DS} < U_{mean}$. The freestream acceleration during dynamic stall (a_{DS}) and the freestream velocity during dynamic stall (U_{DS}) will be used as two indicators for dividing the Φ domain into four ranges. They are:

a) $U_{DS} > U_{mean}$ and $a_{DS} < 0$:
This subdomain occurs for $0 < \Phi \leq \pi/2$. Since the freestream is decelerating during dynamic stall, the maximum velocity occurs before dynamic stall and this causes a significant dynamic stall load augmentation. For $\Phi = \pi/4$, since the angle of maximum incident velocity, 21°, is close to the angle of dynamic stall, 22.7°, the angle where maximum load occurs is the same as that of dynamic stall, 22.7° (Table 8.2). Thus dynamic stall loads for $\Phi = \pi/4$ have the highest load values in the entire Φ domain and are more than double those of the SOS. For $\Phi = \pi/2$, Table 8.2 indicates that a maximum incident velocity occurs 8.3° sooner than dynamic stall. Based on this angle difference, the maximum C_l advances 6° compared to the dynamic stall angle, but the maximum drag angle is still very close to the dynamic stall angle (Figure 8.2f). Figure 8.3 also shows that at $\Phi = \pi/2$ the maximum and the dynamic stall curves for the drag coefficient overlap each other, but they differ for the lift coefficient while the aerodynamic loads are still high compared to those of the SOS. Thus in this subdomain, the location of the maximum lift value depends on the location of U_{max}, but the location of the maximum drag value is coupled with the location of the dynamic stall angle.

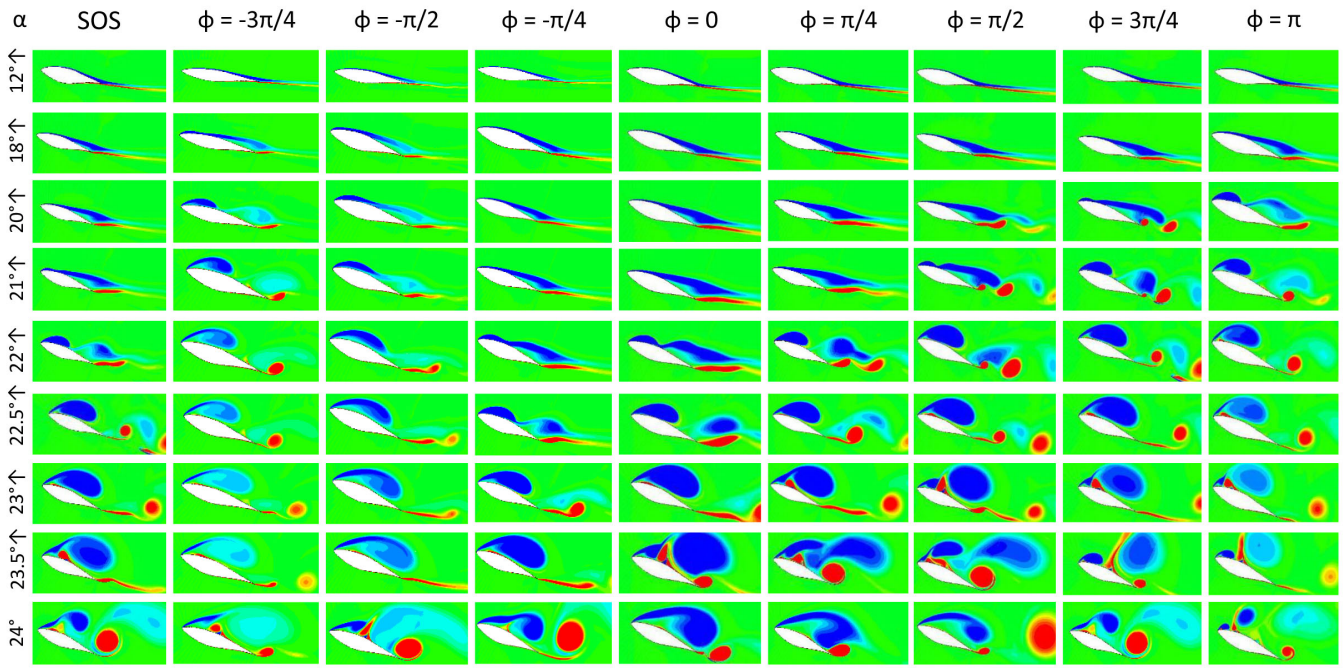
α
SOS
ϕ = -3π/4
ϕ = -π/2
ϕ = -π/4
ϕ = 0
ϕ = π/4
ϕ = π/2
ϕ = 3π/4
ϕ = π
12°↑
18°↑
20°↑
21°↑
22°↑
22.5°↑
23°↑
23.5°↑
24°

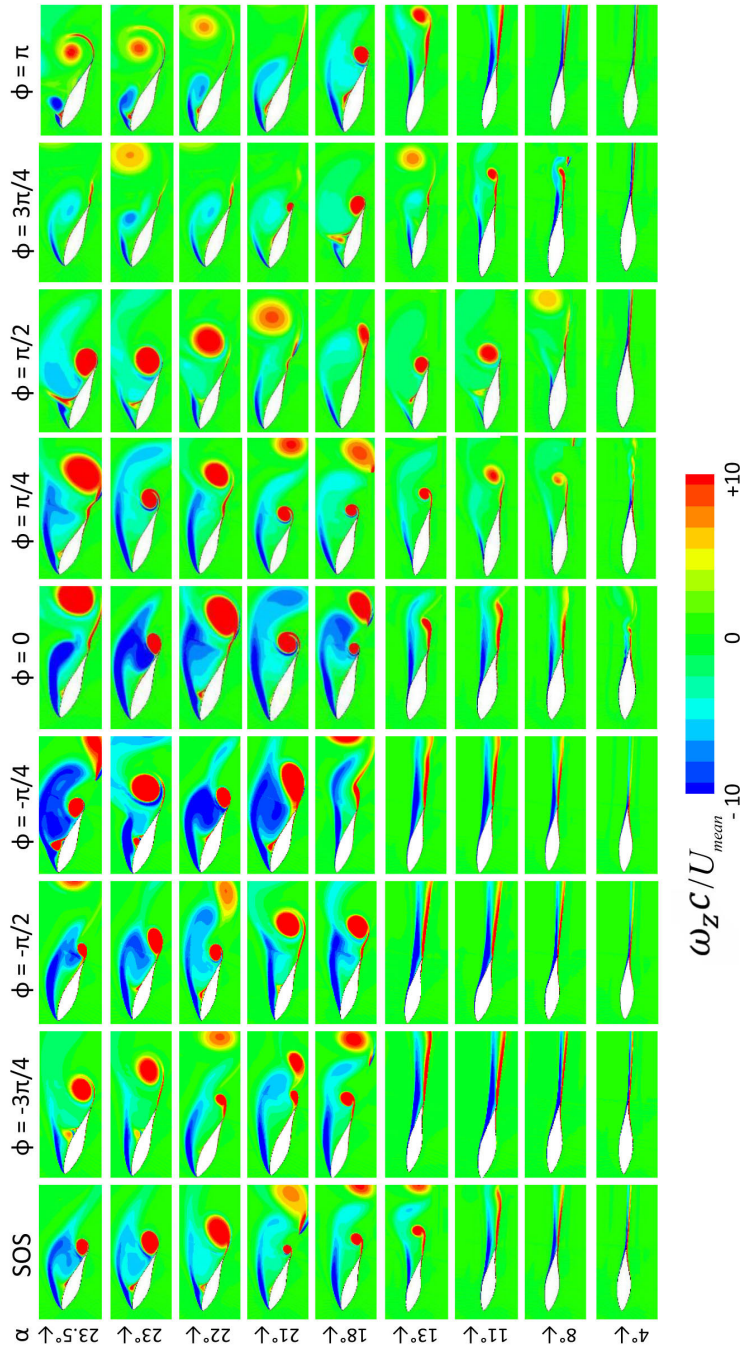

Figure 8.1: Vortical structure at different angles of attack ($Re = 10^6$).

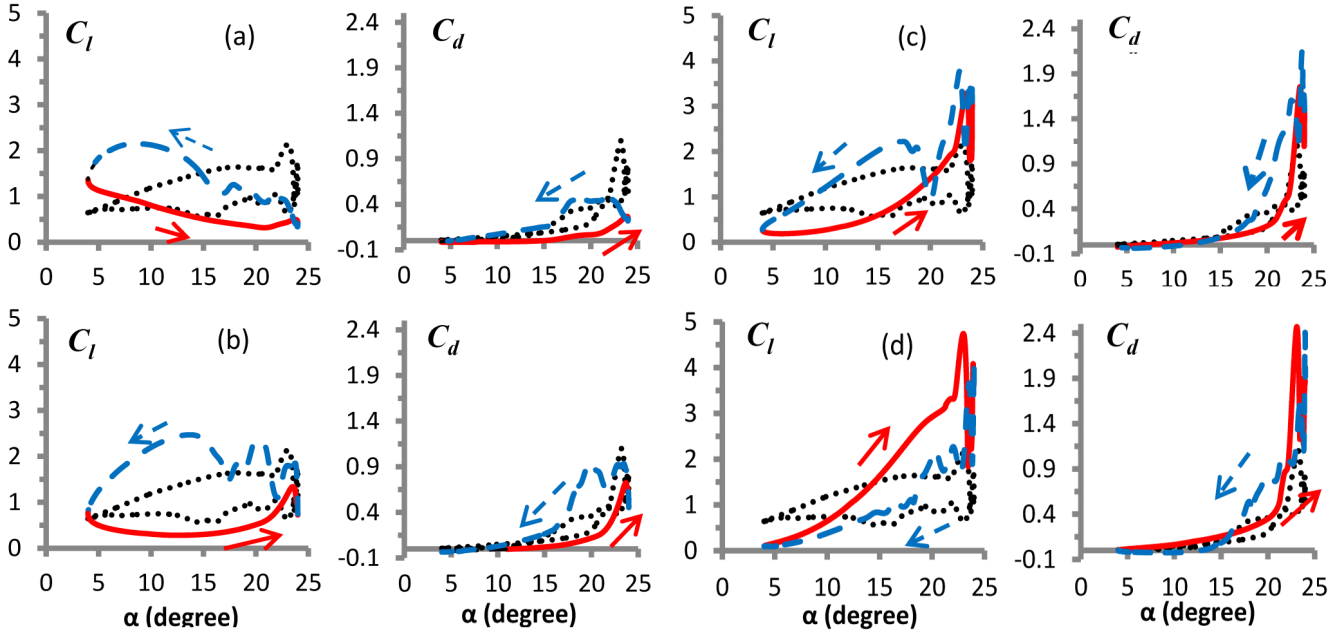
C_l
(a)
C_d
C_l
(c)
C_d
C_l
(b)
C_d
C_l
(d)
C_d
α (degree)
α (degree)
α (degree)
α (degree)

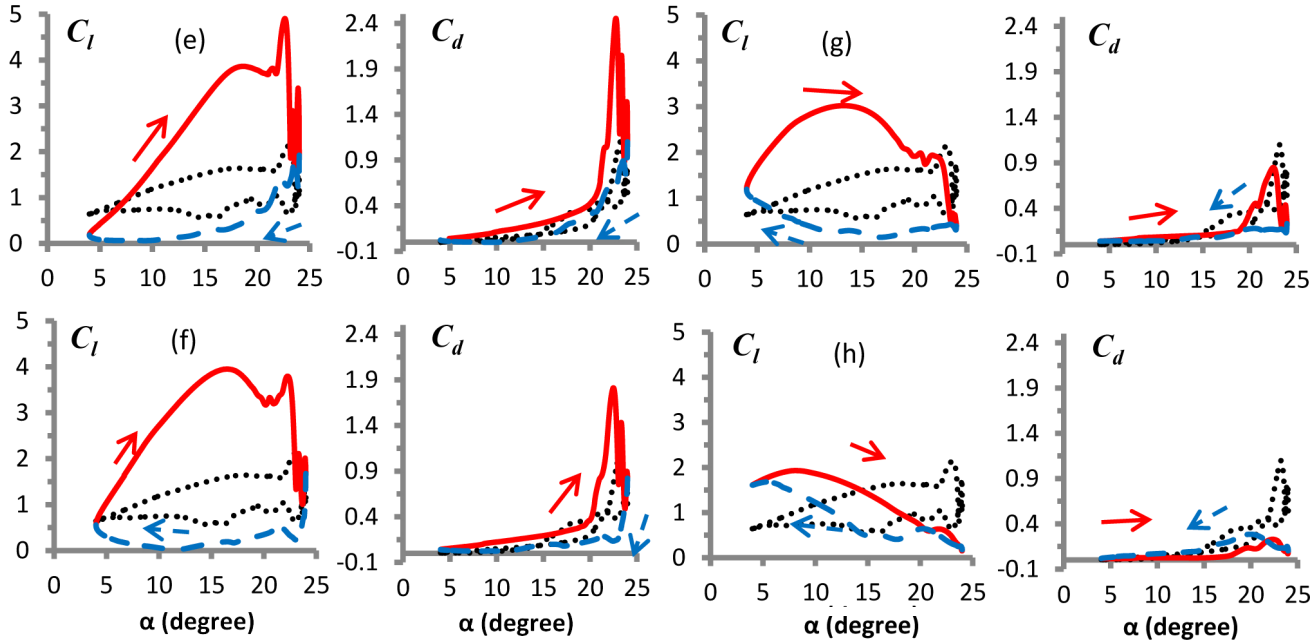

Figure 8.2: Aerodynamic loads ($Re = 10^6$); Legend: ... SOS, _ upstroke for COS and - - downstroke for COS.

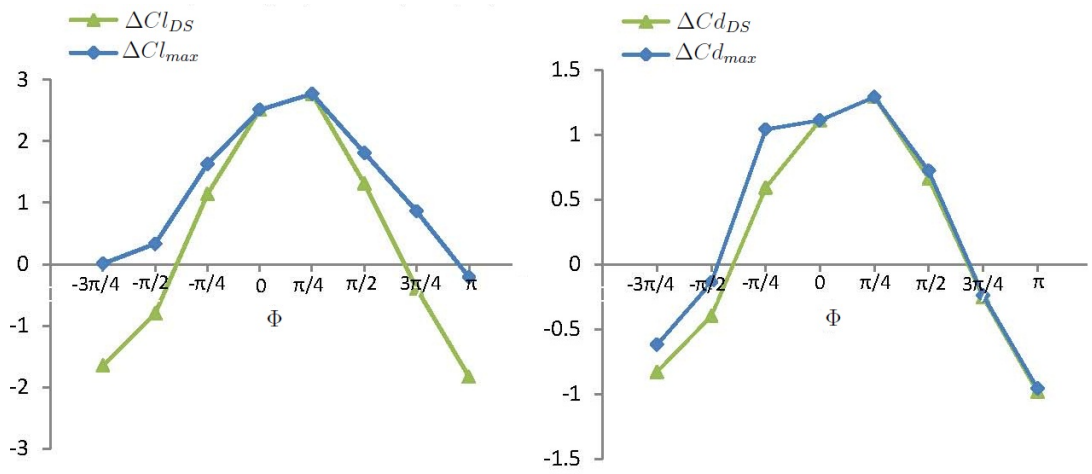

Figure 8.3: Load difference versus Φ, Equation 8.1 and 8.2.

Table 8.2: Summary of the critical angles of attack ($Re = 10^6$).

	SOS	Φ							
		$-3\pi/4$	$-\pi/2$	$-\pi/4$	0	$\pi/4$	$\pi/2$	$3\pi/4$	π
Reversed flow at trailing edge	14.0° ↑	10.8° ↑	11.9° ↑	15.1° ↑	15.4° ↑	14.5° ↑	13.2° ↑	13.2° ↑	12.0° ↑
1st LEV formation	19.7° ↑	16.0° ↑	17.6° ↑	20.3° ↑	20.7° ↑	20.6° ↑	20.5° ↑	19.0° ↑	18.1° ↑
DS/TEV formation	23.2° ↑	23.7° ↑	23.5° ↑	23.4° ↑	23.0° ↑	22.7° ↑	22.3° ↑	22.7° ↑	23.3° ↑
2nd LEV formation	23.3° ↑	23.2° ↑	23.7° ↑	23.5° ↑	23.2° ↑	23.0° ↑	22.6° ↑	22.5° ↑	22.3° ↑
2nd LEV pinch-off	23.9° ↓	22.7° ↓	23.7° ↓	24.0°	23.9° ↑	23.8° ↑	23.9° ↑	23.0° ↓	20.9° ↓
No vortex	13.1° ↓	14.9° ↓	8.7° ↓	7.8° ↓	4.5° ↓	8.7° ↓	8.7° ↓	10.9° ↓	14.2° ↓
Maximum incident velocity	–	6.9° ↓	14.0° ↓	21.0° ↓	24.0°	21.0° ↑	14.0° ↑	6.9° ↑	4.0°
Maximum C_l	23.2° ↑	8.7° ↓	13.8° ↓	22.8° ↓	23.0° ↑	22.7° ↑	16.3° ↑	13.5° ↑	8.0° ↑
Maximum C_d	23.2° ↑	21.8° ↓	19.8° ↓	23.7° ↓	23.0° ↑	22.7° ↑	22.5° ↑	22.6° ↑	19.7° ↑

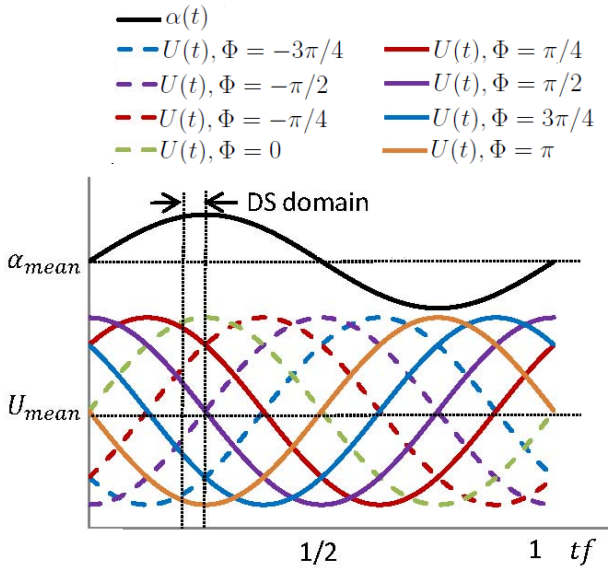

Figure 8.4: Angle of attack and streamwise freestream velocity oscillations with different Φ versus dimensionless time (tf); note dynamic stall for all cases in this study occurs inside the dynamic stall domain.

b) $U_{DS} > U_{mean}$ and $a_{DS} > 0$:
This subdomain occurs for $-\pi/2 < \Phi \leq 0$. Since the freestream velocity is accelerating, the maximum velocity is located slightly after dynamic stall; thus, the dynamic stall loads are lower than $\Phi = \pi/4$, but still very high compared to the SOS load values. In Figure 8.2 at an angle of attack of 23°, which is close to the dynamic stall angle for all cases, the LEV of $\Phi = 0$ has the maximum vorticity for $a_{DS} > 0$. Increasing the magnitude of Φ decreases the vortex strength significantly; the LEV of $\Phi = \pi$ has minimum vorticity. The dynamic stall aerodynamic loads are dominated by the strength of the vortices. Figure 8.5 shows that the vortex circulation of $\Phi = 0$ is significantly higher than that of $\Phi = \pi$ showing the same trend as their dynamic stall loads. The in-phase COS, $\Phi = 0$, increases the vorticity of the first LEV substantially in comparison with the SOS resulting in significant aerodynamic load augmentation (2.5 units and 1.1 units augmentation of C_l and Cd respectively) at an angle of attack of 23.2° when dynamic stall occurs. This strengthening is due to the close location of U_{max} to dynamic stall. For out-of-phase oscillations U_{max} is located at downstroke where strong vortices exist. The dynamic stall vorticity is increased because of high U_{DS}, but the maximum aerodynamic loads are in downstroke close to the location of U_{max}. After the maximum circulation, the vortex pinches off from the boundary layer.

Figure 8.6 shows that the maximum circulation of the downstroke vortices is higher than that of the upstroke ones which differ from the general behavior of the SOS boundary layer indicating that the boundary layer is more affected by the unsteady freestream velocity than unsteady angle of attack. Another interesting observation for out-of-phase oscillations in this subdomain is that the downstroke curve is located on top of the upstroke curve. Comparing to subdomain (a), the dynamic stall load values and locations are close, but the locations of the maximum loads differ. When the maximum loads are located in downstroke, the boundary layer is affected for the entire downstroke increasing the aerodynamic loads in comparison with the upstroke.

c) $U_{DS} < U_{mean}$ and $a_{DS} < 0$:

This subdomain occurs for $\pi/2 < \Phi \leq \pi$ where the maximum freestream velocity is located at a low angle of attack during upstroke. Of interest for high Φ values, the overall LEV-TEV vortex pair process during dynamic stall has not changed as shown in Figure 8.2. Low U_{DS} values cause lower vortex circulation, as seen for example in Figure 8.5 for $\Phi = \pi$. Thus, the dynamic stall aerodynamic loads are reduced consequently. For $\Phi = 3\pi/4$ in Table 8.2, the high angle difference between U_{max} and dynamic stall, 15.8°, increases the angle difference between $C_{l_{max}}$ and $C_{l_{DS}}$, 9.2°, but does not have an effect on the angle difference between $C_{d_{max}}$ and $C_{d_{DS}}$ and $C_{d_{max}} \approx C_{d_{DS}}$. As Φ reaches its highest value, π, $C_{d_{max}}$ occurs close to $C_{d_{DS}}$ and $C_{d_{max}} \approx C_{d_{DS}}$ but it is about 8 times lower than that of the SOS. Thus it can be inferred that a high angle of attack is of primary importance in the peak drag coefficient location; less vorticity in the dynamic stall vortices results in low peak drag values at high Φ; then, this subdomain can decrease the overall drag value of the whole cycle.

For $\Phi = \pi$, the $C_{l_{max}}$ value is close to that of the SOS. $C_{l_{max}}$ is shifted close to the maximum incident velocity and the difference between $C_{l_{max}}$ and $C_{l_{DS}}$ increases to almost 2 units, Figure 8.3. For this subdomain, since the angle of attack of $C_{l_{max}}$ is lower than the static stall angle, there is no sign of the LEV and then the focus should be on analyzing the behavior of the TEV. The TEV appears as a vortex sheet before the LEV is formed. A TEV with counter-clockwise rotation causes a downward normal force on the object resulting in lift reduction. The longer TEV sheet decreases the negative effect and is more favorable for lift augmentation [35, 51]. For $\Phi = 3\pi/4$, $C_{l_{max}}$ is located at $\alpha = 13.5° \uparrow$. At $\alpha = 13.5° \uparrow$, Figure 8.7 displays a longer TEV sheet for $\Phi = 3\pi/4$ compared to that of $\Phi = \pi$ with the lower lift value. For the SOS, at $\alpha = 13.5° \uparrow$, the length of the vortex sheet is close to that of $\Phi = \pi$ and the lift values are also similar at this angle. According to Gharali and Johnson [35], the freestream velocity affects the expansion speed of the TEV. At $\alpha = 13.5° \uparrow$, the freestream velocity is very close to the maximum value for $\Phi = 3\pi/4$,

then the TEV expands faster resulting in a longer vortex sheet. For $\Phi = \pi$, since the speed of the freestream is very close to U_{mean}, the TEV length is almost the same as that of the SOS. Figure 8.5 also shows that the low freestream velocity causes the rolled up TEV after dynamic stall for $\Phi = \pi$ to decay very slowly.

d) $U_{DS} < U_{mean}$ and $a_{DS} > 0$:
This subdomain occurs for $-\pi < \Phi \leq -\pi/2$. Since during dynamic stall the freestream is accelerating while U_{DS} is very low, the maximum freestream velocity is shifted to low angles of attack. The typical behaviors of the maximum and dynamic stall aerodynamic loads are almost the same as those of subdomain (c) with a main difference: the downstroke aerodynamic loads are higher than upstroke ones. This discrepancy is due to the maximum loads located at downstroke and as discussed before, they dominate the overall aerodynamic loop characteristics. Similar to the other cases, there is a phase difference between the maximum velocity and C_{lmax} agreeing with the results of Prater and Lian [86]. C_{dmax} is located at downstroke, but at high angles of attack, $\alpha > \alpha_{mean}$, similar to subdomain (b). During pitch down motion at low angles of attack, the vorticity of the consequent LEV-TEV pairs decrease until the flow is attached during downstroke. Table 8.2 (no vortex row) indicates the angles of attack at which there is no rolled up vortex connected to the boundary layer of the airfoil. For the SOS, after an angle of attack of 13.1° no rolled up vortex is attached to the airfoil, but for the COS, this angle is advanced at high Φ; for example for $\Phi = \pi$, there is no attached vortex at 14.2° (compare it with $\alpha = 4.5°$ for $\Phi = 0$, Table 8.2). These small vortices do not have high circulation to increase the aerodynamic loads and when they disappear a vortex sheet covers the wake, as shown in Figure 8.2 at $\alpha = 13° \downarrow$. Figure 8.8 shows a close up view of the vortex sheet at $\alpha = 13.8° \downarrow$ where C_{lmax} for $\Phi = -\pi/2$ is located. Similar to the upstroke, during downstroke the longer vortex sheet results in higher lift values.

8.4 Vortex growth time

Figure 8.5 shows that the LEV separation from the boundary layer (maximum vortex circulation) occurs slightly after the dynamic stall peak lift (Table 8.2); thus the phase delay can be ignored. When the LEV meets the trailing edge and dynamic stall occurs, a very small TEV is formed to complete the vortex pair. The emerging TEV gradually grows and covers a part of the suction surface where the LEV was located. Comparing with the results of Chapters 5 and 7 indicates that a lower reduced frequency and higher

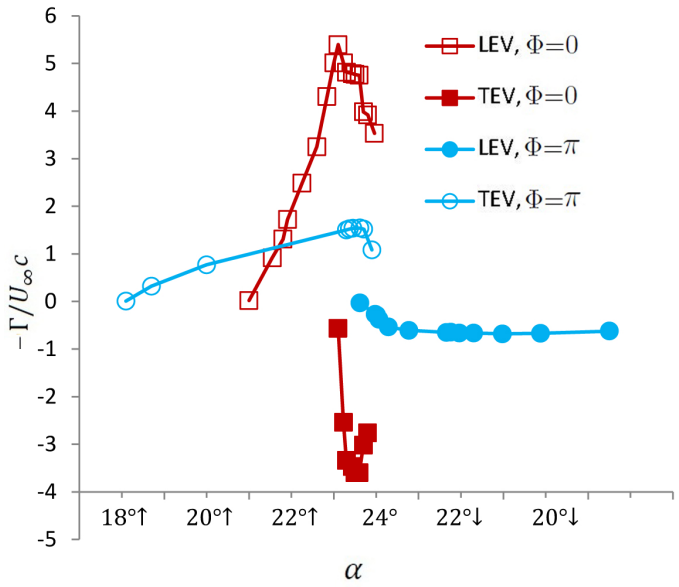

Figure 8.5: Vortex pair circulation for $\Phi = 0$ and $\Phi = \pi$.

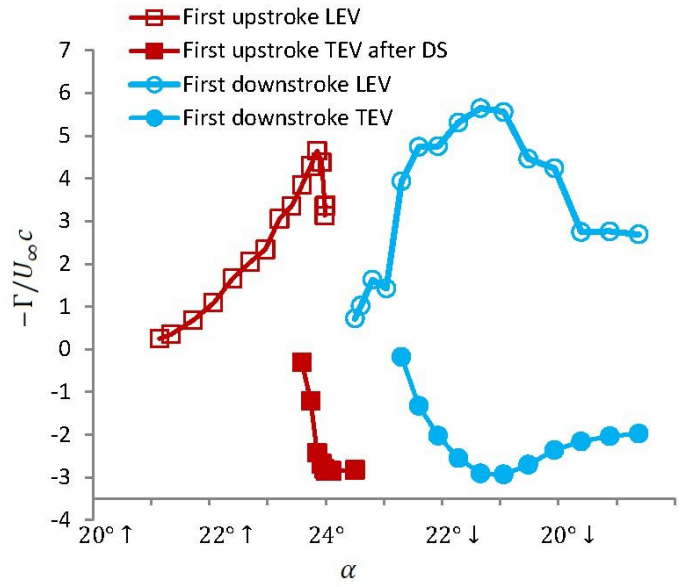

Figure 8.6: Circulations of the first upstroke and downstroke vortex pairs ($\Phi = -\pi/4$).

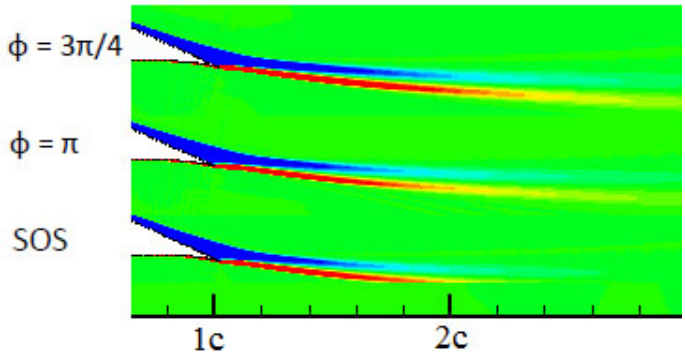

Figure 8.7: Vortical wake structure at $\alpha = 13.5^o \uparrow$.

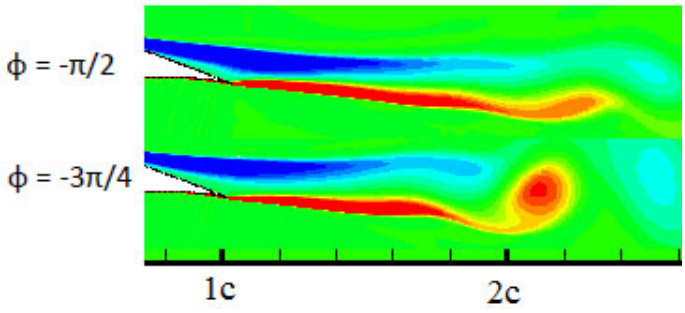

Figure 8.8: Vortical wake structure at $\alpha = 13.8^o \downarrow$.

Reynolds number causes a short phase delay.

The vortex growth time can be made dimensionless by the frequency of oscillation f,

$$\textit{Dimensionless vortex growth time} = f[\textit{vortex separation time} - \textit{vortex onset time}]. \tag{8.3}$$

The vortex growth time for the first two LEVs is tracked and compared in Figure 8.9 based on different Φ values. For $-\pi/4 \leq \Phi \leq \pi/2$, since the second fully developed LEVs are located in upstroke, their vortex growth times are very short. The figure also shows that during pitch down motion when the freestream is accelerating ($\Phi < -\pi/4$), the second vortex experiences faster freestream velocity and grows faster than the first one, in contrast to decelerating freestream ($\Phi > \pi/2$), the second LEV grows slowly. It can be concluded that a higher freestream velocity decreases the vortex growth time while increasing the vortex circulation.

The surrounding flow and the affected boundary layer influence the vortex generation and pinch off [35, 96]. For the SOS at the angle of attack around 19.7° ↑, the first LEV generates, but for the COS, this angle varies about 5° based on different Φ. For $\Phi = 0$, the first LEV initiates at 20.7° ↑ and as Φ increases, LEV formation occurs earlier and finally for $\Phi = \pi$ it occurs at 18.1° ↑. For the SOS, dynamic stall occurs at an angle of attack of 23.2° and for the COS, for various Φ, the dynamic stall stall angle variation is less than 1.5°. The ways that the boundary layer is adjusted at different domains are shown in Figure 8.10 for the first LEV. As the magnitude of Φ increases, the vortex growth time increases except subdomain (a), $U_{DS} > U_{mean}$ and $a_{DS} < 0$ ($0 < \Phi \leq \pi/2$), in which the boundary layer has the opposite behavior. In this subdomain, as Φ increases, dynamic stall occurs closer to U_{max} to increase the aerodynamic loads. This trend of the boundary layer results in shorter vortex growth time. These two different behaviors of the boundary layer in the whole Φ domain move toward increasing the dynamic stall vortex circulation and show that increasing vortex growth time is not always favorable for enriching vortex circulation.

In Figure 8.10, the range of $-\pi/4 \leq \Phi \leq \pi/2$ has the shortest vortex growth time and then the second LEV is fully developed during upstroke; see Figure 8.2c-f that the second lift peak is located during upstroke. For the SOS, if the reduced frequency is decreased, the boundary layer decreases the vortex growth time and then the second peak can occur during upstroke while the dynamic stall loads are decreased significantly [68]. Conversely, for the COS, the aerodynamic loads are increased dramatically while the second peak is located upstroke showing that the behavior of the boundary layer differs from that of the SOS.

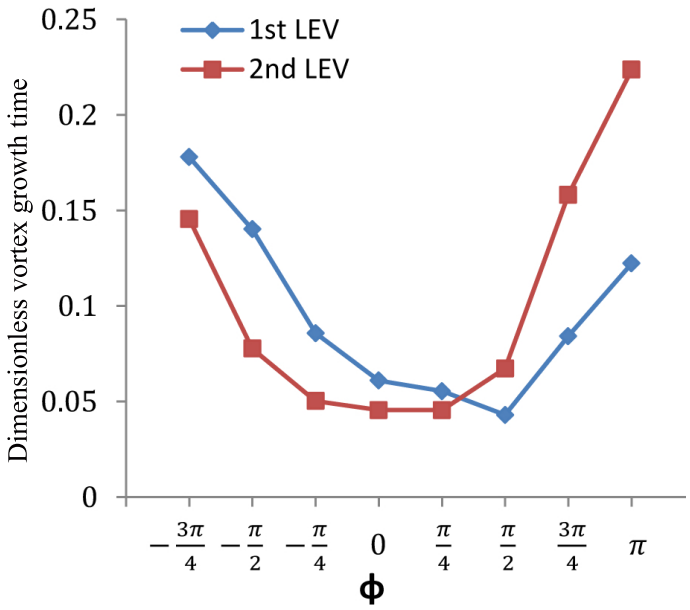

Figure 8.9: Dimensionless LEV growth time (Equation 8.3) versus Φ.

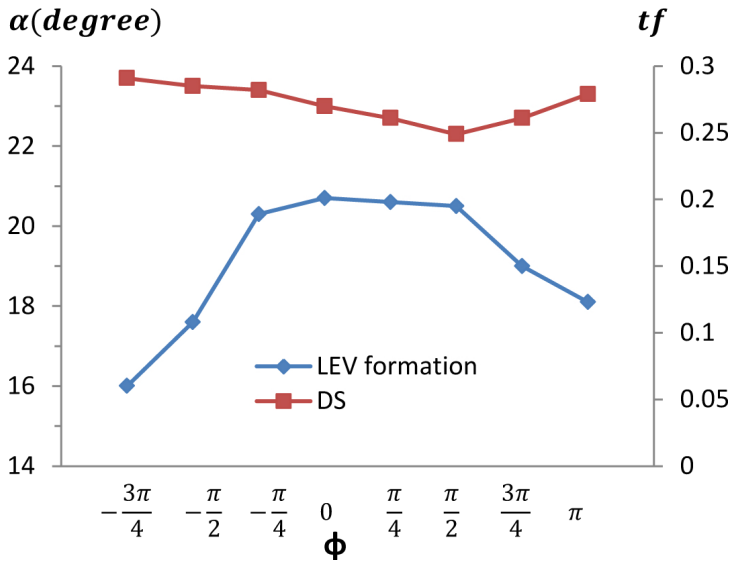

Figure 8.10: Angles and time of the first LEV formation and dynamic stall ($Re = 10^6$) versus Φ. Angles are in upstroke. Note difference between curves shows vortex growth time.

8.5 Pressure distribution

The simulated pressure distribution supports the above discussion and provides more information. In Figure 8.11, the pressure coefficient (Equation 3.8 where P_∞ is the static pressure of the incoming flow at one chord ahead of the airfoil location) is plotted for the SOS as well as for two critical Φ values, 0 and π, of the COS. In this figure, the streamlines are superimposed to present more details; for example, the reversed flows at the trailing edge are very clear in the first row which is common to the S809 airfoil [143], see Table 8.2 for critical angles of reversed flows. In one cycle, a strong suction usually occurs during the first LEV formation and development. For the SOS, the first LEV corresponds to the maximum aerodynamic loads occurring during dynamic stall. After convection of the first LEV, the higher pressure waves replace the first LEV resulting in drastically dropping aerodynamic loads. Among these three cases, the $\Phi = 0$ case has the strongest suction corresponding with the highest aerodynamic loads occurring in dynamic stall. On the contrary, for $\Phi = \pi$, the deterioration in suction, linked to the low incident velocity at high angles of attack, reduced overall aerodynamic loads considerably.

8.6 Summary

In this chapter, the pitch oscillating S809 airfoil configuration, subjected to unsteady incident velocities and compared with the steady incident velocity, was investigated using CFD with the Reynolds number of 10^6. For different Φ values, the boundary layer showed different and some times opposing behavior. Based on vortex interaction visualization and aerodynamic forces, the Φ domain was divided into four subdomains according to U_{DS} and a_{DS}: (a) the $U_{DS} > U_{mean}$ and $a_{DS} < 0$ ($0 < \Phi \leq \pi/2$) condition increased the circulation of the dynamic stall vortex pair and the dynamic stall loads were amplified consequently while the maximum aerodynamic loads were equal to the dynamic stall loads; (b) the $U_{DS} > U_{mean}$ and $a_{DS} > 0$ ($-\pi/2 < \Phi \leq 0$) condition postpones U_{max} after dynamic stall and when maximum loads were located at downstroke, the downstroke vortices had higher circulation than dynamic stall vortices, differed from the SOS, and the overall aerodynamic loads during downstroke are higher than those of upstroke although dynamic stall loads are significantly augmented; (c) the $U_{DS} < U_{mean}$ and $a_{DS} < 0$ ($\pi/2 < \Phi \leq \pi$) condition shifts Cl_{max} close to the U_{max} location at low angle of attack during upstroke before the static stall angle with a long vortex sheet while the dynamic stall loads are decreased dramatically; (d) the $U_{DS} < U_{mean}$ and $a_{DS} > 0$ ($\pi < \Phi \leq -\pi/2$) condition showed damped loads similar to subdomain (c) and switched upstroke and downstroke loads as in subdomain

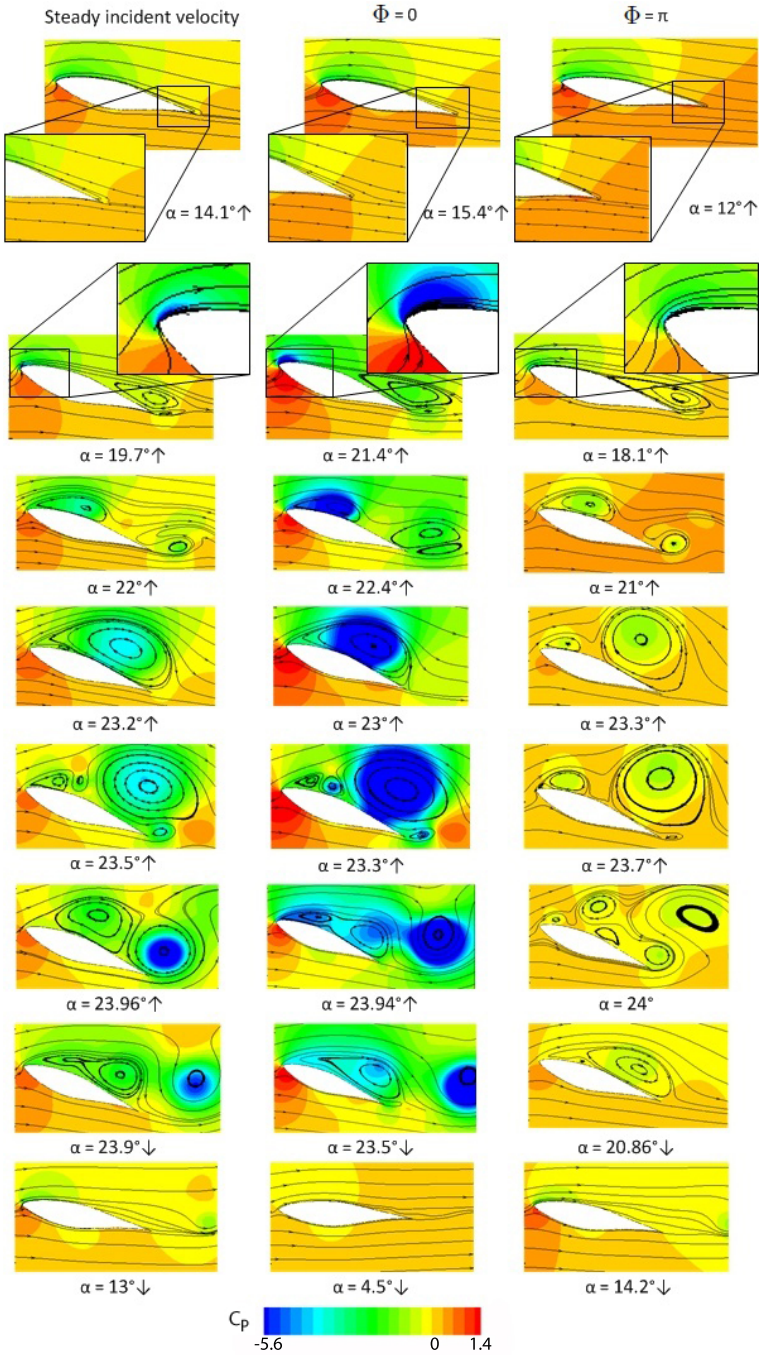

Figure 8.11: Static pressure coefficient distribution ($Re = 10^6$); left column: SOS; middle column: in-phase oscillations of COS ($\Phi = 0$); right column: out-of-phase oscillations of COS ($\Phi = \pi$).

(b) since the maximum loads were located in downstroke. Overall, the location of $C_{l_{max}}$ is related to the location of the maximum freestream velocity, but the location of the maximum drag value is close to the dynamic stall drag value, while its overall value decreases as the magnitude of Φ increases. Load controlling systems for different applications can also benefit from this variety in results under different Φ. When $U_{DS} > U_{max}$, the second LEV was fully developed in upstroke because of the short vortex growth time although aerodynamic loads are significantly high. That means for the COS, shorter vortex growth time is not always favorable for load reduction. These results of $0 \leq \Phi \leq \pi$ are consistent with those of Chapter 7, although the airfoil was NACA0012 and the Reynolds number, Re$\approx 10^5$, was one order of magnitude smaller.

Chapter 9

Conclusions and outlook

9.1 Conclusions

This study was organized to gain in-depth information about dynamic stall phenomena with the application to HAWTs under yaw loads. In the following the main findings are highlighted, although the summaries of previous chapters provide more details. Overall, this study is divided in two main parts based on a steady and an unsteady freestream.

Part I Experimental and Numerical study of a pitching airfoil under a steady freestream for $3.5 \times 10^4 \leq Re \leq 10^5$:

The main achievement of this part was that now calculating the PIV aerodynamic loads by a control-volume approach is possible not only for a dynamic airfoil but also for the deep dynamic stall phenomena when the dynamic stall vortices have made the flow field very complicated. The following items are also resulted from this part of study to answer questions 2-7 in Section 1.1.

- The PIV aerodynamic loads under high reduced frequencies can be determined, but at some cost. For the drag estimation, the downstream control-volume boundary should not be located close to the center of the vortices. The spatial resolution plays a significant role and should be high. High quality image pairs are needed for Reynolds shear stress calculation as well as to decrease errors. Finally, each individual determined load was considered reliable when it converged, agreed with the numerical simulation, and corresponded with all flow structures.

- The high resolution PIV study gave more insight into the vortical structure of dynamic stall phenomena. Increasing the reduced frequency results in enriched vortex growth time and phase delay. The vortex circulation and trajectory analysis showed that at high reduced frequency, a TEV started rolling up after stall and decreasing the lift value while the LEV was growing with a significant phase delay. After the LEV was pinched off, it did not move downstream until the TEV was separated from the boundary layer; thus, there is a strong correlation between dynamic stall vortices.

- The calculated PIV pressure field showed low pressure waves at the center of vortices. If the circulation of a vortex decreases, the pressure level of that vortex increases agreeing with the lift trend.

- The height of the bubble was introduced as an indicator for studying the behavior of the LSB versus reduced frequency variations. Increasing the reduced frequency decreases the bubble height while advancing the laminar to turbulent transition. Hence, increasing reduced frequency results in a thinner LSB; in terms of the load study, this conclusion is valuable since LSB formation is not favorable.

- Based on the phase averaged PIV results and the CFD simulation, the trailing edge vortices appeared as a sheet vortex at low angles of attack. Flow visualization showed that a vortex sheet presented shed vortices that were separated randomly from the training edge without a particular pattern. Dynamic stall phenomena create a barrier between the random vortical pattern and the organized vortical pattern with repeatable LEVs and TEVs.

- For HAWTs, which usually work under small yaw errors, a pitching airfoil study within a static stall angle showed no significant vortical and wake differences, although the rotor experienced unbalanced aerodynamic loads in one revolution.

Part II Numerical study of a pitching airfoil under an unsteady freestream for $10^5 \leq Re \leq 10^6$.

Analyzing the HAWT blade elements showed that when the rotor is operating under yaw loads, the incident velocity is oscillating periodically similar to the angle of attack oscillation. Therefore, the effects of the oscillating incident (freestream) velocity on dynamic stall events have been studied. Changing the main parameter Φ, the phase difference between the freestream oscillation and the airfoil oscillation, from $-\pi$ to π with the same frequency of oscillations has provided some answers for questions 9-12 in Section 1.1.

- According to the aerodynamic loads and flow structures, the Φ variation was divided into four subdomains based on U_{DS} and a_{DS}. Several times augmented dynamic load values to several times damped dynamic load ones (some dynamic stall loads were damped even under static stall load values) were reported. The maximum loads appeared in locations different from the location of the dynamic stall loads and even in some subdomains, the maximum loads were located during downstrokes.

- At low Φ values, the vortex growth time showed completely different trends and circumstances than that of the pitching airfoil under a steady freestream. As the vortex growth time decreased, the aerodynamic loads increase and the second LEV appears during upstrokes. Thus, the assumption of decreasing vortex growth time to decrease aerodynamic loads does not apply for low Φ values. The maximum vortex circulation also did not always belong to the dynamic stall vortices; all these observations completely differ from those of the steady freestream.

- An accelerating freestream at low angles speeds the vortex sheet expansion in the wake and resulted in a longer vortex sheet which increased lift significantly since the longer trailing edge vortex sheet was favorable for the lift augmentation.

- The overall results were consistent when the Reynolds number and the shape of the airfoil were changed.

9.2 Outlook

Both experimental and numerical methods have limitations in many respects. Hybrid PIV-CFD methods are recommended to overcome the limitations of each method. CFD methods can predict the flow field in an area with poor experimental data, can post process the velocity field with advanced algorithms and also can extend the 2D flow field to a 3D one.

For future consideration, significantly higher spatial resolution should be taken into account for PIV load determination of dynamic airfoils with high reduced frequencies.

Three-dimensional PIV and CFD studies are also recommended especially with industrial applications. Although 3D studies are both numerically and experimentally expensive, they can provide valuable information regarding dynamic stall and vortical structures especially during downstroke. For 3D PIV techniques such as the stereoscopic and tomographic methods, the pressure and load calculation codes should be upgraded to 3D. In this regard, 3D synthetic images are needed to validate the upgraded codes.

The Time-Resolved PIV technique provides the opportunity to calculate instantaneous loads and to visualize dynamic stall events just for one cycle. Since the Reynolds number in this study is moderate, selecting proper PIV equipment plays an important role.

A tremendous effort is needed to measure the incident velocity variations of large scale wind turbine blades under dynamic loads. It will be valuable to show the incident velocity variation domain versus angle of attack variation range for a HAWT blade element under different circumstances.

Because of different causes of yaw loads, many states are possible. Analyzing each individual or combination of these states provides frequency of oscillation and reduced amplitude domains which can be used for future studies of dynamic stall in HAWTs.

References

[1] ANSYS Fluent, Academic Research, V13 and V12.1.

[2] Dantec Dynamics A/S, BSA flow software version 4 installation, user's guide, 2005.

[3] R J Adrian and J Westerweel. *Particle Image Velocimetry*. Cambridge, New York : Cambridge University Press, 2011.

[4] S A Ahmadi, S Sharif, and R Jamshidi. A numerical investigation on the dynamic stall of a wind turbine section using different turbulence models. *WASET*, 58:290–296, 2009.

[5] H E Albrecht, M Borys, N Damaschke, and C Tropea. *Laser Doppler and Phase Doppler Measurement Techniques*. Springer, NY, 2003.

[6] S Bansmer and R Radespiel. Validation of unsteady Reynolds-Averaged Navier-Stokes simulations on three-dimensional flapping wings. *AIAA J*, 50(1):190–202, 2012.

[7] S Bansmer, R Radespiel, R Unger, M Haupt, and P Horst. Experimental and numerical fluid-structure analysis of rigid and flexible flapping airfoils. *AIAA J*, 48(9):1959–1974, 2010.

[8] G Barakos and D Drikakis. Computational study of unsteady turbulent flows around oscillating and ramping airfoil. *Int J Numer Meth Fl*, 42:163–186, 2003.

[9] J B Barlow, W H Rae, and A Pope. *Low-Speed Wind Tunnel Testing, Third Edition*. John Wiley Sons Inc., NY, 1999.

[10] P W Bearman. Vortex shedding from oscillating bluff bodies. *Ann Rev Fluid Mech*, 16:195–222, 1984.

[11] L Benedict and R Gould. Towards better uncertainty estimates for turbulence statistics. *Exp Fluids*, 22(2):129–136, 1996.

[12] E Berton, D Favier, M NsiMba, C Maresca, and C Allain. Embedded LDV measurement methods applied to unsteady flow investigation. *Exp Fluids*, 30:102–110, 2001.

[13] E Berton, C Maresca, and D Favier. A new experimental method for determining local airloads on rotor blades in forward flight. *Exp Fluids*, 37:455–457, 2004.

[14] D G Bohl and M M Koochesfahani. MTV measurements of the vortical field in the wake of an airfoil oscillating at high reduced frequency. *J Fluid Mech*, 620:63–88, 2009.

[15] T Burton, D Sharpe, N Jenkins, and E Bossanyi. *Wind Energy Handbook*. John Wiley and Sons, 2001.

[16] B H Carmichael. Low Reynolds number airfoil survey. NASA Contractor Report No. 165803, 1982.

[17] L W Carr, K W McAlister, and W J McCroskey. Analysis of the development of dynamic stall based on oscillating airfoil experiments, NASA TN D-8382. Technical report, 1977.

[18] E W Casimiri. Evaluation of a non-intrusive airfoil load determination method based on PIV. Master's thesis, Delft University of Technology, The Netherlands, 2006.

[19] T Cebec, M Platzer, H Chen, K Chang, and J P Shao. *Analysis of low-speed unsteady airfoil flows*. Springer, Heidelberg, Germany, 2005.

[20] M S Chandrasekhara and L W Carr. Flow visua1ization studies of the Mach number effects on dynamic staIl of an oscillating airfoil. *J Aircraft*, 27:516–522, 1990.

[21] L David, T Jardin, and A Farcy. On the non-intrusive evaluation of fluid forces with the momentum equation approach. *Meas Sci Technol*, 20:1–11, 2009.

[22] S S Diwan and O N Ramesh. Laminar separation bubbles: dynamics and control. In *Sadhana – Academy Proceedings in Engineering Science*, 32:103-109, 2007.

[23] M Drela and H Youngren. XFOIL: An analysis and design system for low Reynolds number airfoils. In *Conference on Low Reynolds Number Airfoil Aerodynamics. University of Notre Dame*, page 1, 1989.

[24] J Ekaterinaris. Numerical investigation of dynamic stall of an oscillating wing. *AIAA J*, 33:1803–1808, 1995.

[25] L E Ericsson and J P Reding. Fluid mechanics of dynamic stall Part 1. Unsteady flow concepts. *J Fluids and Struct*, 2:1–33, 1988.

[26] D Favier. The role of wind-tunnel experiments in CFD Validation. *Encyclopedia of Aerospace Engineering*, 1:351–366, 2010.

[27] D Favier, A Agnes, C Barbi, and C Maresca. Combined translation/pitch motion - A new airfoil dynamic stall simulation. *J Aircraft*, 25(9):805–814, 1988.

[28] D Favier, J Beleudy, and C Maresca. Influence of coupling incidence and velocity variations on the airfoil dynamic stall. In *48th Annual Forum of the American Helicopter Society, Washington, D.C.*, 1992.

[29] D Favier, C Maresca, and J Rebont. Dynamic stall due to fluctuations of velocity and incidence. *AIAA J*, 20:865–871, 1982.

[30] P Gerontakos. An experimental investigation of flow over an oscillating airfoil. Master's thesis, McGill University, Montreal, Quebec, Canada, 2004.

[31] K Gharali, M Gu, and D A Johnson. A PIV study of a low Reynolds number pitch oscillating SD7037 airfoil in dynamic stall with CFD comparison. In *16th Int. Symp. Appl Laser Tech Fluid Mechanics, Lisbon, Portugal*, 2012.

[32] K Gharali and D A Johnson. Pressure and acceleration determination methods using PIV velocity data. In *ASME Fluids Engineering Conference, Jacksonville, Florida, USA*, 2008.

[33] K Gharali and D A Johnson. Numerical modeling of pitch oscillating S809 airfoil dynamic stall in 2D with application to a Horizontal Axis Wind Turbine. In *International Green Energy conference IGEC V, Waterloo, Canada*, 2010.

[34] K Gharali and D A Johnson. Numerical modeling of an S809 airfoil under dynamic stall, erosion and high reduced frequencies. *Appl Energy*, 93:45–53, 2012.

[35] K Gharali and D A Johnson. Dynamic stall simulation of a pitching airfoil under unsteady freestream velocity, (in press). *J Fluids and Struct*, 2013.

[36] K Gharali and D A Johnson. Reduced frequency effects on Laminar Separation Bubbles. In *10th International Symposium on Particle Image Velocimetry, Delft, The Netherlands*, 2013.

[37] P Gigue and M Selig. Low Reynolds number airfoils for small horizontal axis wind turbines. *Wind Eng*, 32:367–380, 1997.

[38] R Gilbert. Evaluation of FFT based cross-correlation algorithms for particle image velocimetry. Master's thesis, University of Waterloo, Waterloo, Canada, 2002.

[39] R Gilbert and D A Johnson. Evaluation of FFT-based cross-correlation algorithms for PIV in a periodic grooved channel. *Exp Fluids*, 34:473–483, 2003.

[40] S Gupta and J Leishman. Dynamic stall modelling of the S809 aerofoil and comparison with experiments. *Wind Energy*, 9:521–547, 2006.

[41] W Haans, T Sant, G V Kuik, and G V Bussel. Measurement of tip vortex paths in the wake of a HAWT under yawed flow conditions. *J Sol Energy Eng.*, 127:437–596, 2005.

[42] A C Hansen. Yaw dynamics of Horizontal Axis Wind Turbines. NREL/TP-442-4822. Technical report, 1992.

[43] M K Heerenbrink. Simultaneous PIV and balance measurements on a pitching aerofoil. Master's thesis, Delft University of Technology, The Netherlands, 2011.

[44] H Horton. *Laminar Separation Bubbles in Two and Three Dimensional Incompressible Flow*. PhD thesis, Department of Aeronautical Engineering, Queen Mary College, University of London, 1968.

[45] H Hu and Z Yang. An experimental study of the laminar flow separation on a low-Reynolds-number airfoil. *J Fluids Eng*, 130:1–11, 2008.

[46] J Johansen. Unsteady airfoil flows with application to aeroelastic stability Risø-R-1116(EN). Technical report, 1999.

[47] W Johnson and N D Ham. On the mechanism of dynamic stall. *J Am Helicopter Soc*, 17(4):36–45, 1972.

[48] W P Jones and B E Launder. The prediction of laminarization with a two-equation model of turbulence. *Int J of Heat and Mass Transfer*, 15:301–314, 1972.

[49] Y W Jung and S O Park. Vortex shedding characteristics in the wake of an oscillating airfoil at low Reynolds number. *J Fluids Struct*, 20:451–464, 2005.

[50] R De Kat. *Instantaneous planar pressure determination from particle image velocimetry*. PhD thesis, Delft University of Technology, The Netherlands, 2012.

[51] J Katz and A Plotkin. *Low Speed Aerodynamics*. Cambridge University Press, Cambridge, 2001.

[52] J S Kim and S O Park. Smoke wire visualization of unsteady separation over an oscillating airfoil. *AIAA J*, 26(11):1408–1410, 1988.

[53] S Ko and W McCroskey. Computations of unsteady separating flows over an oscillating airfoil. *AIAA J*, 35:1235–1238, 1997.

[54] S B R Kottapalli and G A Pierce. Drag on an oscillating airfoil in a fluctuating free stream. *J Fluids Eng*, 101:391–399, 1979.

[55] D Kurtulus, F Scarano, and L David. Unsteady aerodynamic forces estimation on a square cylinder by TR-PIV. *Exp Fluids*, 42(2):185–196, 2007.

[56] T Lee and S Basu. Measurement of unsteady boundary layer developed on an oscillating airfoil using multiple hot-film sensors. *Exp Fluids*, 25:108–117, 1998.

[57] T Lee and P Gerontakos. Investigation of flow over an oscillating airfoil. *J Fluid Mech*, 512:313–341, 2004.

[58] J G Leishman. Challenges in modelling the unsteady aerodynamics of wind turbines. *Wind Energy*, 5:85–132, 2002.

[59] J G Leishman. *Principles of helicopter aerodynamics. Cambridge Aerospace series, 18*. Cambridge University Press, Cambridge, 2006.

[60] Y Lian and W Shyy. Laminar-turbulent transition of a Low Reynolds number rigid or flexible airfoil. *AIAA J*, 45(7):1501–1513, 2007.

[61] T Maeda, Y Kamada, J Suzuki, and H Fujioka. Rotor blade sectional performance under yawed inflow conditions. *J Sol Energy Eng*, 130:031018, 2008.

[62] J M Martin, R W Empey, W J McCroskey, and F X Caradonna. An experimental analysis of dynamic stall on an oscillating airfoil. *J Am Helicopter Soc*, 19(1):26–32, 1974.

[63] G Martinat, M Braza, G Harrana, A Sevrain, G Tzabiras, Y Hoarau, and D Favier. Dynamic stall of a pitching and horizontally oscillating airfoil. In *IUTAM Symposium on Unsteady Separated Flows and their Control, Springer, Netherlands*, volume 14, 2009.

[64] K W McAlister, L W Carr, and W J McCroskey. Dynamic stall experiments on the NACA 0012 airfoil. NASA TP 1100. Technical report, 1978.

[65] W McCroskey. The phenomenon of dynamic stall. NASA TM-81264. Technical report, NASA TM-81264, 1981.

[66] W McCroskey. Unsteady airfoils. *Annu Rev Fluid Mech*, 14:285–311, 1982.

[67] W J McCroskey. Some current research in unsteady fluid dynamics. *J Fluids Eng*, 99:8–39, 1977.

[68] W J McCroskey, L W Carr, and K W McAlister. Dynamic stall experiments on oscillating airfoils. *AIAA J*, 14:57–63, 1976.

[69] W J McCroskey, K W McAlister, L W Carr, S L Pucci, and O Lamber. Dynamic stall on advanced airfoil sections. *J Am Helicopter Soc*, 26(3):40–50, 1981.

[70] C Mellen, J Frohlich, and W Rodi. Lessons from LESFOIL project on large-eddy simulation of flow around an airfoil. *AIAA J*, 41:573–581, 2003.

[71] F R Menter. Two-equation eddy-viscosity turbulence models for engineering applications. *AIAA J*, 32:1598–1605, 1994.

[72] F R Menter, R B Langtry, S R Likki, Y B Suzen, P G Huang, and S Volker. A correlation based transition model using local variables Part I- model formulation. In *ASME Turbo Expo, Vienna, Austria*, 2004.

[73] F R Menter, R B Langtry, and S Volker. Transition modeling for general purpose CFD codes. *Flow Turbul Combust*, 77:277–303, 2006.

[74] M Narayana, G A Putrus, P S Leung, M Jovanovic, and S McDonald. Development of a model to investigate the yaw behaviour of small horizontal axis wind turbines. *Proc IMechE*, 226:86–97, 2012.

[75] R Nobile, M Vahdati, J Barlow, and A M Crook. Dynamic stall for a Vertical Axis Wind Turbine in a two-dimensional study. In *World Renewable Energy Congress, Sweden*, 2011.

[76] F Noca, D Shiels, and D Jeon. Measuring instantaneous fluid dynamic forces on bodies, using only velocity fields and their derivatives. *J Fluids and Struct*, 11(3):345–350, 1997.

[77] M V Ol, L Bernal, C K Kang, and W Shyy. Shallow and deep dynamic stall for flapping low Reynolds number airfoils. *Exp Fluids*, 46:883–901, 2009.

[78] M V Ol, B McAuliffe, E S Hanff, U Scholz, and C Kahler. Comparison of laminar separation bubble measurements on a low Reynolds number airfoil in three facilities. In *35th AIAA Fluid Dynamics Conference and Exhibit, Toronto, Ontario, Canada*, 2005.

[79] M M O'Meara and T J Mueller. Laminar separation bubble characteristics on an airfoil at low Reynolds numbers. *AIAA J*, 25:1033–1041, 1987.

[80] S M Orlando. Laser doppler anemometry and acoustic measurements of an S822 airfoil at low Reynolds numbers. Master's thesis, University of Waterloo, Waterloo, Canada, 2011.

[81] O Ozgener and L Ozgener. Exergy and reliability analysis of wind turbine systems: a case study. *Renewable and Sustainable Energy Rev*, 11:1811–1826, 2007.

[82] J Panda and K B M Q Zaman. Experimental investigation of the flow field on an oscillating airfoil and estimation of lift from wake surveys. *J Fluid Mech*, 265:65–95, 1994.

[83] A Pelletier and T J Mueller. Low Reynolds number aerodynamics of low-aspect-ratio, thin/flat/cambered-plate wings. *J Aircraft*, 37(5):825–832, 2000.

[84] G A Pierce, D L Kunz, and B B Malone. The effect of varying freestream velocity on dynamic stall characteristics. *J Am Helicopter Soc*, 23:27–33, 1978.

[85] T Prangemeier, D Rival, and C Tropea. The manipulation of trailing-edge vortices for an airfoil in plunging motion. *J Fluids and Struct*, 26(2):193–204, 2010.

[86] R Prater and Y Lian. Numerical analysis of aerodynamic characteristics of a flat plate in gusting low Reynolds number flow. In *28th AIAA paper 4564, Chicago, Illinois*, 2010.

[87] R Prater and Y Lian. Aerodynamic response of stationary and flapping wings in oscillatory low Reynolds number flows. In *50th AIAA paper 418, Nashville, Tennessee*, 2012.

[88] M Raffel, D Favier, E Berton, C Rondot, M Nsimba, and W Geissler. Micro-PIV and ELDV wind tunnel investigations above a helicopter blade tip. *Measur Sci Technol*, 17:1652–1658, 2006.

[89] M Raffel, J Kompenhans, and P Wernert. Investigation of the unsteady flow velocity field above an airfoil pitching under deep dynamic stall conditions. *Exp Fluids*, 19:103–111, 1995.

[90] M Raffel, C Willert, and J Kompenhans. *Particle Image Velocimetry*. Springer-Verlag, New York, 1998.

[91] D Ragni. *PIV-based load determination in aircraft propellers*. PhD thesis, Delft University of Technology, The Netherlands, 2012.

[92] D Ragni, B W van Oudheusden, and F Scarano. PIV-load determination in aircraft propellers. In *16th Int Symp on Applications of Laser Techniques to Fluid Mechanics. Lisbon, Portugal*, 2012.

[93] R Ramsay, M J Homan, and G M Gregorek. Effects of grit roughness and pitch oscillation on the S809 airfoil. NREL/TP-442-7817. Technical report, 1995.

[94] D Rival, G Hass, and C Tropea. The recovery of energy from leading- and trailing-edge vortices in tandem-airfoil configurations. *J Aircraft*, 48(1):203–211, 2011.

[95] D Rival, R Manejev, and C Tropea. Measurement of parallel blade-vortex interaction at low Reynolds numbers. *Exp Fluids*, 49(1):89–99, 2010.

[96] D Rival, T Prangemeier, and C Tropea. The influence of airfoil kinematics on the formation of leading-edge vortices in bio-inspired flight. *Exp Fluids*, 46(5):823–833, 2009.

[97] D Rival and C Tropea. Characteristics of pitching and plunging airfoils under dynamic-stall conditions. *J Aircraft*, 47(1):80–86, 2010.

[98] D E Rival. *Development, Control and Recovery of Leading- and Trailing-Edge Vortices in Tandem-Airfoil Configurations*. PhD thesis, Darmstadt, 2009.

[99] W Rozenn, C S Michael, L J Torben, and P S Uwe. Simulation of shear and turbulence impact on wind turbine performance. Risø-R-1722(EN). Technical report, 2010.

[100] H Sadeghi and M Mani. Measurements of the flow field behind a helicopter blade using the hot-wire anemometry. *J Information Comm Tech*, 2:32–39, 2009.

[101] S B Savaliya, S P Kumar, and S Mittal. Laminar separation bubble on an Eppler 61 airfoil. *Int J Numer Methods Fluids*, 64:627–652, 2010.

[102] F Scarano and M L Riethmuller. Iterative multigrid approach in PIV image processing with discrete window offset. *Exp Fluids*, 26:513–523, 1999.

[103] M S Selig, J J Guglielmo, A P Broeren, and P Giguere. *Summary of low-speed airfoil data, Vol. 1*. SoarTech Pulications, VA, 1995.

[104] M S Selig, C A Lyon, P Giguere, C P Ninham, and J J Guglielmo. *Summary of low speed airfoil data, Vol. 2*. SoarTech Publications, VA, 1996.

[105] M S Selig and B D McGranahan. Wind tunnel aerodynamic tests of six airfoils for use on small wind turbines. *ASME J Sol Energy Eng*, 126:986–1001, 2004.

[106] M S Selig and B D McGranahan. Wind tunnel aerodynamic tests of six airfoils for use on small wind turbines, NREL/SR-500-34515. Technical report, NREL, 2004.

[107] W Sheng, R Galbraith, and F Coton. A modified dynamic stall model for low Mach numbers. *ASME J Sol Energy Eng*, 130:310–313, 2008.

[108] W Sheng, R A McD Galbraith, and F N Coton. On the S809 airfoil's unsteady aerodynamic characteristics. *Wind Energy*, 12:752–767, 2009.

[109] Z W Shi and X Ming. Effects of unsteady freestream on aerodynamic characteristics of pitching delta wing. *J Aircraft*, 45:2182–2185, 2008.

[110] Z W Shi and X Ming. Experimental investigation on a pitching motion delta wing in unsteady free stream. *Mod Phys Lett B*, 23:409–41, 2009.

[111] R K Singh, M R Ahmed, M L Zullah, and Y H Lee. Design of a low Reynolds number airfoil for small horizontal axis wind turbines. *Renewable Energy*, 42:66–76, 2012.

[112] E Skensved. Air jets for lift control in low Reynolds number flow. Master's thesis, University of Waterloo, Waterloo, Canada, 2010.

[113] D M Somers. Design and experimental results for the S809 airfoil NREL/SR-440-6918. Technical report, NREL, 1997.

[114] D M Somers. The S822 and S823 airfoils. Subcontractor report 500-36342. Technical report, NREL, 2005.

[115] D M Somers and M D Maughmer. Theoretical aerodynamic analyses of six airfoils for use on small wind turbines. NREL/SR-500-33295. Technical report, NREL, 2002.

[116] L J Souverein, B W van Oudheusden, and F Scarano. Particle image velocimetry based load determination in supersonic flows. In *45th AIAA Aerospace Sciences Meeting and Exhibit, Reno, Nevada*, 2007.

[117] P Spalart and M Strelets. Mechanisms of transition and heat transfer in a separation bubble. *J Fluid Mech*, 403:329–349, 2000.

[118] A Spentzos, G Barakos, K Badcock, B Richards, P Wernert, S Schreck, and M Raffel. Investigation of three-dimensional dynamic stall using computational fluid dynamics. *AIAA J*, 43:1023–1033, 2005.

[119] B Sperandei. The application of particle image velocimetry in a small scale wind tunnel. Master's thesis, University of Waterloo, Waterloo, Canada, 2002.

[120] J L Tangler and D M Somers. NREL airfoil families for HAWTs, NREL/TP-442-7109. Technical report, 1995.

[121] K Tsuchiya and L S Fan. Near-wake structure of a single gas bubble in a two-dimensional liquid-solid fluidized bed: Vortex shedding and wake size variation. *Chem Eng Sci*, 43(5):1167–1181, 1988.

[122] M F Unal, J C Lin, and D Rockwell. Force prediction by PIV imaging: a momentum based approach. *J Fluids and Struct*, 11:965–971, 1997.

[123] B W van Oudheusden, E W F Casimiri, and F Scarano. Aerodynamic load measurement of a low speed airfoil using particle image velocimetry. In *AIAA 45th Aerospace Science Meeting and Exhibit, Reno, Nevada (USA)*, 2007.

[124] B W van Oudheusden, F Scarano, and E W F Casimiri. Non-intrusive load characterization of an airfoil using PIV. *Exp Fluids*, 40:988–992, 2006.

[125] B W van Oudheusden, F Scarano, E W M Roosenboom, E W F Casimiri, and L J Souverein. Evaluation of integral forces and pressure fields from planar velocimetry data for incompressible and compressible flows. In *13th Int Symp on Applications of Laser Techniques to Fluid Mechanics, Lisbon, Portugal,*, 2006.

[126] B W van Oudheusden, F Scarano, E W M Roosenboom, E W F Casimiri, and L J Souverein. Evaluation of integral forces and pressure fields from planar velocimetry data for incompressible and compressible flows. *Exp Fluids*, 43:153–162, 2007.

[127] B W van Oudheusden, F Scarano, N P van Hinsberg, and E W M Roosenboom. Quantitative visualization of the flow around a square-section cylinder at incidence. *J Wind Eng Ind Aerodyn*, 96:913–922, 2008.

[128] S Wang, D B Ingham, L Ma, M Pourkashanian, and Z Tao. Turbulence modeling of deep dynamic stall at relatively low Reynolds number. *J Fluids and Struct*, 33:191–209, 2012.

[129] S Wang, L Ma, D Ingham, M Pourkashanian, and Z Tao. Numerical investigations on dynamic stall of low Reynolds number flow around oscillating airfoils. *Comput Fluids*, 39:1529–1541, 2010.

[130] S Wang, Z Tao, L Ma, D Ingham, and M Pourkashanian. Numerical investigations on dynamic stall associated with low Reynolds number flows over airfoils. In *IEEE. 2nd Int Conf on Computer Eng and Tech*, 5:308-312, 2010.

[131] W Wenguo, F Weicheng, L Guangxuan, and Q Jun. An improved cross-correlation method for (digital) particle image velocimetry. *Acta Mechanica Sinica*, 17:332–339, 2001.

[132] P Wernert, W Geissler, J Kompenhans, and M Raffel. Experimental and numerical investigations of dynamic stall on a pitching airfoil. *AIAA J*, 34(5):982–989, 1996.

[133] J Westerweel. Fundamentals of digital particle image velocimetry. *Meas Sci Technol*, 8:1379–1397, 1997.

[134] J Westerweel, D Dabiri, and M Gharib. The effect of a discrete window offset on the accuracy of cross-correlation analysis of digital PIV recordings. *Exp Fluids*, 23:20–28, 1997.

[135] D C Wilcox. *Turbulence modeling for CFD*. DCW Industries, Inc., La Canada, California, 1998.

[136] J Wong, A Mohebbian, J Kriegseis, and D Rival. On the simulation of complex gusts at low Reynolds numbers. In *30th AIAA Applied Aerodynamics Conference, New Orleans, Louisiana*, 2012.

[137] J Wong, A Mohebbian, J Kriegseis, and D Rival. Rapid flow separation for transient inflow conditions versus accelerating bodies: an investigation into their equivalency, (in press). *J Fluids Struct*, 2013.

[138] A K Wright and D H Wood. Yaw rate, rotor speed and gyroscopic loads on a small horizontal axis wind turbine. *Wind Eng*, 31:197–209, 2007.

[139] S Yarusevych and S H Boutilier. Vortex shedding of an airfoil at low Reynolds numbers. *AIAA J*, 49(10):2221–2227, 2011.

[140] S P Yarusevych, P E Sullivan, and J G Kawall. On vortex shedding from an airfoil in low-Reynolds-number flows. *J Fluid Mech*, 632:245–271, 2009.

[141] S P Yarusevych, P E Sullivan, and J G Kawall. Smoke-wire flow visualization in seperated flows at relatively high velocities. *AIAA J*, 47:1592–1595, 2009.

[142] C N Young. *Algorithm enhancements for particle image velocimetry*. PhD thesis, University of Waterloo, Waterloo, Canada, 2004.

[143] G H Yu, X C Zhu, and Z H Du. Numerical simulation of a wind turbine airfoil: dynamic stall and comparison with experiments. *J Power Energy*, 224:657–677, 2010.

Appendix A

Experimental setup equipment

Ruland $CLX\_4\_4\_F$ rigid shaft coupling
CLX is for one piece clamp style; Its material is Black oxide steel, indicated as F in the model number. The size of the bores is .25", with a tolerance of $+0.002" / +0.0005"$.
http://www.ruland.com/ps_couplings_rigid_clx.asp.

T0603-A0-N-CG-N-F-A-A Cleveland Motion Controls MDM-5000
0603-A0: a 60mm frame, N: no thermal protection (standard), CG: 2000 incremental encoder(standard), N: no brake (standard), F: flying leads termination(standard), A:0.250" shaft w/flat, and last A: IP 65 w/o seal - standard ingress protection; The T0603 model provides a stall torque of 1.8 Nm and peak torque of 5.90 Nm.
http://www.torquesystems.com/mdm-5000-brushless-servo-motor.asp.
http://www.torquesystems.com/downloads/servo_motors/mdm-5000_ordering.pdf.

PSR-12-24 power supply
Its output is 12 Amps at 24 VDC while it needs 100-240 VAC, 50/60 Hz as its input.
http://www.galilmc.com/products/psr-power-supplies.php.

Galil Motion Controls CDS-3310
It features a unique programming language with built-in functions for various modes of motion, such as point-to-point positioning, contouring, and vector motion. There are 8 TTL uncommitted inputs and 10 TTL outputs, as well as 2 uncommitted analog inputs and 1 analog output for custom applications. Moreover, with optional DB-28040 more 8 analog inputs and 40 digital inputs and outputs can be added.
http://www.galilmc.com/products/cds-3310.php.

Edmund optics Laser Line Mirror
The 25mm Diameter mirror for 532nm laser beams. It is 0^o, but located in 45°.
http://www.edmundoptics.com.

Dantec dynamics FlowSense EO 4M camera
It can take pictures at 16.3/20.4 full resolution frames per second with an interframe time of 200 ns. It is capable of 2x, 3x, 4x, and 8x vertical and horizontal binning, allowing to take higher sensitivity photos at the cost of resolution. This makes it suitable for PIV applications when the light levels are low. A bandwidth of up to 160 MB/s is essential to sustain a secure image transfer for extended periods of time. For this purpose, a Camera Link Frame Grabber is connected to the system PC's PCIe bus. This makes on-camera memory unnecessary.

80N77 Timer Box
This timer Box comes with 8 independent output channels, and 2 input channels. This is enough to run a camera, which uses 1 output, and a dual-cavity laser, which uses 4 outputs.

Appendix B

Galil program

This program creates a sinusoidal oscillation for the airfoil and triggers the PIV system with a TTL output

```
'Tuning parameters
'Tuning parameters will be changed if the oscillating parameters, such as
'frequency and amplitude, the freestream velocity and the mass of the airfoil
'are changed.
#PARAM
STA     'stop motion
MOA     'motor off
TM250   'control loop update time 250 microsecs
(For high frequencies TM250 and for low frequencies TM1000 are recommended)
ILA=-.1 'integrator limit (< 0 makes tune independent of KI)
PLA=.4  'pole (adds low pass filter)
KDA=233 'derivative constant
KPA=27  'proportional constant
KIA=.1  'integration constant
FVA=1   'velocity feedforward
FAA=9   'acceleration feedforward
AG2     'amplifier gain (maximum)
SHA     'motor on
WT2000

'Main subroutine
```

```
#START
'Constants
per=70      'period in millisecs
amp=233     'amplitude in counts
init=-1     '+1=downstroke, -1=upstroke
VSS = (2*3.1416*amp)*(1000/per)/4 'vector speed (/1 if TM1000)
VA68431360  'vector acceleration (max)
VD68431360  'vector deceleration (max)
VM XN       'vector mode axes
'Linear motion
SP1250      'linear speed
AC12500     'linear acceleration
DC12500     'linear deceleration
PA amp*init 'move to initial position
BGA         'begin motion
AMA         'wait for finish
WT500       'wait for 500ms
'Sinusoidal motion
CR amp, (1-init)*90, 360 'draw circle
BGS         'begin motion
#LOOP
OCA=44,0    'trigger at absolute position
CR amp, (1-init)*90, 360 'draw circle
AV @INT[2*3.1416*amp]    'wait for finish
JP#LOOP     'repeat
EN

'Reset subroutine
#STOP
STA   'stop motion
AMA   'wait for finish
WT500 'wait for 500ms
PA0   'move to zero position
BGA   'begin motion
EN
```

Appendix C

Uncertainty analysis

The statistical uncertainty for the LDA and PIV methods are estimated according to Benedict and Gould [11] and shown in Table C.1. The RMS is used for calculating fluctuations (e.g. δ_u) around the phase-average (time-average) parameter while N is the number of uncorrelated observations.

If a parameter (B) is a function of uncorrelated variables (n), $B = f(y_1, y_2, ..., y_n)$, linear uncertainty propagation can be used to determine the uncertainty [11, 50],

$$\varepsilon_B = \sqrt{(\frac{\partial f}{\partial y_1}\varepsilon_{y_1})^2 + (\frac{\partial f}{\partial y_2}\varepsilon_{y_2})^2 + ... + (\frac{\partial f}{\partial y_n}\varepsilon_{y_n})^2}. \tag{C.1}$$

For example, the uncertainty of the vorticity can be determined according to Equation C.2. For the PIV vorticity field, considering the values of Table C.1, ε_{ω_z} has been determined 2.9% while it is dimensionless by U_∞/c.

$$\varepsilon_{\omega_z} = \frac{\sqrt{2}}{2}(\frac{\varepsilon_u}{\Delta y} - \frac{\varepsilon_v}{\Delta x}). \tag{C.2}$$

The same methodology has been adapted for aerodynamic loads, Equations 3.3 and 3.6 for the LDA and PIV techniques, respectively. The calculated uncertainties have been provided in Chapters 5 and 6.

Table C.1: Statistical uncertainty for LDA method, $Re = 10^5$ and PIV method, $Re = 4 \times 10^4$.

Uncertainty definition		LDA	PIV
$\varepsilon_u = \frac{\delta_u}{\sqrt{N}}$	$\frac{\varepsilon_u}{U_\infty} =$	0.26%	0.52%
$\varepsilon_v = \frac{\delta_v}{\sqrt{N}}$	$\frac{\varepsilon_v}{U_\infty} =$	0.30%	0.48%
$\varepsilon_{u'} = \frac{\delta_u}{\sqrt{2N}}$	$\frac{\varepsilon_{u'}}{U_\infty} =$	0.18%	0.37%
$\varepsilon_{v'} = \frac{\delta_v}{\sqrt{2N}}$	$\frac{\varepsilon_{v'}}{U_\infty} =$	0.21%	0.34%
$\varepsilon_{u'u'} = \frac{2\delta_u^2}{\sqrt{2N}}$	$\frac{\varepsilon_{u'u'}}{U_\infty^2} =$	0.03%	0.21%
$\varepsilon_{v'v'} = \frac{2\delta_v^2}{\sqrt{2N}}$	$\frac{\varepsilon_{v'v'}}{U_\infty^2} =$	0.03%	0.18%
$\varepsilon_{u'v'} = \frac{\sqrt{1+\frac{\frac{1}{N}\sum u'v'}{\delta_u \delta_v}}\delta_u \delta_v}{\sqrt{N}}$	$\frac{\varepsilon_{u'v'}}{U_\infty^2} =$	0.03%	0.12%